



**Max-Planck-Institut für Metallforschung**  
Stuttgart

---

**Fe-C and Fe-N compound layers:  
Growth kinetics and microstructure**

Thomas Greßmann

Dissertation  
an der  
**Universität Stuttgart**

---

Bericht Nr. 206  
September 2007



# **Fe-C and Fe-N compound layers: growth kinetics and microstructure**

Von der Fakultät Chemie der Universität Stuttgart zur  
Erlangung der Würde eines Doktors der Naturwissenschaften (Dr. rer. nat.)  
genehmigte Abhandlung

vorgelegt von

**Thomas Greßmann**

aus Bayreuth

Hauptberichter: Prof. Dr. Ir. E.J. Mittemeijer

Mitberichter: Prof. Dr. F. Aldinger

Mitprüfer: Prof. Dr. H. Bertagnolli

Tag der Einreichung: 05.07.2007

Tag der mündlichen Prüfung: 24.09.2007

**INSTITUT FÜR METALLKUNDE DER UNIVERSITÄT STUTTGART**  
MAX-PLANCK-INSTITUT FÜR METALLFORSCHUNG  
STUTTGART, 2007



# Table of contents

<b>1</b>	<b>Introduction.....</b>	<b>7</b>
1.1	Thermodynamics of gas nitriding and gas nitrocarburising .....	9
1.1.1	Nitriding in NH <sub>3</sub> /H <sub>2</sub> gas mixtures.....	10
1.1.2	Carburising in CO containing gas mixtures.....	12
1.1.3	Gas nitrocarburising.....	13
1.2	Crystal structure and homogeneity range of $\gamma'$ -Fe <sub>4</sub> N <sub>1-y</sub> , $\epsilon$ -Fe <sub>3</sub> (N,C) <sub>1+x</sub> and cementite.....	14
1.3	Growths kinetics of iron-(carbo-)nitride compound layers .....	16
1.4	Microstructure of Fe-N compound layers.....	17
	References.....	19
<b>2</b>	<b>Formation of massive cementite layers on iron by ferritic carburising in the additional presence of ammonia .....</b>	<b>21</b>
2.1	Introduction.....	22
2.2	Experimental procedure .....	23
2.2.1	Specimen preparation and thermochemical treatment.....	23
2.2.2	Analysis of the (nitro-)carburised specimens .....	24
2.3	Results and discussion .....	26
2.3.1	Influence of the ammonia content in the atmosphere on the layer constitution .....	26
2.3.2	Cementite layer-growths kinetics .....	31
2.4	Conclusions.....	33
	References.....	35
<b>3</b>	<b>X-ray diffraction line-profile analysis of hexagonal <math>\epsilon</math>-iron-nitride compound layers: composition- and stress-depth profiles .....</b>	<b>37</b>
3.1	Introduction.....	38
3.2	Experimental .....	41
3.2.1	Specimen preparation .....	41
3.2.2	Metallography .....	43
3.2.3	TEM and EBSD .....	43

3.2.4 X-ray diffractometry .....	43
3.3 Theoretical considerations .....	45
3.3.1 Model for the microstructure of $\varepsilon$ layers.....	45
3.3.1.1 Lattice-parameter-depth profile .....	45
3.3.1.2 Stress-depth profile .....	47
3.3.2 Diffraction effects of the microstructure model .....	48
3.3.3 Data-evaluation method.....	50
3.4 Results and discussion .....	54
3.4.1 Microstructure of the $\varepsilon$ layers, as determined by optical microscopy, TEM and EBSD .....	54
3.4.2 Qualitative description of the diffraction-line profile and preliminary analysis .....	55
3.4.3 Results of the fitting and discussion .....	59
3.4.3.1 Lattice-parameter-depth profiles.....	59
3.4.3.2 Residual stress-depth profiles .....	64
3.5 Conclusions.....	69
Appendix.....	71
Acknowledgement .....	71
References.....	72
<b>4 Elastic anisotropy of <math>\gamma'</math>-Fe<sub>4</sub>N and elastic grain interactions in <math>\gamma'</math>-Fe<sub>4</sub>N<sub>1-y</sub> layers on <math>\alpha</math>-Fe: first-principles calculations and diffraction stress measurements....</b>	<b>75</b>
4.1 Introduction.....	76
4.2 First-principles calculations of elastic constants .....	79
4.2.1 Theoretical background and method of calculation used .....	79
4.2.2 Results.....	83
4.3 Macrostrains and macrostresses in $\gamma'$ -Fe <sub>4</sub> N <sub>1-y</sub> layers.....	84
4.3.1 Determination of residual macrostresses by diffraction methods .....	84
4.3.2 Experimental.....	88
4.3.2.1 Specimen preparation and metallography .....	88
4.3.2.2 X-ray diffractometry .....	89
4.3.3 Results of X-ray stress analysis .....	90

---

4.4 Discussion.....	94
4.4.1 Interpretation of the calculated single-crystal elastic constants .....	94
4.4.2 The effective, experimentally determined type of grain interaction.....	98
4.5 Conclusions.....	99
Acknowledgement .....	100
References.....	100
<b>5 Zusammenfassung.....</b>	<b>105</b>
5.1 Einleitung.....	105
5.2 Experimentelles.....	107
5.3 Ergebnisse und Diskussion .....	108
5.3.1 Bildung und Wachstumskinetik von massiven Zementitschichten .....	108
5.3.2 Röntgenbeugungsanalyse von $\epsilon$ -Fe <sub>3</sub> N <sub>1+x</sub> Schichten: Linienprofilanalyse .	110
5.3.3 Elastische Anisotropie von $\gamma'$ -Eisennitrid .....	112
Literatur.....	114
<b>List of publications.....</b>	<b>115</b>
<b>Danksagung .....</b>	<b>117</b>
<b>Curriculum Vitae .....</b>	<b>119</b>





# *1*

## *Introduction*

Thermochemical surface treatments of iron and steel involving a reactive gas atmosphere, such as gas nitriding and gas nitrocarburising, are very important and versatile processes in the field of materials science in general and in surface engineering in particular [1, 2]. During these processes nitrogen or nitrogen and carbon are introduced into the surface region of iron-based work pieces at elevated temperature (typically below the eutectoid temperature, being 863 K for the binary Fe-N system [3]) in order to achieve microstructural features leading to various types of property improvements of the surface and near-surface region. These improvements are related to the formation of a hard, wear and corrosion resistant surface compound layer (thickness up to several 10  $\mu\text{m}$ ) consisting of different iron-nitride, iron-carbonitride and/or iron-carbide phases [4, 5] (Fig. 1.1). Moreover, the fatigue endurance is enhanced by the enrichment of the underlying bulk with nitrogen in the so-called diffusion zone (thickness of several 100  $\mu\text{m}$ ). Compared to many other thermochemical surface treatments, e.g. carburising, carbonitriding with process temperatures above 863 K, negligible changes of the dimensions of the workpieces occur upon nitriding and nitrocarburising, since the bulk remains ferritic during the treatment.

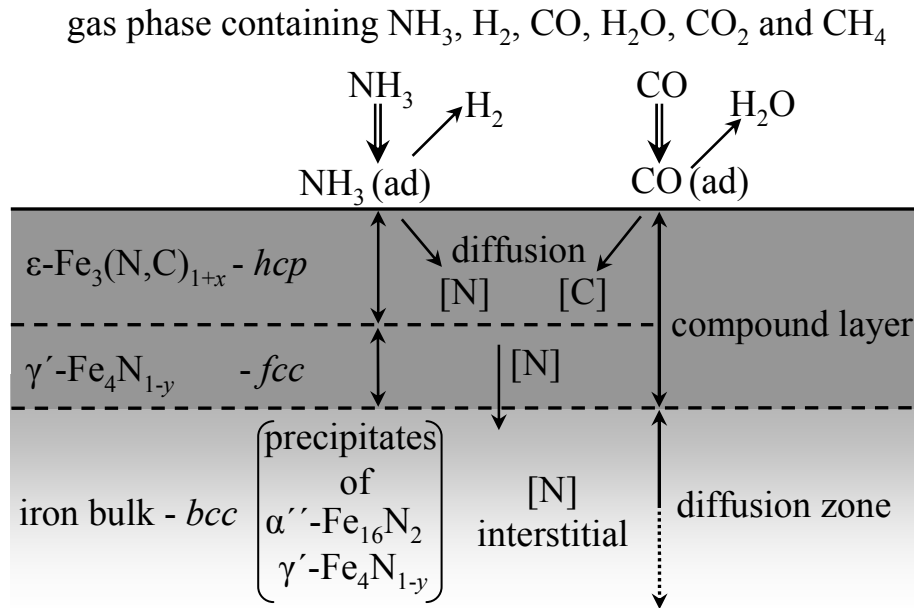


**Fig. 1.1:** Schematic presentation of the subdivision of the surface region into a compound layer and a diffusion zone of gas nitrocarburised, originally pure iron. The nitrogen transfer from the reactive gas atmosphere is realised by the dissociation of  $\text{NH}_3$  and the carbon transfer by the dissociation of  $\text{CO}$  at the iron surface. Diffusion occurs due to a gradient of the chemical potential of nitrogen and carbon from the surface to the substrate. After the nitriding nitrogen is in the iron bulk either interstitially dissolved or present as precipitates of  $\gamma'$  and/or  $\alpha''$ .

The controlled generation of specific compound-layer microstructures requires knowledge of the thermodynamics and kinetics and thus of the process parameters (e.g. atmospheric composition, temperature). Furthermore, the microstructures of the compound layers themselves are decisive for the latter's contribution to the improved surface properties of the work piece. However, many even very basic questions concerning the properties and characteristics of the compound-layer microstructure and of the different compound-layer phases are still unacknowledged. The present work addresses to solve some of these open questions, which are related to the *formation* of compound layers during nitrocarburising and to the *microstructure* of the iron-nitride phases and of the compound layer.

## 1.1 Thermodynamics of gas nitriding and gas nitrocarburising

During gas nitriding and gas nitrocarburising nitrogen and carbon are imposed by a gas mixture (main constituents  $\text{NH}_3/\text{H}_2$  or  $\text{NH}_3/\text{H}_2/\text{CO}$ , Fig. 1.1) on the surface of iron or of an iron-based material. The gas mixture provides certain chemical potentials of nitrogen and carbon. If local equilibrium between the gas phase and the surface of the metal prevails, the chemical potentials of nitrogen and carbon in the gas mixture and at the metal surface must be the same and, correspondingly, compositional changes and phase transformations may occur in the metal.

The chemical potential, which is the partial Gibbs energy  $\mu_{I,g}$  of a constituent  $I$  in the gas mixture, is defined as

$$\mu_{I,g} \equiv \mu_{I,g}^0 + RT \ln(f_I / f_I^0) = \mu_{I,g}^0 + RT \ln a_{I,g}, \quad (1.1)$$

where  $\mu_{I,g}^0$  is the chemical potential of  $I$  in the gaseous (g) reference state,  $f_I$  the fugacity of  $I$  in the gas mixture,  $f_I^0$  the fugacity of  $I$  in the reference state,  $R$  the gas constant and  $T$  the absolute temperature.  $a_I$  denotes the activity of  $I$  in the gas. If only ideal gases are assumed Eq. (1.1) becomes

$$\mu_{I,g} \equiv \mu_{I,g}^0 + RT \ln(p_I / p_I^0), \quad (1.2)$$

with  $p_I$  the partial pressure of  $I$  and  $p_I^0$  the pressure of  $I$  in the reference state.

In the solid the chemical potential of an element  $I$ , dissolved in the solid matrix is defined as

$$\mu_{I,s} \equiv \mu_{I,s}^0 + RT \ln a_{I,s}, \quad (1.3)$$

where  $\mu_{I,s}^0$  denotes the chemical potential of  $I$  in the solid (s) reference state and  $a_{I,s}$  is the activity of  $I$  in the dissolved state with respect to the reference state ( $a_I^0 = 1$ ). If the state of reference of  $I$  is the same for the gas and for the solid than it holds  $a_{I,s} = a_{I,g}$ .

### 1.1.1 Nitriding in NH<sub>3</sub>/H<sub>2</sub> gas mixtures

From solid iron and N<sub>2</sub> gas it is not possible at atmospheric pressure to form iron nitrides (cf. phase diagram [3], Fig. 1.2) or to dissolve considerable amounts of nitrogen in solid iron, because the chemical potential of nitrogen in N<sub>2</sub>, even at elevated temperatures, is too low. The necessary equilibrium pressure of N<sub>2</sub> for the formation of iron nitrides amounts up to several thousand atmospheres [6],



where [N] denotes nitrogen in solid solution or in the form of an iron nitride.

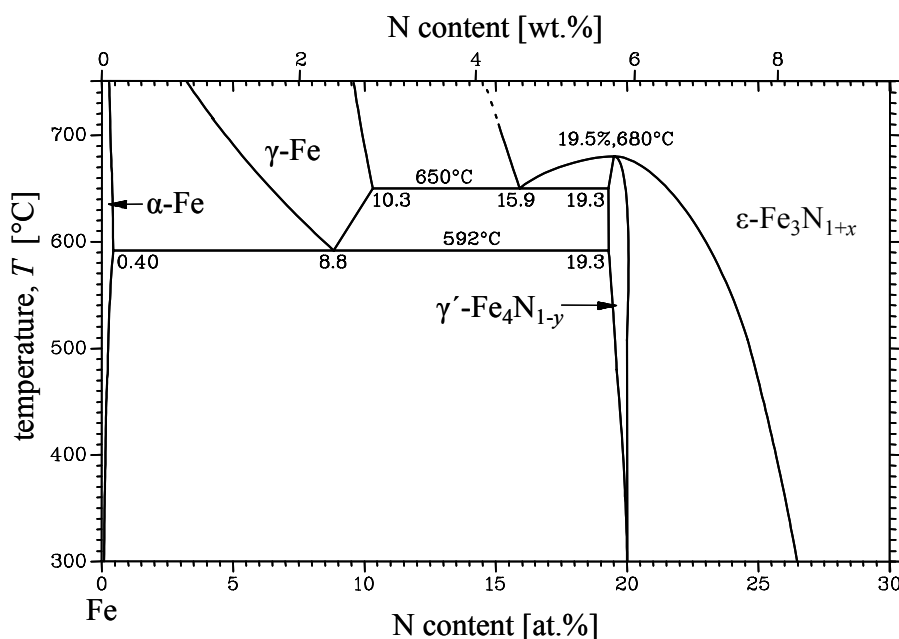


**Fig. 1.2:** Part of the metastable Fe-N phase diagram, redrawn according to Ref. [3].

One of the classical methods to achieve nitriding of solid iron is a treatment with NH<sub>3</sub>/H<sub>2</sub> gas mixtures at atmospheric pressure at about 700 – 860 K. By this method nitrogen can be introduced easily into the solid and allows formation of iron nitrides, since nitriding in NH<sub>3</sub>/H<sub>2</sub> gas mixtures can *formally* be conceived as the result of bringing iron into contact with N<sub>2</sub> gas at a certain, mostly extremely high partial pressure. This virtual N<sub>2</sub> partial pressure can be regarded as that one which would bring



into equilibrium at given NH<sub>3</sub> and H<sub>2</sub> partial pressures.

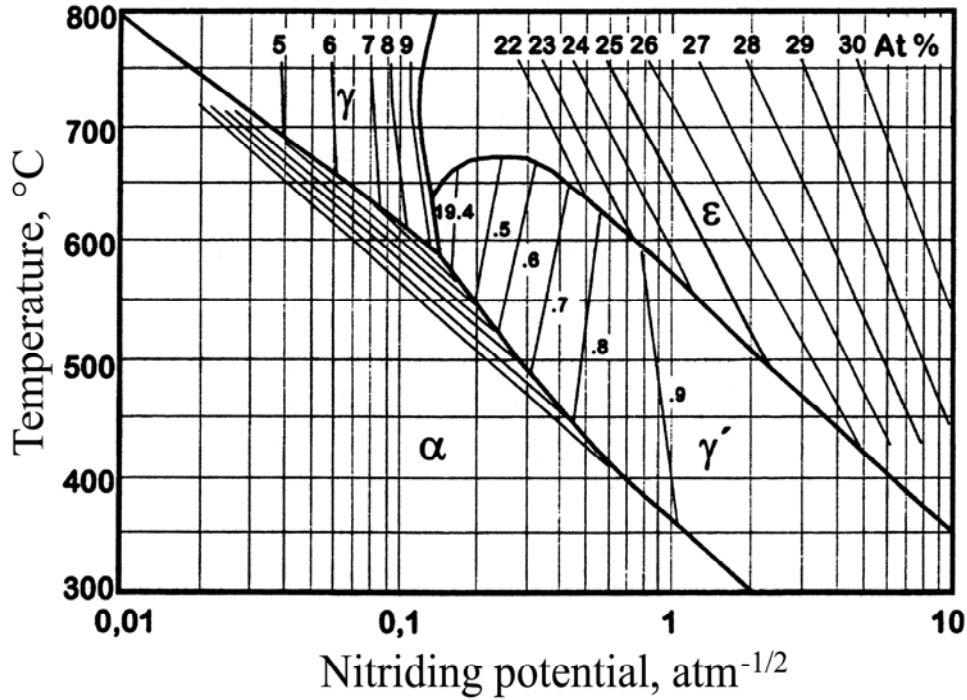


**Fig. 1.3:** Extended Lehrer diagram with additional isoconcentration lines [7], indicating which iron nitride or which solid solution is in equilibrium with a given nitriding atmosphere at a certain temperature. The atmosphere is characterised by the nitriding potential,  $r_N = p_{\text{NH}_3} / p_{\text{H}_2}^{3/2}$ .

Additionally, the thermal decomposition of  $\text{NH}_3$  according to Eq. (1.5) as well as the decomposition of the metastable nitrides (Eq. 1.4) is slow. Thus, it is possible to dissolve nitrogen into an iron surface according to Eq. (1.6), which is the hypothetical sum of Eq. (1.4) and Eq. (1.5):



According to Eqs. (1.1-1.3, 1.6) the chemical potential of nitrogen dissolved in the solid,  $\mu_{[\text{N}]}$ , obeys

$$\mu_{[\text{N}]} \equiv \frac{1}{2} \mu_{\text{N}_2}^0 + \frac{1}{2} RT \ln \left( \frac{p_{\text{N}_2}}{p^0} \right) = \mu_{\text{NH}_3}^0 - \frac{3}{2} \mu_{\text{H}_2}^0 + RT \ln \left( r_N \cdot (p^0)^{1/2} \right), \quad (1.7)$$

where  $p_{\text{N}_2}$  is the (virtual) pressure of  $\text{N}_2$  which would bring Eq. (1.5) into equilibrium (see above),  $p^0$  denotes the reference pressure for all gases (1 atm) and  $r_N$  denotes the so-called nitriding potential,

$$r_N = \frac{p_{\text{NH}_3}}{p_{\text{H}_2}^{3/2}}. \quad (1.8)$$

Thus, the activity of nitrogen provided by the  $\text{NH}_3/\text{H}_2$  gas atmosphere and under equilibrium conditions present at the surface of the solid can be calculated according to

$$a_N = K_1 \cdot r_N \cdot (p^0)^{-1/2}, \quad (1.9)$$

with  $K_1$  the equilibrium constant of Eq. (1.5).

By controlling the composition of the gas atmosphere in a furnace (e.g. by controlling the mass flow of  $\text{NH}_3$  and  $\text{H}_2$  through a tube furnace or by controlling the atmospheric composition in a chamber furnace) the nitriding potential  $r_N$  can be adjusted to a high degree of accuracy and thus, at a given temperature, also the chemical potential and the activity of nitrogen. The atmosphere is consequently in equilibrium with either a certain iron-nitride phase or a Fe-N solid solution [8-11]. In the so-called Lehrer diagram the information is compiled which iron nitride is formed in equilibrium as a function of the composition of the  $\text{NH}_3/\text{H}_2$  gas mixture (in agreement with Eq. (1.9) the decisive factor is the nitriding potential  $r_N$ ) and the treatment temperature [12]. In an extended version of the Lehrer diagram (Fig. 1.3) isoconcentration lines indicate the expected N content in the certain phase under particular nitriding conditions [7].

### 1.1.2 Carburising in CO containing gas mixtures

The transfer of carbon from the gas phase during a (nitro-)carburising treatment into the iron is usually associated with the presence of CO in the gas mixture. The carbon transfer from CO to the solid can occur in principle via the following reactions:



where  $[\text{C}]$  denotes carbon dissolved in the iron matrix or in a carbide or in a carbonitride. It has been shown experimentally that the heterogeneous water-gas

reaction (Eq. (1.11)) is considerably faster than the Boudouard reaction (Eq. (1.10)) [13]. For undergoing Eq. (1.11) the necessary  $H_2$  is either provided directly or as a result of the thermal dissociation of  $NH_3$  during nitrocarburising. In the following thermodynamic considerations only Eq. (1.11) will be discussed.

If local equilibrium between the gas phase and the solid exists, it follows that the carbon activity,  $a_C$ , obeys

$$a_C = K_2 \cdot r_C \cdot (p^0)^{-1}, \quad (1.12)$$

where  $K_2$  is the equilibrium constant of Eq. (1.11) and  $r_C$  is the corresponding carburising potential

$$r_C = \frac{p_{CO} \cdot p_{H_2}}{p_{H_2O}}. \quad (1.13)$$

As state of reference typically pure solid graphite at 1 atm is adopted for which  $a_C = 1$  holds. For certain atmospheric compositions  $a_C > 1$  is possible, by which carbides can be prepared. However, these carbides are metastable with respect to decomposition, leading to the formation of graphite.

### 1.1.3 Gas nitrocarburising

As mentioned above, nitrocarburising is typically performed in  $NH_3/H_2/CO$  gas mixtures. It must be mentioned that such gas mixtures are thermodynamically not in equilibrium at the nitrocarburising temperature: the carbon activity is hypothetically infinite with respect to both Eq. (1.10) and Eq. (1.11), because for the partial pressures of the reaction products it holds  $p_{H_2O} = p_{CO_2} = 0$ . Additionally to the above mentioned reactions (Eqs. (1.6, 1.10 and 1.11)) several homogeneous (Eqs. (1.14 – 1.16)) and heterogeneous (Eq. (1.17)) side reactions can occur, altering the composition of the gas mixture:





An unequivocal carbon activity of the gas phase can only be realised if the carbon activities associated with the different heterogeneous carbon-transfer reactions (Eqs. (1.10, 1.11 and 1.17)) are equal. It can be shown that in that situation also the homogeneous (*gas-phase shift*) reactions (Eqs. (1.14 – 1.16)) are in equilibrium. This, however, requires the simultaneous control of the partial pressures of  $\text{NH}_3$ ,  $\text{H}_2$ ,  $\text{CO}$ ,  $\text{CO}_2$ ,  $\text{CH}_4$  and  $\text{H}_2\text{O}$  vapour in the gas mixture, which is technologically not easily feasible.

In comparison to pure nitriding (section 1.1.1) the presence of a carbon delivering species in the gas mixture during nitrocarburising promotes the formation of the  $\epsilon$  phase, which can dissolve considerable amounts of carbon. This is not the case for the  $\gamma'$  phase (see also section 1.2). If the carbon activity provided by the gas phase is high enough also cementite  $\text{Fe}_3\text{C}$  can be formed in the compound layer [14].

## 1.2 Crystal structure and homogeneity range of $\gamma'$ - $\text{Fe}_4\text{N}_{1-y}$ , $\epsilon$ - $\text{Fe}_3(\text{N,C})_{1+x}$ and cementite

The most important phases occurring during nitriding/nitrocarburising in the compound layer are the  $\gamma'$ ,  $\epsilon$  and cementite phases. The first two phases,  $\gamma'$  and  $\epsilon$ , can be conceived as typical interstitial compounds with the iron atoms arranged in a cubic close-packed fashion in the  $\gamma'$  phase [15, 16] and in a hexagonal close-packed fashion in the  $\epsilon$  phase [17] (Fig. 1.4a and 1.4b). In both phases the octahedral interstitial sites are partially occupied by nitrogen (or in the  $\epsilon$  phase nitrogen can partially be substituted by carbon) with long-range order [16, 18-21], leading to space group  $Pm\bar{3}m$  for  $\gamma'$  and  $P6_322$  for  $\epsilon$ . Cementite (space group:  $Pnma$ ),  $\text{Fe}_3\text{C}$ , has an orthorhombic lattice, with twelve iron atoms and four carbon atoms per unit cell where each carbon atom is surrounded by eight iron atoms in a relatively irregular way (Fig. 1.4c) [22].



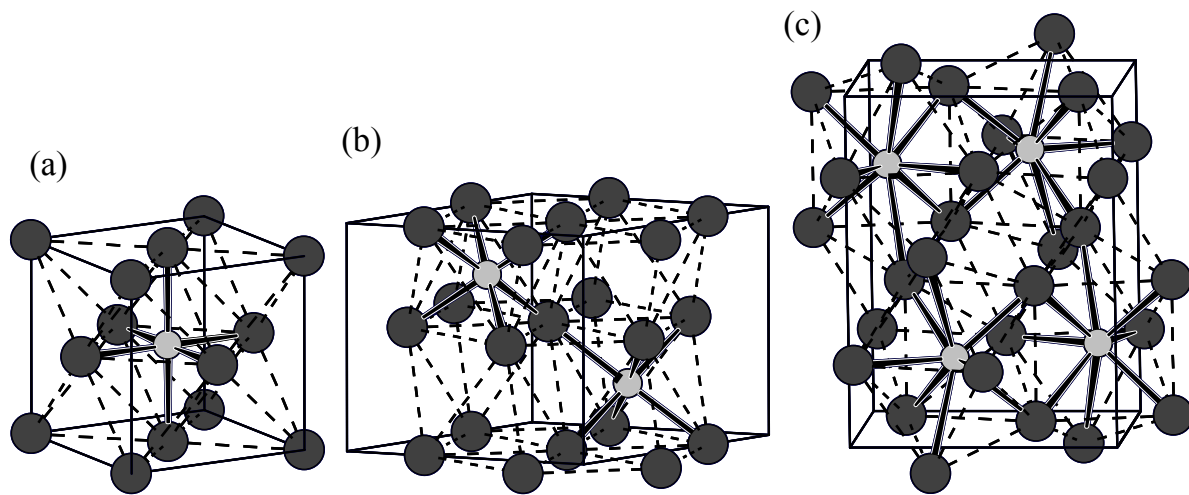


**Fig. 1.4:** Crystal structure of (a)  $\gamma'$ - $\text{Fe}_4\text{N}_{1-y}$ , (b)  $\epsilon$ - $\text{Fe}_3\text{N}_{1+x}$  and (c)  $\text{Fe}_3\text{C}$ . The darker spheres represent the iron atoms and the lighter spheres the nitrogen and carbon atoms. Fe-Fe ‘bonds’ are indicated by dashed lines and Fe-N and Fe-C ‘bonds’ are indicated by solid bold lines.

According to the Fe-N phase diagram (Fig. 1.2) the homogeneity range of the  $\gamma'$  phase is narrow and comprises nitrogen contents equal to and slightly lower than corresponding to  $\text{Fe}_4\text{N}$  [3]. The  $\epsilon$  iron-nitride phase has a wide, temperature-dependent homogeneity range, extending for example at 823 K from 24.05 at.% N up to almost 33 at.% N, often indicated by formulas like  $\epsilon$ - $\text{Fe}_3\text{N}_{1+x}$ ,  $\epsilon$ - $\text{Fe}_2\text{N}_{1-z}$  or  $\epsilon$ - $\text{FeN}_y$ . The wide homogeneity range of the  $\epsilon$  phase is associated with a considerable change of the lattice parameters with the nitrogen content [23, 24] (for the  $\gamma'$  phase also a relation between the lattice parameter and the composition has been reported [25]). In the  $\epsilon$  phase, considerable amounts of carbon (up to 8 at.% C) can be dissolved (e.g. denoted as  $\text{Fe}_3(\text{N,C})_{1+x}$ ) by partial substitution of nitrogen by carbon [26]. The total interstitial content N + C in the  $\epsilon$  phase can then at e.g. 823 K be even significantly lower than 24.05 at.% possible for pure nitride at that temperature [14]. Cementite ( $\text{Fe}_3\text{C}$ ) on the other hand is virtually stoichiometric [27]. The solubility of nitrogen in cementite is reported to be negligible [28].

### 1.3 Growths kinetics of iron-(carbo-)nitride compound layers

Many studies report on the largely parabolic layer-growth kinetics of iron-nitride surface compound layers produced by gas nitriding, e.g. Refs. [8, 10, 29], in order to obtain volume-diffusion coefficients of nitrogen within the compound-layer phases. In the field of nitrocarburising (using either gas or salt baths) much fewer details are known on the growth kinetics of the compound layer involving nitrogen *and* carbon diffusion into the iron substrate [14, 30-32]. Until now very little is known on the growth kinetics of cementite on  $\alpha$ -Fe substrates by ferritic (nitro-)carburising. This is to a considerable part caused by the fact that treatment of  $\alpha$ -Fe with strongly carburising atmospheres (viz. high carbon activities) leads besides the formation of cementite at the surface simultaneously to the deposition of graphite. Additionally, cementite is thermodynamically metastable with respect to the decomposition in Fe and graphite. Indeed, by carburising of  $\alpha$ -Fe in gas mixtures containing high contents of CO (besides  $H_2$ ,  $CO_2$ , hydrocarbons etc.) severe sooting of the surface with graphite and, if cementite forms, disintegration of the metal at the surface has been observed [33] (Fig. 1.5). This process is called ‘metal dusting’ and is highly undesired in practical applications.

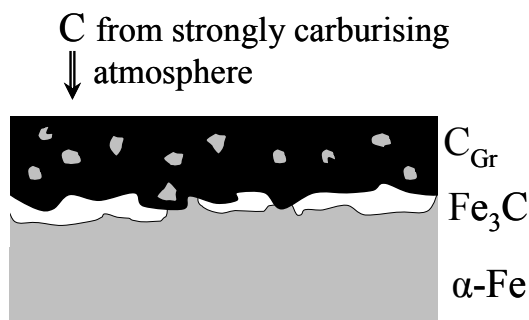


**Fig. 1.5:** Schematic representation of the process of ‘metal dusting’ of iron in strongly carburising environments. Graphite (black) forms at the surface the substrate which partially consists of  $Fe_3C$ . The metastable  $Fe_3C$  (white) decomposes in contact with graphite into graphite and iron particles (light particles within graphite) and thus disintegrates the metal, leading to a roughening of the initially flat iron surface.

In *chapter 2* of this work, it is shown for the first time that it is possible to grow massive  $Fe_3C$  layers using a certain composition of the gas mixture consisting of  $CO$ ,  $H_2$ ,  $NH_3$  and  $N_2$ . Applying this newly developed treatment sooting/graphite formation at the surface can be prevented and thus the disintegration of the metastable  $Fe_3C$  compound layer into  $\alpha$ -Fe and graphite can be suppressed. The growth kinetics of such

Fe<sub>3</sub>C surface compound layers as well as the effect of NH<sub>3</sub> on the carburising process will be evaluated and discussed.

## 1.4 Microstructure of Fe-N compound layers

In practical applications iron (based) massive workpieces are nitrided applying typically relatively high nitriding potentials which lead to the formation of  $\epsilon$ -Fe<sub>3</sub>N<sub>1+x</sub> at the surface. Due to the relatively low diffusion coefficient of nitrogen, in iron-nitride phases, a piece of bulk iron cannot be transformed into homogeneous iron nitride within feasible treatment times. Hence, only at the surface equilibrium with the gas phase can be achieved. Further away from the surface a continuous variation in the chemical potential of nitrogen is present, if local equilibrium holds everywhere in the solid. This change in the chemical potential leads to a certain nitrogen-concentration depth profile, which changes time dependently due to the inward diffusion of nitrogen. Since several phases with different nitrogen homogeneity ranges are involved the nitrogen concentration-depth profile is *not* continuous (Fig. 1.6). Due to the assumption of local equilibrium of the chemical potential of nitrogen at all phase interfaces the nitrogen-concentration values holding at the interfaces, i.e. at gas-solid interface and at the solid-solid interfaces, can be obtained from the Lehrer diagram (Fig. 1.3) and from the phase diagram (Fig. 1.2) [8]. Typical nitrided compound layers are thus composed of an outer surface-adjacent  $\epsilon$ -Fe<sub>3</sub>N<sub>1+x</sub> sublayer and an inner, substrate-adjacent  $\gamma'$ -Fe<sub>4</sub>N<sub>1-y</sub> sublayer (Fig. 1.1). The nitrogen concentration-depth profile present at the nitriding temperature can be retained at room temperature by quenching.

Since, especially, the  $\epsilon$  phase has a wide homogeneity range for nitrogen, the ‘quenched-in’ concentration gradient within the  $\epsilon$  layer after nitriding leads to a considerable variation of the lattice parameters with depth. Furthermore, macrostresses may build up within the compound layer during growth due to a compositional misfit within the layers caused by the concentration gradient and, after growth, due to a thermal misfit between the layer phases and the substrate, viz. different coefficients of thermal expansion of the different phases [34]. In *chapter 3* high-resolution X-ray

diffraction measurements at different specimen tilt angles  $\psi$  using synchrotron radiation revealed a pronounced anisotropic diffraction-line broadening of the  $\epsilon$  reflections. The obtained diffraction patterns are successfully described by a newly developed microstructure model with which it is possible to determine simultaneously the evolution of the (strain-free) lattice parameters with depth as well as a stress-depth profile.

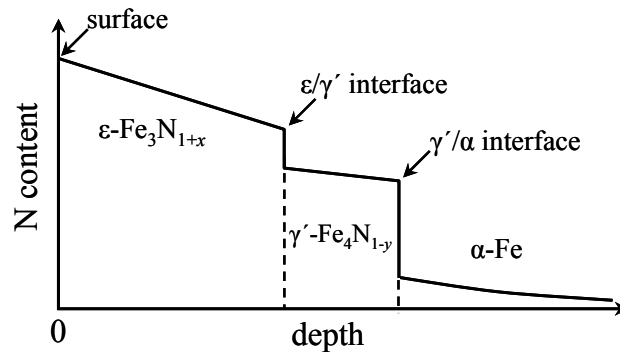


**Fig. 1.6:** Schematic illustration of a typical nitrogen concentration-depth profile of an iron-nitride compound layer. At the interfaces between different phases (indicated by arrows) local equilibrium is assumed to prevail at the nitriding temperature. This profile can be retained at room temperature by quenching. Nitrogen contents at the solid-phase interfaces can be obtained from the phase diagram.

Analysis of  $\gamma'$  layers (*chapter 4*) by X-ray stress measurements using several reflections  $hkl$  simultaneously revealed a for *fcc*-type metals unusual elastic anisotropy of  $\gamma'$  with  $\langle 100 \rangle$  as stiffest and  $\langle 111 \rangle$  as most compliant direction. These results are compared with single-crystal elastic constants obtained by first-principles calculations and are related to the crystal structure of  $\gamma'$ -Fe<sub>4</sub>N in order to get a better understanding of the elastic properties of  $\gamma'$ .

## References

- [1] Knerr CH, Rose TC, Filkowski JH. In: ASM Handbook Heat Treating Vol 4, Eds.: Davis, JR, Davidson, GM, Lampman, SR, Zorc, TB, Daquila, JL, Ronke, AW, Henniger, KL, Uhl, RC, ASM International, 1991, p. 387.
- [2] Liedtke D, Baudis U, Boßlet J, Huchel U, Klümper-Westkamp H, Lerche W, Spies H-J. Wärmebehandlung von Eisenwerkstoffen. Renningen: Expert Verlag, 2006.
- [3] Wriedt HA, Gokcen NA, Nafziger RH. Bull Alloy Phase Diagr 1987;8:355.
- [4] Bell T. Heat Treat Met 1975;2:39.
- [5] Dawes C, Tranter DF. Heat Treat Met 1985;3:70.
- [6] Mittemeijer EJ, Slycke JT. Surf Eng 1996;12:152.
- [7] Hoffmann R. Härtereit-Tech Mitt 1996;51:5.
- [8] Mittemeijer EJ, Somers MAJ. Surf Eng 1997;13:483.
- [9] Maldzinski L, Przylecki Z, Kunze J. Steel Res 1986;57:645.
- [10] Somers MAJ, Mittemeijer EJ. Metall Mater Trans A 1995;26A:57.
- [11] Kooi BJ, Somers MAJ, Mittemeijer EJ. Metall Mater Trans A 1996;27A:1063.
- [12] Lehrer E. Z Elektrochem 1930;36:383.
- [13] Grabke HJ. Arch Eisenhüttenw 1975;46:75.
- [14] Du H, Somers MAJ, Ågren J. Metall Mater Trans A 2000;31A:195.
- [15] Jack KH. Proc Roy Soc, A 1948;195:34.
- [16] Jacobs H, Rechenbach D, Zachwieja U. J Alloys Compd 1995;227:10.
- [17] Hägg G. Nature 1928;121:826.
- [18] Jack KH. Proc Roy Soc, A 1948;195:56.
- [19] Jack KH. Acta Crystallogr 1952;5:404.
- [20] Leineweber A, Jacobs H. J Alloys Compd 2000;308:178.
- [21] Leineweber A, Jacobs H, Hüning F, Lueken H, Kockelmann W. J Alloys Compd 2001;316:21.
- [22] Wood IG, Vocadlo L, Knight KS, Dobson DP, Marshall WG, Price GD, Brodholt J. J Appl Crystallogr 2004;37:82.

- 
- [23] Somers MAJ, Kooi BJ, Maldzinski L, Mittemeijer EJ, van der Horst AA, van der Kraan AM, van der Pers NM. *Acta Mater* 1997;45:2013.
- [24] Liapina T, Leineweber A, Mittemeijer EJ, Kockelmann W. *Acta Mater* 2004;52:173.
- [25] Somers MAJ, van der Pers NM, Schalkoord D, Mittemeijer EJ. *Metall Trans A* 1989;20A:1533.
- [26] Naumann FK, Langenscheid, G. *Arch Eisenhüttenw* 1965;36:677.
- [27] Massalski TB, Okamoto H. *Binary Alloy Phase Diagrams*: ASM International, USA, 1990.
- [28] Kagawa A, Okamoto T. *Trans Jap Inst Met* 1981;22:137.
- [29] Torchane L, Bilger P, Dulcy J, Gantios M. *Metall Mater Trans A* 1996;27A:1823.
- [30] Somers MAJ, Mittemeijer EJ. *Surf Eng* 1987;3:123.
- [31] Somers MAJ, Colijn PF, Sloof WG, Mittemeijer EJ. *Z Metallkunde* 1990;81:33.
- [32] Slycke J, Sproge L, Ågren J. *Scand J Met* 1988;17:122.
- [33] Grabke HJ. *Mater Corr* 2003;54:736.
- [34] Somers MAJ, Mittemeijer EJ. *Metall Trans A* 1990;21A:189.

***Formation of massive cementite layers on iron by ferritic carburising in the additional presence of ammonia***

*T. Greßmann, M. Nikolussi, A. Leineweber, E. J. Mittemeijer*

**Abstract**

Massive Fe<sub>3</sub>C compound layers were grown on  $\alpha$ -Fe substrates at 823 K by a gas carburising process in the additional presence of NH<sub>3</sub>. Whereas pure carburising employing a CO/H<sub>2</sub>/N<sub>2</sub> gas mixture leads, besides Fe<sub>3</sub>C formation, to severe graphite formation, the latter can be suppressed by a partial substitution of N<sub>2</sub> in the gas mixture by NH<sub>3</sub>. The growth kinetics of the obtained massive Fe<sub>3</sub>C layers can be described by a two-stage process.

## 2.1 Introduction

Improvement of the mechanical and chemical properties of iron and iron-based workpieces is often realised by the application of surface layers. Such layers can for example be produced by gaseous nitriding/nitrocarburising [1]. These thermochemical surface treatments are widely applied in order to improve the corrosion and wear resistance as well as the fatigue endurance [2]. Thereby, nitrocarburising is the most versatile surface treatment for ferritic steels.

Upon conventional gaseous nitrocarburising (e.g. by annealing in ammonia and carbonmonoxide containing gas mixtures at temperatures below 853 K) nitrogen and carbon are provided simultaneously to an iron-based surface by atmospheres possessing nitrogen and carbon chemical potentials sufficiently high to form compound layers composed of iron-(carbo-)nitrides. These compound layers are usually composed of an outer  $\epsilon$ -Fe<sub>3</sub>(N,C)<sub>1+x</sub> sublayer adjacent to the surface and an inner  $\gamma'$ -Fe<sub>4</sub>N sublayer adjacent to the layer/substrate interface. The presence of a carbon delivering species in the gas mixture promotes the formation of the  $\epsilon$  phase which can dissolve considerable amounts of carbon [3, 4], which is not the case for the  $\gamma'$  phase.

Until now, only a few systematic investigations on the dependence of the constitution of the compound layer on the gas composition have been performed for high chemical potentials of carbon (as provided by e.g. relatively high CO contents in the gas atmosphere) and for the concurrent presence of ammonia [1, 4-6]. It has been reported that in nitrocarburising atmospheres, with high chemical potentials of carbon, besides (carbo-)nitrides also cementite can form, leading to complex compound-layer microstructures [1, 6]. The nitrocarburising process can even be accompanied by sooting of the surface, if very high CO contents in the gas mixture are applied [4, 5]. Graphite formation is also associated with 'metal dusting', i.e. disintegration of the surface of iron-based work pieces in carburising atmospheres due to the decomposition of cementite into iron and graphite [7].



The present work demonstrates for the first time that it is possible to grow massive cementite surface layers on  $\alpha$ -Fe by carburising (with CO) in the *presence* of ammonia in the gas atmosphere. Ammonia has been found to be decisive for the suppression of sooting and metal dusting which occur in the *absence* of ammonia. The influence of the ammonia content in the atmosphere has been systematically examined. For a selected atmospheric composition the growth kinetics of the cementite surface layer has been evaluated. Such massive cementite layers may be used for applications where corrosion resistant and very hard ( $\text{Fe}_3\text{C} \sim 1000 \text{ HV}$  [8]) surface layers are needed and the properties of the bulk have to be retained.

## 2.2 Experimental procedure

### 2.2.1 Specimen preparation and thermochemical treatment

An iron (Alfa Aesar, 99.98 wt.%) cast rod was cold rolled to a plate of about 1 mm thickness and cut into rectangular pieces (20 mm  $\times$  25 mm). Before (nitro-)carburising these specimens were recrystallised for 2 h at 973 K under hydrogen, mechanically polished (final stage 1  $\mu\text{m}$  diamond) and cleaned ultrasonically in ethanol.

The (nitro-)carburising treatment was performed in a vertical quartz tube furnace equipped with a water container for quenching. The process temperature of 823 K was controlled within  $\pm 1 \text{ K}$  at the position of the sample. The (nitro-)carburising atmosphere was composed of carbon monoxide (99.97 vol.%) as carbon supply, hydrogen (99.999 vol.%), ammonia (99.999 vol.%) as nitrogen supply and nitrogen (99.999 vol.%) as inert gas<sup>2.1</sup>. The flow rate of each gas was controlled with mass flow controllers. The overall flow rate of the gas mixture through the quartz retort (diameter 28 mm) was with 13.5 mm/s (for the gas volume at room temperature) sufficiently high to minimise the effect of reactions changing the composition of the gas phase, e.g. ammonia decomposition. For all experiments, the CO and H<sub>2</sub> contents in the gas mixture were kept constant at 20.0 vol.% and 58.0 vol.%, respectively, whereas the content of ammonia and inert nitrogen gas as well as the process time were variable.

---

<sup>2.1</sup> At atmospheric pressure and at the process temperature N<sub>2</sub> does not dissociate and hence does not react with solid iron.

After the thermochemical heat treatment the specimens were quenched in water at room temperature flushed with N<sub>2</sub>.

**Table 2.1:** Composition of the gas mixtures applied for experiment series *A*, with constant volume fractions of 20.0 vol.% CO and 58.0 vol.% H<sub>2</sub>; the nitriding potential  $r_N = p_{\text{NH}_3} / p_{\text{H}_2}^{3/2}$ ; the phases observed and the optical appearance of the surface after the treatments at 823 K for 4 h and 24 h, see also Fig. 2.3.

NH <sub>3</sub> [vol.%]	N <sub>2</sub> [vol.%]	$r_N$ [atm <sup>-1/2</sup> ]	Phases observed by XRD	Appearance of the surface
22.0 <sup>a</sup>	0	0.5	ε, γ', Fe <sub>3</sub> C	matt grey
17.6	4.4	0.4	Fe <sub>3</sub> C	shiny
13.2	8.8	0.3	Fe <sub>3</sub> C	shiny
6.6	15.4	0.15	Fe <sub>3</sub> C, graphite	partially sooted
3.3 <sup>a</sup>	18.7	0.075	Fe <sub>3</sub> C, graphite	partially sooted
1.7 <sup>a</sup>	20.3	0.0375	Fe <sub>3</sub> C, graphite	black
0	22.0	0	Fe <sub>3</sub> C, graphite	black

<sup>a</sup> treatment only for 4 h

Two series of experiments were performed: for series *A* treatment times of 4 h and 24 h and variable ammonia and nitrogen gas contents (22.0–*n* vol.% NH<sub>3</sub>; *n* vol.% N<sub>2</sub>) were applied (Table 2.1, where also corresponding values of the nitriding potential<sup>2.2</sup>,  $r_N = p_{\text{NH}_3} / p_{\text{H}_2}^{3/2}$  [9], have been gathered), whereas for series *B* constant volume fractions for NH<sub>3</sub> and N<sub>2</sub> were applied (13.2 vol.% and 8.8 vol.%, respectively) with treatment times varying from 5 min to 48 h.

### 2.2.2 Analysis of the (nitro-)carburised specimens

The thermochemically treated specimens were cut into two pieces, which were used for optical microscopy and X-ray diffraction (XRD), respectively. The piece used for light microscopical investigation was covered with an electrodeposited protective

<sup>2.2</sup> The nitriding potential  $r_N$  is commonly used to quantify the chemical potential of nitrogen in NH<sub>3</sub>/H<sub>2</sub> gas mixtures, which is considerable higher than that of molecular N<sub>2</sub> [9].

nickel layer by using a Watts bath [10] (at 333 K) in order to avoid curvature and damaging close to the surface of the specimen during subsequent metallographic handling. Next, the piece was embedded (Polyfast, Buehler GmbH) and ground and polished (final step: 1  $\mu\text{m}$  diamond paste). After etching in 1 vol.% Nital containing 0.1 vol.% HCl [1, 6, 11] some cross sections were stained either with a Murakami solution (1 g NaOH, 1 g KOH and 4 g  $\text{KMnO}_4$  per 100 ml distilled water) at 333 K or with an alkaline sodium picrate solution (25 g NaOH and 2 g picric acid per 75 ml distilled water) at room temperature. The staining occurred selectively on the carbon containing phases, i.e. here  $\epsilon\text{-Fe}_3(\text{N,C})_{1+x}$  and  $\text{Fe}_3\text{C}$  [12, 13]. Light optical microscopy was performed with a Leica DMRM microscope. For each specimen several cross-sectional micrographs were taken close to both faces of the specimen. The cementite surface-layer thickness was determined from these micrographs: the measured area of the layer was divided by the measured lateral length of the layer, yielding the layer thickness. The values of several micrographs were arithmetically averaged.

For phase identification X-ray diffraction analysis was applied by recording diffractograms from the surface of the second piece of the original specimen, using a PANalytical X'Pert MP diffractometer ( $\text{CoK}\alpha$  radiation), equipped with a graphite monochromator in the diffracted beam and employing Bragg-Brentano geometry. During the measurements the specimen pieces were rotated around the surface normal to achieve better crystallite statistics. For lattice-parameter determination Si standard powder suspended in isopropanol was deposited as a thin layer on the surface of the specimen in order to calibrate the diffraction angle.

Quantitative Electron Probe Micro Analysis (EPMA) was performed employing a Cameca SX100 instrument to determine the carbon and nitrogen contents in the compound layer. To this end the intensities of the  $\text{N-K}\alpha$ ,  $\text{C-K}\alpha$  and  $\text{Fe-K}\alpha$  radiations, excited by an incident 10 keV electron beam, were measured simultaneously. Before the measurement started, oxygen was blown at each location onto the cross section for 40 s while the electron beam was switched on in order to remove carbon contamination, which would otherwise obscure the  $\text{C-K}\alpha$  intensity stemming from the carbon present in the material probed [14]. The  $\text{K}\alpha$  intensities of nitrogen, carbon and iron were compared with the corresponding intensities of  $\gamma\text{'-Fe}_4\text{N}$ ,  $\text{Fe}_3\text{C}$  and pure iron

standards. Concentration values were calculated from the intensity ratios applying the  $\Phi(\rho z)$  approach [15].

## 2.3 Results and discussion

### 2.3.1 Influence of the ammonia content in the atmosphere on the layer constitution

At the highest  $\text{NH}_3$  content in the gas atmosphere (22.0 vol.%), the outer, visual appearance of the specimen of experiment series *A* (Table 2.1) is similar to that of conventionally nitrided surfaces: matt grey. The microstructure of the developed compound layer is rather complex (Fig. 2.1a) as compared to the microstructure of the compound layer developed by pure nitriding of iron [16]. Comparing the results of XRD and light microscopical investigation after Murakami staining, it appears that the outer part of the layer consists predominantly of  $\epsilon\text{-Fe}_3(\text{N,C})_{1+x}$  and cementite (both stained), the latter phase exhibiting sometimes a needle-like morphology. The unstained part of the compound layers - adjacent to the substrate - is identified as  $\gamma'\text{-Fe}_4\text{N}$ . The thickness of the overall compound layer is quite irregular. At regions where more cementite is present the total compound-layer thickness is smaller than at regions consisting predominantly of  $\gamma'\text{-Fe}_4\text{N}$  (Fig. 2.1a). This suggests that cementite hinders the diffusion of nitrogen and carbon as compared to  $\epsilon\text{-Fe}_3(\text{N,C})_{1+x}/\gamma'\text{-Fe}_4\text{N}$  layers.

For lower ammonia contents in the gas atmosphere (17.6 and 13.2 vol.%  $\text{NH}_3$ ) the sample surface remains metallicly shiny (Fig. 2.2b) as prior to nitrocarburising (Fig. 2.2a). Optical microscopy on the cross sections and XRD analysis revealed that the microstructure of the compound layers changes upon decreasing the ammonia content in the gas mixture from multiphase to monophase layers consisting only of cementite (Fig. 2.1b). These compound layers are of much more homogeneous thickness and are also thinner than in the above discussed case where iron (carbo-) nitrides are also present. EPMA demonstrated that the carbon content in these layers is 25 at.%, corresponding to the formula  $\text{Fe}_3\text{C}$ . Nitrogen could not be detected, which is in agreement with previously reported values for the maximum, marginal solubility of

nitrogen in  $\text{Fe}_3\text{C}$  [17]. This is, in any case, much lower than the nitrogen detection limit of the EPMA technique. X-ray diffraction analysis was used to determine the lattice parameters of the cementite phase in these layers. The observed lattice parameters of orthorhombic cementite,  $a = 5.0936 \pm 0.0006 \text{ \AA}$ ,  $b = 6.7685 \pm 0.0008 \text{ \AA}$ ,  $c = 4.5310 \pm 0.0008 \text{ \AA}$  ( $Pnma$  setting), are larger than those reported in literature [18]. One has to recognise that these values were determined with the diffraction vector perpendicular to the surface. Therefore, the too large values for the lattice parameters can be explained as the consequence of the presence of compressive stresses parallel to the surface within the compound layers, as confirmed by additional X-ray stress measurements.

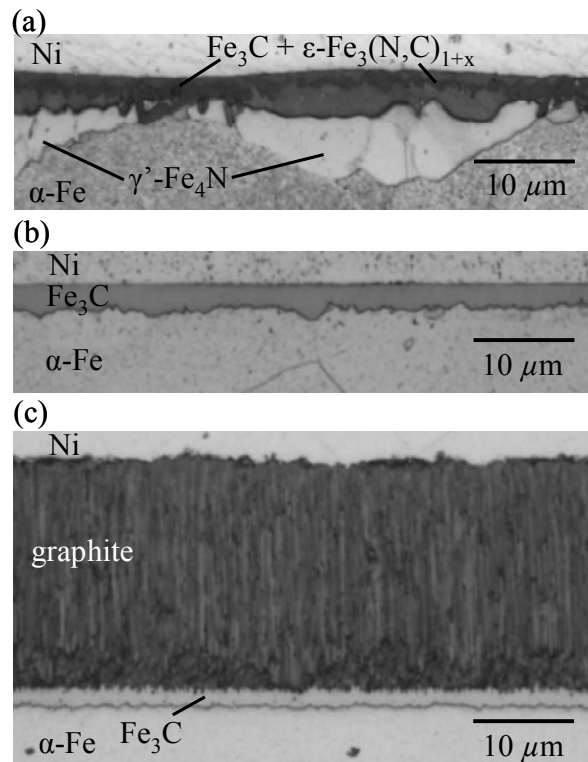


**Fig. 2.1:** Optical micrographs (bright field) showing cross sections of compound layers obtained on  $\alpha$ -Fe specimens by (nitro-)carburising at 823 K for 4 h after Nital etching; Applied gas mixture consisting of 20.0 vol.%  $\text{CO}$ , 58.0 vol.%  $\text{H}_2$  and (a) 22.0 vol.%  $\text{NH}_3$  (after additional Murakami staining; showing a complex microstructure, consisting of  $\epsilon\text{-Fe}_3(\text{N,C})_{1+x}$  and cementite (both stained) near the surface and  $\gamma'\text{-Fe}_4\text{N}$  adjacent to the substrate), (b) 13.2 vol.%  $\text{NH}_3$ , 8.8 vol.%  $\text{N}_2$  (after additional staining with picrate; showing a single  $\text{Fe}_3\text{C}$  layer) and (c) 22.0 vol.%  $\text{N}_2$  ( $\text{Fe}_3\text{C}$  layer slightly stained with picrate; the  $\text{Fe}_3\text{C}$ /graphite interface is roughened due to metal dusting).

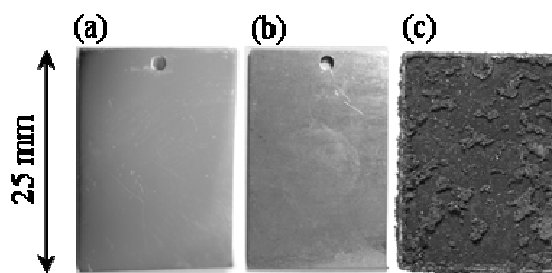


**Fig. 2.2:** Photographs of the  $\alpha$ -Fe samples (a) before (nitro-)carburising, (b) after (nitro-)carburising in a 13.2 vol.%  $\text{NH}_3$ , 58.0 vol.%  $\text{H}_2$ , 20.0 vol.%  $\text{CO}$ , 8.8 vol.%  $\text{N}_2$  gas mixture exhibiting a cementite layer and (c) after carburising in a 58.0 vol.%  $\text{H}_2$ , 20 vol.%  $\text{CO}$ , 22.0 vol.%  $\text{N}_2$  gas mixture (severely sooted).

Further reduction of the ammonia content in the gas atmosphere (down to values  $\leq 6.6$  vol.%  $\text{NH}_3$ ) leads to the formation of soot (graphite) on the surface of the samples, which is easily recognised visually since the surface becomes black (Fig. 2.2c). The degree of sooting *increases* with *decreasing*  $\text{NH}_3$  content in the gas atmosphere. In the extreme case of no ammonia in the atmosphere, the surface is severely sooted. The cross-sectional micrograph (Fig. 2.1c) reveals that the outer surface adjacent part of the specimen is composed of graphite. A relatively thin cementite layer remains adjacent to the substrate. The presence of both cementite and graphite is confirmed by XRD. During the (nitro-)carburising process the former surface of the sample, which is now the interface between  $\text{Fe}_3\text{C}$  and graphite, has become quite rough as a result of disintegration of  $\text{Fe}_3\text{C}$  on the iron surface caused by metal dusting (Fig. 2.1c).

The addition of different amounts of ammonia to the carburising gas atmosphere does not only affect the microstructure/constitution of the compound layer, but also the cementite-layer thickness. The higher the ammonia content, the thicker the cementite layer becomes. The relation between the ammonia content in the gas mixture and the corresponding cementite-layer thickness for treatment times of 4 h and 24 h as well as the approximate ammonia-content range where pure, massive cementite layers can be generated are shown in Fig. 2.3.

Indications that nitrogen delivering species in the gas atmosphere can suppress carbon deposition on an iron-based surface have also been made in the case of an

'ion-softnitriding' study on steels in CH<sub>4</sub>/H<sub>2</sub>/N<sub>2</sub> gas mixtures<sup>2.3</sup> [19], however, without giving details. Furthermore, some observations in Ref. [20], where deformed Fe-Cr-Ti alloys were exposed to strongly carburising gas mixtures composed of C<sub>3</sub>H<sub>8</sub>, C<sub>4</sub>H<sub>10</sub> and NH<sub>3</sub> at 853 K, can also be interpreted such that ammonia suppresses the formation of graphite on the surface of the specimen.

In order to explain the possible role of ammonia in preventing sooting, one could think of substitution of some carbon in the cementite by nitrogen, which might reduce the chemical potential of carbon in Fe<sub>3</sub>C so that it may become less unstable with respect to decomposition in Fe and graphite. However, the solubility of nitrogen in cementite is extremely low (EPMA results reported above and see Ref. [17]). A possible, more likely explanation could be that nitrogen at the gas/solid interface kinetically suppresses the formation of graphite there. Here it should be mentioned that the presence of gaseous H<sub>2</sub>S in strongly carburising gas mixtures also suppresses metal dusting: H<sub>2</sub>S is adsorbed at the surface and hence reduces the number of adsorption sites for CO at the iron surface [21]. However, H<sub>2</sub>S in particular hinders carbon to enter the solid and to form cementite, whereas ammonia only prevents sooting, but still allows carbon to enter the substrate, according to the results of the present study.

The presence of ammonia even appears to accelerate the carbon absorption, as evidenced by the observed layer-growth rate (increasing layer-growth rate with increasing ammonia content in the atmosphere; see Fig. 2.3). A faster absorption of carbon in the presence of a nitrogen providing media has been observed also in the case of the austenitic carbonitriding processes [22].

---

<sup>2.3</sup> In the ion-nitriding process N<sub>2</sub> is activated and thus can be used for nitriding reactions, whereas this is not possible in the conventional gaseous nitriding/nitrocarburising process (see footnote 2.1).

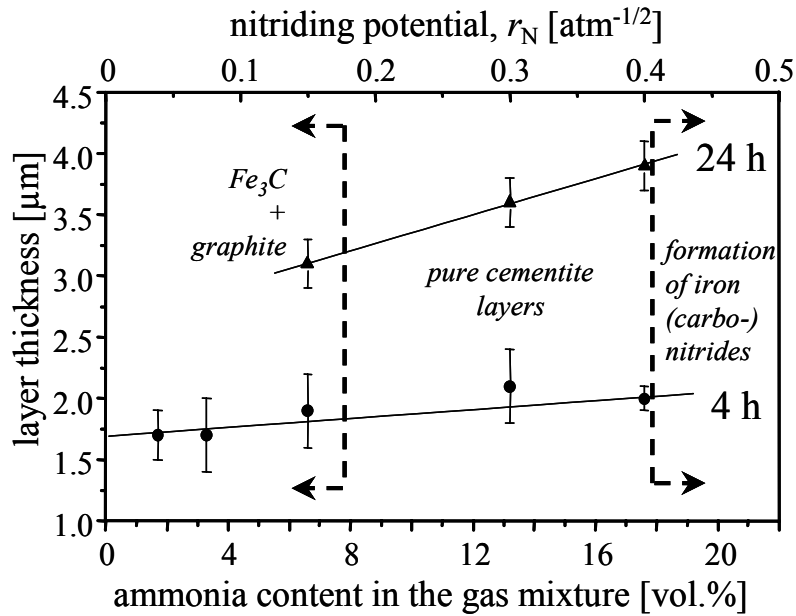


**Fig. 2.3:** Dependence of the cementite layer-thickness on the ammonia content for 4 h and 24 h treatments at 823 K in gas mixtures consisting of 20.0 vol.% CO, 58.0 vol.% H<sub>2</sub>, 22.0 –  $n$  vol.% NH<sub>3</sub> and  $n$  vol.% N<sub>2</sub>. The approximate ranges for the formation of pure cementite layers, cementite layers accompanied by sooting and the region where layers consisting of cementite and iron (carbo-) nitrides are formed have been indicated.

The following consideration may explain how ammonia enhances the cementite layer-growth rate by an accelerated carbon uptake. The heterogeneous carbon uptake reactions are [7]<sup>2.4</sup>:



These are total reactions, which can be subdivided in steps. The CO dissociation can be written as



<sup>2.4</sup> The initial gas mixtures composed of CO/H<sub>2</sub>/NH<sub>3</sub>/N<sub>2</sub>, as applied in this work, are not in equilibrium at the nitrocarburising temperature, since several homogeneous and heterogeneous reactions involving e.g. CO<sub>2</sub>, H<sub>2</sub>O, CH<sub>4</sub> can occur. The chemical potential of carbon,  $\mu_C$ , is initially hypothetically infinite with respect to reactions (2.1) and (2.2), because initially  $p_{\text{CO}_2} = p_{\text{H}_2\text{O}} = 0$ .



and may thus be conceived as the first step of reactions (2.1) and (2.2). The removal of the adsorbed oxygen due to reaction (2.3) can occur for total reaction (2.1) according to:



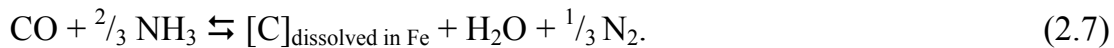
and for total reaction (2.2) according to



Since reaction (2.5) is considerable faster than reaction (2.4) [7], reaction (2.2) may provide the dominant pathway for the carbon uptake. The hydrogen needed for removal of the oxygen according to reaction (2.5) can be provided by the hydrogen in the gas atmosphere but also by the decomposition of ammonia:



leading to the total reaction:



Reaction (2.7) may play a crucial role to realise the growth of massive cementite layers, additionally to reaction (2.2), because, it provides an extra possibility for carbon transfer from the atmosphere to the solid. However, the nitriding potential (i.e. the chemical potential of nitrogen  $\mu_{\text{N}}$ ) must be sufficiently low in order to prevent the formation of iron (carbo-) nitrides.

### 2.3.2 Cementite layer-growths kinetics

To analyse the cementite layer-growth kinetics, the specimens of experiment series *B* were treated with a constant  $\text{NH}_3$  content of 13.2 vol.% ( $r_{\text{N}} = 0.3 \text{ atm}^{-1/2}$ ) in order to achieve massive cementite layers without sooting or the formation of iron-nitrides (cf. Fig. 2.3). Results of series *B* are shown in Fig. 2.4 where the squared cementite-layer thickness  $S^2$  has been plotted versus the treatment time  $t$ .

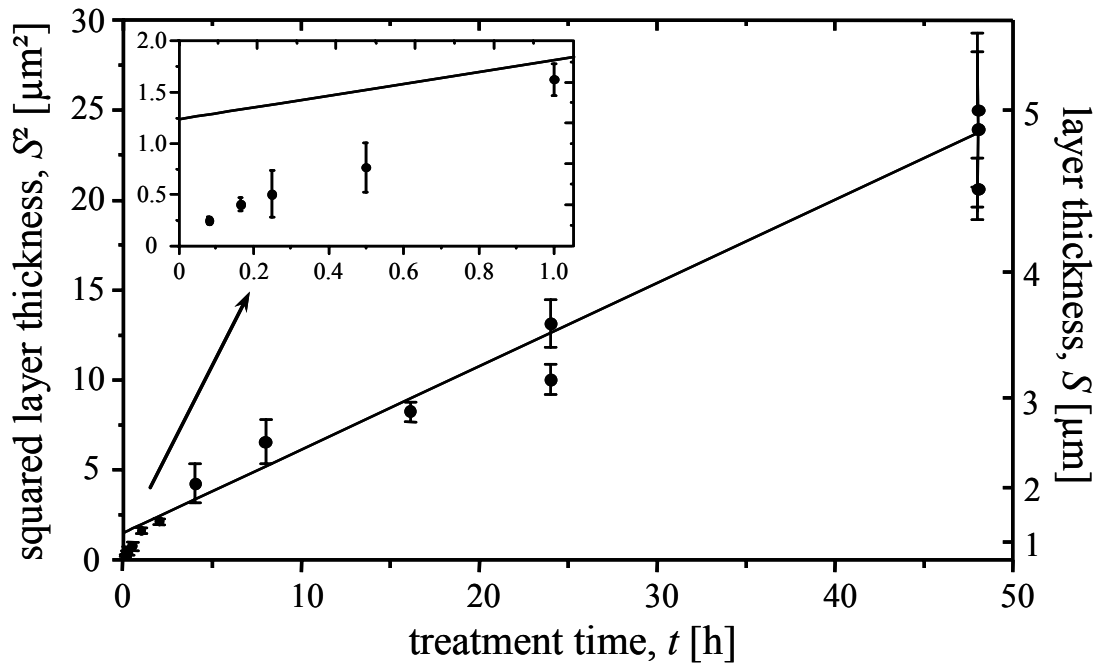


**Fig. 2.4:** The squared cementite-layer thickness versus the (nitro-) carburising time at 823 K for treatment in a gas mixture composed of 20.0 vol.% CO, 58.0 vol.% H<sub>2</sub>, 13.2 vol.% NH<sub>3</sub>, and 8.8 vol.% N<sub>2</sub> ( $r_{\text{N}} = 0.3 \text{ atm}^{-1/2}$ ). The straight line shown for stage II ( $t > 1 \text{ h}$ ) has been obtained by least-squares fitting of Eq. (2.8).

Occurrence of (carbon) volume-diffusion controlled growth would lead to a straight line through the origin in that plot. Clearly, for treatment times larger than 1 h parabolic, volume-diffusion controlled growth occurs, whereas for the shorter treatment times a faster growth rate occurs.

The initial, fast layer growth (stage I) may be caused by two effects. At the very beginning of the carburising treatment an incomplete, only fractionally closed cementite layer may be present and carbon can diffuse through ferrite (bypassing the cementite), which is much faster than the diffusion of carbon through the cementite (a similar bypassing effect has been discussed for  $\gamma'$ -Fe<sub>4</sub>N-layer growth on iron [16]). This ‘bypass’ growth mechanism can, in any case, contribute until, upon lateral growth, the cementite crystallites coalesce and form a continuous layer. Already after 5 min a complete cementite layer was observed. Thereafter, carbon diffusion may preferentially occur through especially thin and defect-rich parts of the just completed cementite layer with a high grain-boundary density (short-circuit diffusion). Thus

carbon could be transported relatively fast through the layer, as compared to volume diffusion.

Upon longer treatment times cementite crystallites may coarsen and/or defects become annihilated, leading to a microstructure not allowing substantial short-circuit diffusion, and thus the layer-growth rate decreases and becomes controlled by volume diffusion. Analysing the layer-thickness data as a function of time for  $t > 1$  h (stage II) in terms of

$$S^2(t) = k \cdot t + S_0^2, \quad (2.8)$$

with  $S_0$  as the hypothetical thickness at  $t = 0$  and  $k$  as the parabolic growth constant leads to values for  $S_0$  and  $k$  by (least-squares) fitting of a straight line through the data in Fig. 2.4. Thus an ‘initial’ layer thickness of about 1.2  $\mu\text{m}$  ( $S_0 > 0$ , because of the ‘bypass/short-circuit’ mechanism) and a growth constant of  $1.3 \times 10^{-16}$   $\text{m}^2/\text{s}$  were determined for the given carburising parameters. Comparison of the growth rate of the cementite layer with that of a  $\gamma'$ - $\text{Fe}_4\text{N}$  layer at the same temperature [9] indicates that the cementite layer grows much slower, leading to thinner compound layers at comparable treatment times.

## 2.4 Conclusions

1. Pure and massive cementite layers can be grown onto ferritic iron by carburising in gas atmospheres containing a certain amount of ammonia. The ammonia content in the atmosphere (consisting of 20 vol.% CO, 58 vol.%  $\text{H}_2$ ,  $22 - n$  vol.%  $\text{NH}_3$  and  $n$  vol.%  $\text{N}_2$ ) controls the phase composition of the compound layer: In a certain range of ammonia content the growth of cementite layers can be easily controlled, as required for practical applications. A too high amount of ammonia leads to the formation of iron (carbo-) nitrides, whereas a too low amount of ammonia leads to sooting at the surface.
2. Examination of the growth kinetics of the cementite layers revealed a two-stage process. In the beginning stage of cementite formation ( $t < 1$  h at 823 K) relatively fast layer growth occurs, which may be ascribed to e.g. (i) a fractionally complete

cementite layer ('bypassing' diffusion of carbon through ferrite) and (ii) short-circuit diffusion due to many defects such as cementite grain boundaries within the initially very thin layer. After that beginning stage of layer growth, massive cementite-layer growth obeys a parabolic, (likely carbon volume) diffusion-controlled growth law.

## References

- [1] Somers MAJ, Mittemeijer EJ. Surf Eng 1987;3:123.
- [2] Source Book on Nitriding, ASM, Metals Park, OH, 1977
- [3] Jack KH. Proc Roy Soc A 1948;195:41.
- [4] Naumann FK, Langenscheid G. Arch Eisenhüttenwes 1965;36:583.
- [5] Naumann FK, Langenscheid G. Arch Eisenhüttenwes 1965;36:677.
- [6] Du H, Somers MAJ, Ågren J. Met Trans A 2000;31:195.
- [7] Grabke HJ. Mater Corr 2003;54:736.
- [8] Umemoto M, Todaka Y, Takahashi T, Li P, Tokumiya R, Tsuchiya K. J Metastable and Nanocryst Mat 2003;15-16:607.
- [9] Mittemeijer EJ, Somers MAJ. Surf Eng 1997;13:483.
- [10] Chatterjee-Fischer R, et al. Wärmebehandlung von Eisenwerkstoffen, Expert Verlag, Renningen-Malmsheim, 1995.
- [11] Wells A. J Mat Sci 1985;20:2439.
- [12] Colijn PF, Mittemeijer EJ, Rozendaal HCF. Z Metallkde 1983;74:620.
- [13] Rozendaal HCF, Colijn PF, Mittemeijer EJ. Surf Eng 1985;1:30.
- [14] Schalkoord, D. M.Sc. Thesis, Delft University of Technology (1973).
- [15] La Pouchau JL, Pichoir F. Rech Aerospatial 1984;3:167
- [16] Somers MAJ, Mittemeijer EJ. Met Trans A; 1995;26:57.
- [17] Kagawa A, Okamoto T. Trans Jap Inst Met 1981;22:137.
- [18] Wood IG, Vocadlo L, Knight KS, Dobson DP, Marshall, WG, Price GD, Brodholt J. J Appl Cryst 2004;37:82.
- [19] Sone T, Tsunasawa E, Yamanaka K. Trans Jap Inst Met 1981;22:237.
- [20] Demchenko L, Sidorenko S, Tinyaev V. Def Diff Forum 2003;216-217:87.
- [21] Schneider A, Grabke HJ. Mater Corr 2003;54:793.
- [22] Cowan RJ, Bryce JT. Trans Amer Soc Metals 1938;26:766.



***X-ray diffraction line-profile analysis of hexagonal  $\epsilon$ -iron-nitride compound layers: composition- and stress-depth profiles***

*T. Greßmann, A. Leineweber, E.J. Mittemeijer*

**Abstract**

Two hexagonal  $\epsilon$ -Fe<sub>3</sub>N<sub>1+x</sub> layers grown on  $\alpha$ -Fe substrates by nitriding in NH<sub>3</sub>/H<sub>2</sub> gas atmospheres were investigated by high-resolution X-ray powder diffraction using synchrotron radiation employing systematic tilting of the diffraction vector with respect to the specimen surface. The obtained complicatedly shaped diffraction profiles, considering all recorded reflections simultaneously, were analysed using a model incorporating  $hkl$ -dependent (anisotropic) and tilt-angle ( $\psi$ ) dependent diffraction-line broadening and diffraction-line shifting. The diffraction-line broadening is mainly ascribed to the nitrogen concentration-depth profile within the layers causing depth-dependent strain-free lattice parameters, whereas the line shifts are predominantly caused by the stress-depth profile originating from the concentration-dependence of the coefficients of thermal expansion of the  $\epsilon$  phase, with stress parallel to the surface which is of tensile nature at the surface and of compressive nature at the  $\epsilon/\gamma'$  interface. This stress gradient additionally leads to a  $\psi$ -dependence of the line broadening. Fitting of the microstructure and diffraction model led to determination of microstructure parameters, which can be related to the different sets of treatment conditions applied for the  $\epsilon$ -iron-nitride layer growth.

### 3.1 Introduction

In the field of materials science there is a great demand for methods for depth-dependent characterisation of the microstructure of polycrystalline thin films and surface layers, especially recognising that in many specimens/workpieces the properties change with depth. Depth profiling by determination of depth-dependent (micro-)structural features (e.g. lattice parameters – associated with composition, macrostresses, microstresses, crystallite size), is often realised in a destructive manner either by cutting a piece out of the specimen/workpiece of interest and investigation of the thus produced cross section (e.g. by electron probe microanalysis (EPMA)), or by successive removal of sublayers of material from the surface by methods like polishing and analysis of the occurring surface or near surface volume (e.g. by means of X-ray diffraction (XRD)) [1]. These types of depth profiling are destructive and, moreover, upon removal of material from the surface the characteristics of the investigated material may change, e.g. a redistribution of stress in the remaining material occurs because of the requirement of mechanical equilibrium and also stress may be induced by the removal of material. Hence, a non-destructive method is desired. The method developed and applied in this work is based on non-destructive high-resolution X-ray powder-diffraction analysis: The positions and full shapes of diffraction-line profiles recorded under variation of the orientation of the diffraction vector with respect to the surface are interpreted in terms of an absorption-weighted superposition of the diffraction effects in the detected signal arising from different depths and as influenced by changes in composition and stress.



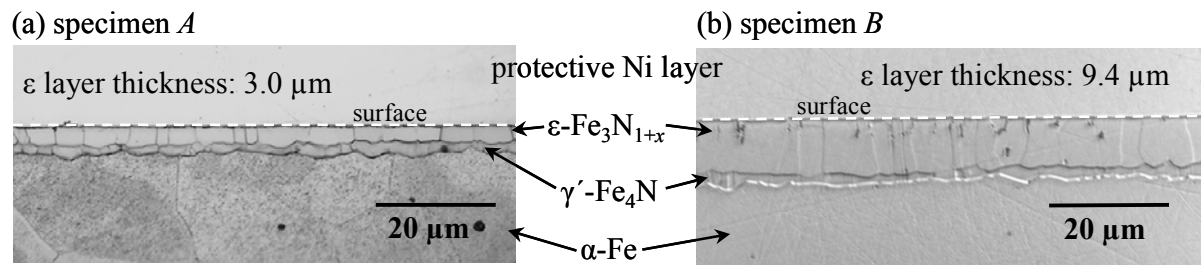


**Fig. 3.1:** Optical micrographs (bright field) of compound-layer cross sections (after Nital etching) of the analysed gas nitrated  $\alpha$ -iron specimens, consisting of an outer  $\epsilon$ - $\text{Fe}_3\text{N}_{1+x}$  layer and an inner  $\gamma'$ - $\text{Fe}_4\text{N}$  layer: (a) specimen A (1.5 h, 823 K, 56/44 vol.%  $\text{NH}_3/\text{H}_2$ ), (b) specimen B (5.0 h, 823 K, 60/40 vol.%  $\text{NH}_3/\text{H}_2$ )

The system iron-nitrogen is not only scientifically of great interest in metallurgy but also plays an important role in technology [2, 3]: in particular iron-nitride phases as surface layers on iron or steel workpieces are of great importance, since they can improve the corrosion resistance and the tribological properties of the surface region [4, 5]. Iron-nitride phases are typically generated by nitriding iron or steel in  $\text{NH}_3/\text{H}_2$  gas mixtures at temperatures between 773 K and 863 K. During the nitriding process the  $\alpha$ -iron substrate becomes enriched with nitrogen and, if the chemical potential of nitrogen in the applied gas mixture is sufficiently high, a compound layer forms composed of an outer surface-adjacent  $\epsilon$ - $\text{Fe}_3\text{N}_{1+x}$  sublayer (for the  $\epsilon$  phase also formulas like  $\text{Fe}_2\text{N}_{1-z}$  and  $\text{FeN}_y$  with  $y = (1 + x)/3$  are used in literature) and an inner  $\gamma'$ - $\text{Fe}_4\text{N}$  sublayer adjacent to the  $\alpha$ -iron substrate (Fig. 3.1)<sup>3.1</sup>. Both, the  $\epsilon$  and the  $\gamma'$  phase contain a close-packed stacking of the iron atoms, with *hcp* for  $\epsilon$  and *fcc* for  $\gamma'$ , in which the nitrogen atoms occupy octahedral interstitial sites in a more or less long-range ordered fashion [6-10]. Especially the  $\epsilon$  phase is of great interest, since its homogeneity range is quite large, e.g. at 823 K from about 24 at.% N to about 33 at.% N [11] (Fig. 3.2). These concentration variations are associated with considerable variations of the lattice parameters  $a$  and  $c$ . It is well known that within the  $\epsilon$  layer a concentration gradient builds up during the nitriding process due to the inward diffusion of nitrogen from the gas atmosphere to the bulk [12], with *higher*

<sup>3.1</sup> For nitriding steels, composed of many different alloying elements, often no clear distinction between the sublayers is possible.

nitrogen contents at the surface of the specimen and with *lower* nitrogen contents at the  $\epsilon/\gamma'$  interface, implying a strong depth dependence of the lattice parameters. Various dependencies of the lattice parameters on the composition of the  $\epsilon$  phase have been reported [7, 13-18]. The data from the different sources vary considerably. Furthermore, it was shown recently that the lattice parameters depend not only on the nitrogen content but also to a significant extent on the degree of nitrogen ordering induced by the type of cooling procedure employed after nitriding or heat treatment [18].

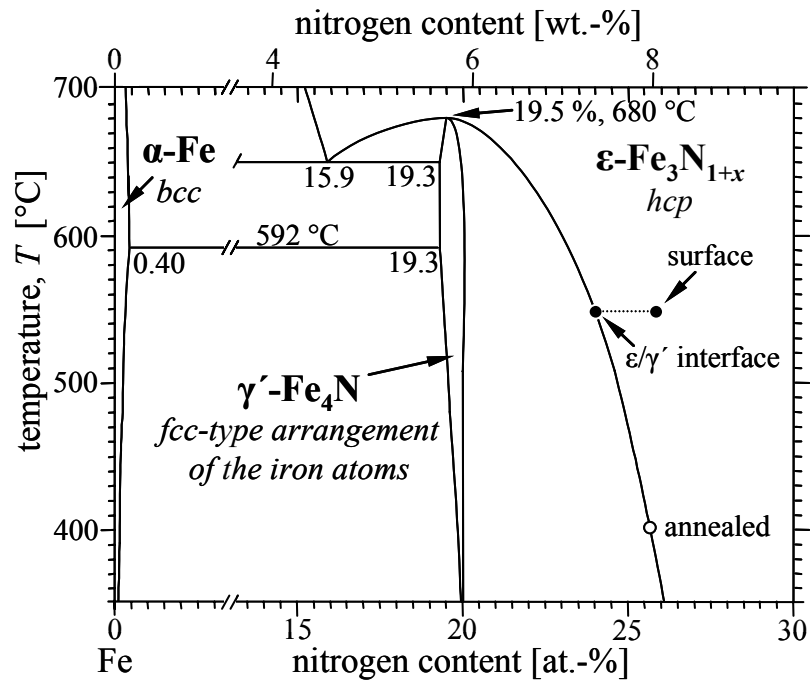


**Fig. 3.2:** Part of the metastable Fe-N phase diagram [11]. Note the break at the abscissa. The filled points connected by the dashed line indicate the nitrogen contents of  $\epsilon$  compound layers at the surface (approximately; in equilibrium with the gas phase) and at the  $\epsilon/\gamma'$  interface, as expected for nitriding at 823 K. The concentration-depth profile in the  $\epsilon$  layer is due to the inward diffusion of nitrogen during the nitriding process. The nitrogen content of the annealed (at 673 K), homogenised reference sample, used for the line-broadening contribution  $f'$ , has been indicated by the open circle.

Additional to the concentration gradient, a macrostress-depth profile will likely build up within the  $\epsilon$  layer. Residual macrostresses can arise when different parts/phases of a cohesive specimen tend to assume different volumes. Thus concentration-depth profiles and misfit between layer and substrate can induce a state of stress in a surface layer. Detailed information on and fundamental understanding of

the macrostresses present in  $\epsilon$  layers lacks. Until now a few publications provide data on macrostresses in  $\epsilon$  layers, unfortunately mostly dealing with steels nitrided by commercial treatments without giving much detail [19-21], which hinders a straightforward interpretation of the obtained results. The work by Somers and Mittemeijer, 1992 [21] can be regarded as the most comprehensive one, dealing also with pure nitride compound layers on pure  $\alpha$ -iron. In all previous works only diffraction-line (peak) positions were analysed. The present work deals with non-destructive *high-resolution X-ray powder-diffraction* investigation of hexagonal  $\epsilon$ - $Fe_3N_{1+x}$  layers grown on top of  $\alpha$ -iron substrates by gas nitriding, thereby allowing detailed (shape) analysis of the full line profiles. A model for the microstructure has been developed which, upon fitting to the diffraction data, leads to determination of the depth profiles of the macrostrain-free lattice parameters and the macrostress, simultaneously considering several *hkl*-reflections recorded at different specimen tilt angles  $\psi$ .

## 3.2 Experimental

### 3.2.1 Specimen preparation

Iron rods were prepared from pure iron (Alfa Aesar, 99.98 wt.%) in an inductive furnace under argon atmosphere (99.999 vol.%). The casts were cold-rolled to plates of about 1 mm thickness. These sheets were cut into rectangular pieces (20 mm  $\times$  25 mm) and annealed for 2 h at 973 K under flowing hydrogen to obtain a recrystallised grain structure. Before nitriding the specimens were ground, polished (last step: 1  $\mu$ m diamond paste) and cleaned in ethanol in an ultrasonic bath.

For nitriding the specimens were suspended by quartz fibres in the middle of a vertical quartz-tube furnace equipped with a water container for quenching. The nitriding experiments were performed in  $NH_3$  (99.999 vol.%) /  $H_2$  (99.999 vol.%) gas mixtures at 823 K. The fluxes of both gases were adjusted using mass-flow controllers and amounted together to 500 ml/min (referring to the gas volume at room temperature), which corresponds to a linear gas velocity of 13.5 mm/s through the quartz retort (diameter 28 mm), which is sufficiently high in order to minimise the

effect of ammonia decomposition. After the thermochemical heat treatments the quartz fibres were cut within the furnace and thus the specimens were quenched by dropping into water at room temperature flushed with  $N_2$ . The treatment parameters of the two analysed specimens, further denoted as specimen *A* and *B*, have been listed in Table 3.1.

**Table 3.1:** Nitriding parameters for specimens *A* and *B* treated both at 823 K, the corresponding nitriding potential\*,  $r_N = p_{NH_3} / p_{H_2}^{3/2}$ , the measured  $\epsilon$ -layer and  $\gamma'$ -layer thicknesses and the according to the nitriding conditions expected nitrogen content in the  $\epsilon$  phase at the surface [22] and at the  $\epsilon/\gamma'$  interface [12].

Specimen	Treatment time [h]	NH <sub>3</sub> content [vol.%]	H <sub>2</sub> content [vol.%]	Nitriding potential $r_N$ [atm <sup>-1/2</sup> ]	$\epsilon$ -layer thickness [ $\mu$ m]	$\gamma'$ -layer thickness [ $\mu$ m]	Maximum N content at the surface [at.% N]	Minimum N content at the $\epsilon/\gamma'$ interface [at.% N]
<i>A</i>	1.5	56	44	1.92	3.0	1.8	25.7	24.1
<i>B</i>	5.0	60	40	2.37	9.4	1.3	26.2	24.1

\* The nitriding potential  $r_N$  is commonly used to quantify the chemical potential of nitrogen in  $NH_3/H_2$  gas mixtures, which is considerable higher than that of molecular  $N_2$  [23].

Specimen *B* was subdivided into two parts of equal size. One part was subjected to a subsequent heat treatment in order to remove by homogenisation the concentration gradient within the  $\epsilon$  layer [24]. To this end this part of the specimen was encapsulated into a quartz tube under residual Ar pressure (300 mbar). The annealing occurred in a salt bath at 673 K for 1 d. After the heat treatment the specimen was quickly removed from the salt bath and quenched by throwing the tube (without crushing) into cold water. During the homogenisation process the nitrogen concentration of the  $\epsilon$  phase in the specimens adjusts to the value pertaining to equilibrium of  $\epsilon$  with  $\gamma'$  according to the phase diagram (Fig. 3.2) [25].

### **3.2.2 Metallography**

For light-optical microscopy a small part of each specimen was cut and covered with a protective nickel layer by electrodeposition using a Watts bath [26, 27] at 333 K in order to avoid curvature and damaging close to the surface of the specimen during subsequent metallographic handling. Next, the pieces were embedded (Polyfast, Buehler GmbH), ground, polished (last step: 1  $\mu$ m diamond paste) and finally etched using 1 vol.% Nital containing 0.1 vol.% HCl [28]. Light-optical microscopy was performed with a Leica DMRM microscope. For each specimen several cross-sectional micrographs were taken close to both faces of the specimens. The layer thicknesses were determined from these micrographs: the measured area of the layer was divided by the measured lateral length of the layer, yielding the layer thickness (Table 3.1). The values of several micrographs were arithmetically averaged [24]. By this method the effect of the slight interface roughness is averaged out.

### **3.2.3 TEM and EBSD**

High-resolution transmission electron microscopy (TEM) and electron back-scattering diffraction (EBSD) were performed to investigate the orientation relationship between the  $\epsilon$  and the  $\gamma'$  layer. TEM on cross-sections at the  $\epsilon/\gamma'$  interface region was carried out using a JEOL JEM-4000FX (400 kV) transmission electron microscope. The preparation procedure of the TEM foils is described elsewhere [29, 30]. For EBSD measurements, performed on cross-sections, the specimens were embedded, ground and polished (last step: colloidal silica suspension OPS, Struers GmbH, for several hours). EBSD was carried out using a Zeiss scanning electron microscope equipped with an EBSD system (TSL, EDAX, Inc.). Indexing and analysis of the recorded Kikuchi patterns was done using the software OIM 3.5.

### **3.2.4 X-ray diffractometry**

High-resolution X-ray powder-diffraction analysis was carried out at the synchrotron beamline B2, HASYLAB, Hamburg. The station was equipped with a Eulerian cradle and used in direct beam configuration [31]. The wavelength was adjusted to 0.80017 Å, in order to achieve a relatively low X-ray absorption (cf. section 3.3.2). The cross-section of the beam was set to 5 mm  $\times$  1 mm, in order to ensure that the

whole beam hits the surface of the specimen and that as much surface area as possible is illuminated for all applied specimen orientations. The diffracted beam passed a Ge(111) analyser crystal before being detected by a NaI scintillation counter. During the measurements the samples were rotated around the surface normal in order to achieve better crystallite statistics (rotational symmetry of the state of stress within the plane of the specimen was assumed:  $\sigma_{//} \equiv \sigma_{11} = \sigma_{22}$ ). For stress measurements the diffractometer was used in  $\chi$  mode<sup>3.2</sup> [32, 33] in symmetrical diffraction geometry and the applied specimen tilt angles  $\psi$  ranged from  $0^\circ$  to  $60^\circ$ . The step size in  $2\theta$  was varied  $hkl$  dependently between  $0.002^\circ$  and  $0.008^\circ$ . The following 9 reflections pertaining to the  $\epsilon$  phase were recorded for both specimens in the ‘as-nitrided’ state by measuring over sufficiently large  $2\theta$  subranges: 110, 002, 111, 112, 300, 113, 302, 223 and 304. These  $hkl$  refer to the hexagonal superstructure with  $a = 3^{1/2}a_{hcp}$  and  $c = c_{hcp}$ ; the index  $hcp$  refers to the unit cell of the  $hcp$  type arrangement of the iron atoms. Weak superstructure reflections due to nitrogen ordering were not considered in the measurements. Additionally, selected reflections of SRM660a LaB<sub>6</sub> (NIST, USA) were measured as a standard to determine the instrumental resolution, as well as reflections were recorded from the annealed, homogenised part of specimen *B* for determining the remaining diffraction-line broadening due to thermal misfit induced microstresses (see section 3.3.3) of homogenised  $\epsilon$ -Fe<sub>3</sub>N<sub>1+x</sub> layers.

---

<sup>3.2</sup>  $\chi$  is the angle of rotation of the sample around the axis defined by the intersection of the diffraction plane and sample surface, i.e. perpendicular to the  $\theta/2\theta$  plane;  $\chi$  coincides in  $\chi$  mode with the angle  $\psi$ .

### 3.3 Theoretical considerations

#### 3.3.1 Model for the microstructure of $\epsilon$ layers

The microstructure of *hcp*  $\epsilon$ -Fe<sub>3</sub>N<sub>1+x</sub> layers can be modelled recognising that at each depth below the surface a plane of constant lattice parameters and a constant state of stress is present and adopting an ideally flat  $\epsilon/\gamma'$  interface.

##### 3.3.1.1 Lattice-parameter-depth profile

Compositional variations within a single, crystalline phase are generally associated with lattice-spacing variations. According to the applied nitriding conditions relatively large depth( $z$ )-dependent nitrogen-concentration variations are expected to be present within the  $\epsilon$  layers (cf. Table 3.1), implying depth-dependent hexagonal lattice parameters  $a(z)$  and  $c(z)$ . Then, for each  $hkl$ , the corresponding depth-dependent lattice spacing  $d_{hkl}(z)$  can be calculated according to:

$$d_{hkl}^{-2}(z) = \frac{4}{3}a^{-2}(z)(h^2 + k^2 + hk) + c^{-2}(z)l^2. \quad (3.1)$$

Composition dependencies of  $a$  and  $c$  are known, as e.g. reported in Refs. [17, 18]. Also a significant degree-of-order (in the nitrogen superstructure) dependence of  $a$  and  $c$  has been reported [18]. In order to allow maximum flexibility in the model, the strain-free lattice parameters  $a$  and  $c$  are allowed to vary independently (see section 3.4.3).

The  $\epsilon$  layers of thickness  $Z$  were considered to be composed of a sufficient number of  $n$  sublayers ( $n = 5$  for sample *A* and  $n = 8$  for sample *B*) of equal thickness,  $\delta z = Z/n$ <sup>3.3</sup>. Thus, the sublayer/sublayer interfaces, further denoted as grid points (GP in Figs. 3.3 and 3.4), are located at depth  $z_j = j\delta z$ , with  $j = 0, 1, \dots, n$ , below the specimen surface (Fig. 3.3). The lattice parameters are assumed to decrease monotonously with increasing distance to the surface and at the grid points have values  $a(j)$  and  $c(j)$ . The  $j^{\text{th}}$  sublayer occurs between the grid points  $j - 1$  and  $j$ . Within a sublayer the lattice parameters  $a$  and  $c$  are assumed to vary linearly between their

---

<sup>3.3</sup>  $\delta X$  denotes the *change* of a variable/function  $X$  over a sublayer  $j$  ( $\delta X(j)$ ), e.g.  $\delta z$ ,  $\delta d_{hkl}(j)$  or  $\delta d_{hkl}^{-2}(j)$  (see Figs. 3.3 and 3.4) or over the whole  $\epsilon$  layer ( $\delta X$  with superscript 'total').

values at the adjacent grid points, leading to a partitioning of the functions  $a(z)$  and  $c(z)$  over the whole layer. The  $d$  spacing at the grid points and the partitioned function  $d_{hkl,0}(z)$  can then be calculated straightforwardly from the corresponding values from the lattice parameters  $a$  and  $c$  using Eq. (3.1)<sup>3,4</sup>.

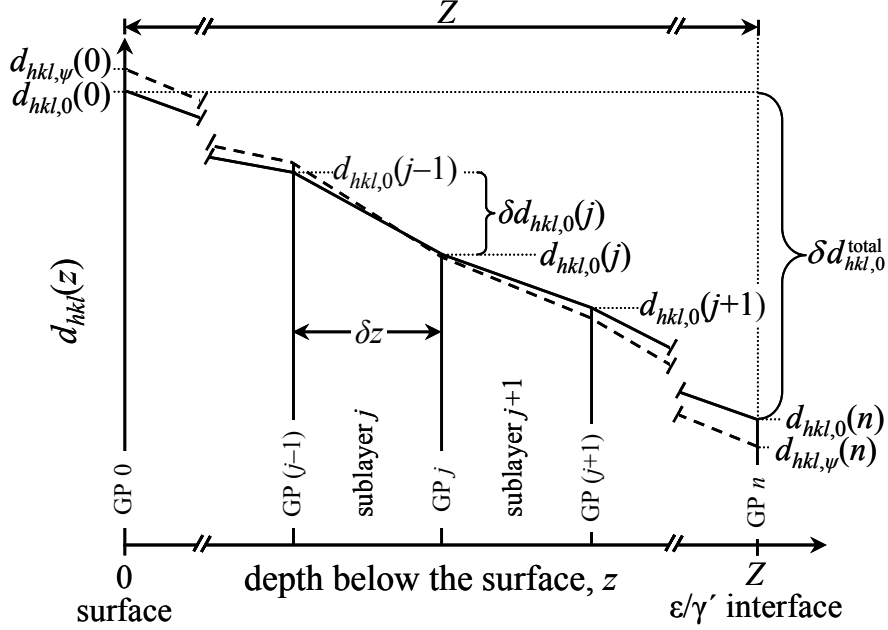


**Fig. 3.3:** Schematic illustration of the partitioning of the  $\epsilon$ - $\text{Fe}_3\text{N}_{1+x}$  compound layer (total thickness  $Z$ ) into  $n$  sublayers of equal thickness  $\delta z = Z/n$ . The strain-free lattice spacings  $d_{hkl,0}$  at the grid points GP ( $j = 0, 1, \dots, n$ ) decrease with increasing distance to the surface due to the corresponding decrease of nitrogen content. Within the sublayers ( $j = 1, 2, \dots, n$ ) the lattice spacings are taken to depend linearly on depth. Variation of the tilt angle  $\psi$  leads to variation of the observed lattice spacing (see dashed line for  $d_{hkl,\psi}$ ) as due to the presence of an (assumedly linear) stress-depth profile.

<sup>3,4</sup> Small changes  $\delta a(j) = a(j) - a(j-1)$  and  $\delta c(j) = c(j) - c(j-1)$  with respect to  $a(j-1)$  and  $c(j-1)$ , as well as linear dependence on depth of  $a$  and  $c$  within the sublayers leads to an, also, practical linear dependence on depth of  $d_{hkl}^{-2}(z)$  and  $d_{hkl}(z)$  within each sublayer.



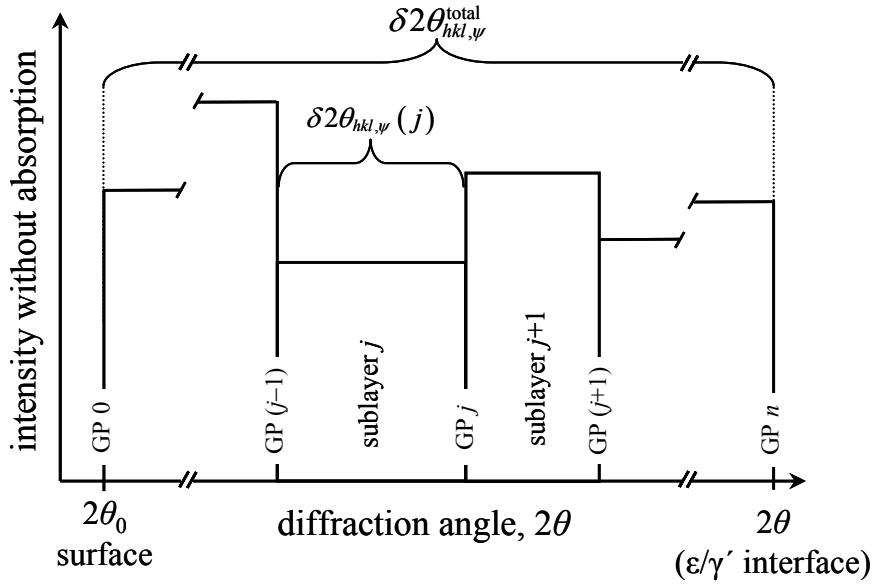


**Fig. 3.4:** Theoretically expected constitution of the diffraction-line profile of reflection  $hkl$  at a tilt angle  $\psi$  originating from the partitioning of the  $\epsilon$  layer (neglecting here for simplicity the effect of X-ray absorption, which additionally occurs): all sublayers give rise to the same integrated intensity. Assuming that each slice of lattice spacing  $d_{hkl,\psi}$  diffracts independently and since each sublayer has its own lattice-spacing variation, different subprofile breadths and heights on the diffraction-angle scale  $2\theta$  occur.

### 3.3.1.2 Stress-depth profile

The compound layers are produced by gas nitriding of polycrystalline substrates and thus the  $\epsilon$  layers should exhibit a rotationally symmetric biaxial state of stress parallel to the surface of the specimen, i.e.  $\sigma_{//} \equiv \sigma_{11} = \sigma_{22}$  (similar to the observations made in Ref. [34] on  $\gamma'$  layers). Effects originating from the edges of the specimens can be ignored for the irradiated area in the experiment. The stress is assumed to change linearly with depth within the layers so that at the grid points  $j$  the stress corresponds to

$$\sigma_{//}(j) = \sigma_{//}(j=0) + \frac{j\delta z}{Z} \delta\sigma_{//}^{\text{total}}, \quad (3.2)$$

where  $\sigma_{//}(j=0)$  denotes the stress value at the surface of the specimen and  $\delta\sigma_{//}^{\text{total}}$  represents the total change in stress over the whole layer. Such a macrostress-depth profile,  $\sigma_{//}(z)$ , leads to  $\psi$ - and depth-dependent mechanical strains and lattice spacings

$d_{hkl,\psi}(z)$ , where  $\psi$  is the specimen-tilt angle (angle between surface normal and diffraction vector; see also footnote 3.2).

It can be shown that  $d_{hkl,\psi}$  depends linearly on  $\sin^2\psi$  (e.g. see Ref. [32]):

$$d_{hkl,\psi}(j) = \left[ (2S_1^{hkl} + \frac{1}{2}S_2^{hkl} \sin^2\psi) \sigma_{//}(j) + 1 \right] d_{hkl,0}(j), \quad (3.3a)$$

where  $d_{hkl,0}$  denotes the strain-free lattice spacing and  $S_1^{hkl}$  and  $\frac{1}{2}S_2^{hkl}$  are the so-called X-ray elastic constants (XECs). The calculated single-crystal elastic constants (SECs) of stoichiometric  $\epsilon$ -Fe<sub>3</sub>N indicate a very small intrinsic elastic anisotropy (see Appendix) which will be neglected here<sup>3.5</sup>. In that case the X-ray elastic constants (XECs) are independent of  $hkl$  and Eq. (3.3a) can be written as

$$d_{hkl,\psi}(j) = \left[ \left( -2\frac{\nu}{E} + \frac{1+\nu}{E} \sin^2\psi \right) \sigma_{//}(j) + 1 \right] d_{hkl,0}(j), \quad (3.3b)$$

with  $E$  as Young's modulus and  $\nu$  as Poisson ratio.

### 3.3.2 Diffraction effects of the microstructure model

The intrinsic diffraction-line profiles of the  $\epsilon$  layers can in principle (see below) be calculated on the basis of the microstructure model described in section 3.3.1. This leads to a line profile, denoted here as  $f''$ , which has to be convoluted with line-profile contributions  $g$  and  $f'$  as described in section 3.3.3, to obtain the overall diffraction pattern that can be considered as a simulation of the experimentally recorded one.

For calculation of the intrinsic diffraction-line profile  $f''$  it is assumed that each – infinitesimally thin – slice of the  $\epsilon$  layer with a given lattice spacing  $d_{hkl,\psi}$  diffracts independently and produces its own diffraction subline profile. Coherency effects (of diffraction) are not considered, i.e. the integrated (diffracted) intensities of the slices are additive.

The layer consists mainly of columnar grains; viz.  $\epsilon$ - $\epsilon$  grain boundaries are generally perpendicular to the surface of the specimen (see section 3.4.1) and thus a

---

<sup>3.5</sup> Application of calculated  $hkl$ -dependent XECs (used as  $S_1^{hkl}$  and  $\frac{1}{2}S_2^{hkl}$  in Eq. (3.3a)) recognising the slight anisotropy of the SECs and calculated using different methods for grain interaction (e.g. Reuss, Voigt [35, 36]) did not lead to an improvement of the fitting results described in section 3.4.3.

possible texture can be taken as depth independent. Finally, it is assumed that the scattering power of the iron nitride does not vary with depth recognising the modest changes in nitrogen content and correspondingly modest changes of unit-cell volume and the structure factor.

The diffraction angle at which the diffraction contribution of a reflection  $hkl$ , at a given  $\psi$ , pertaining to a slice at grid point  $j$  occurs is given by

$$2\theta_{hkl,\psi}(j) = 2\theta_{hkl,\psi}(j=0) + \sum_{j'=1}^j \delta 2\theta_{hkl,\psi}(j'), \quad (3.4)$$

where the reflection shift  $\delta 2\theta_{hkl,\psi}(j) = 2\theta_{hkl,\psi}(j) - 2\theta_{hkl,\psi}(j-1)$  over the sublayer  $j$  can

be calculated by using Bragg's law:  $\delta 2\theta_{hkl,\psi}(j) = -2 \frac{\delta d_{hkl,\psi}(j)}{d_{hkl,\psi}(j)} \tan \theta_{hkl,\psi}(j)$ . Because

$$-2 \delta d_{hkl,\psi}(j) / d_{hkl,\psi}(j) = \delta d_{hkl,\psi}^{-2}(j) / d_{hkl,\psi}^{-2}(j) \approx \delta d_{hkl,\psi}^{-2}(j) / d_{hkl,\psi}^{-2}(j=0) \text{ and}$$

$\tan \theta_{hkl,\psi}(j) \approx \tan \theta_{hkl,\psi}(j=0)$  it is finally obtained:

$$\delta 2\theta_{hkl,\psi}(j) = \frac{\delta d_{hkl,\psi}^{-2}(j)}{d_{hkl,\psi}^{-2}(j=0)} \times \tan \theta_{hkl,\psi}(j=0). \quad (3.5)$$

The total line width  $\delta 2\theta_{hkl,\psi}^{\text{total}}$  is given by the sum of the line-width contributions of the sublayers,  $\sum_{j=1}^n \delta 2\theta_{hkl,\psi}(j)$  (Fig. 3.4).

Neglecting at first the effect of X-ray absorption, (i) the integrated intensity originating from each sublayer is the same, since the amount of diffracting material is the same for each sublayer, and (ii) the intensity diffracted by the sublayer is distributed homogeneously over the width  $\delta 2\theta_{hkl,\psi}(j)$ , since the lattice-spacing gradient is virtually constant within the sublayer due to the linear variation of  $a$  and  $c$  and of the strain (see section 3.3.1) and the relation between  $d$  and  $2\theta$  is approximately linear for small ranges in  $d$  and  $2\theta$  (cf. Bragg's law). Since the grid points, for a given  $hkl$  and  $\psi$ , are not equidistantly distributed on the  $2\theta$  scale, the same amount of integrated intensity (again ignoring the absorption of X-rays) is distributed over different diffraction-angle ranges  $\delta 2\theta_{hkl,\psi}(j)$  (Fig. 3.4): The smaller the lattice-parameter

variation over a sublayer  $j$  is, the smaller  $\delta 2\theta_{hkl,\psi}(j)$  and the higher the intensity of the sublayer are in the composite reflection  $hkl$ . The relative intensity (height) originating from sublayer  $j$  is given by the factor  $[\delta d_{hkl,\psi}^{-2}(j)]^{-1}$  (cf. Eq. (3.5)).

The X-rays are absorbed along their way through the  $\varepsilon$  layer. Therefore, the diffracted intensity originating from a depth  $z$  below the surface gets attenuated according to

$$I(z) = I_s \exp(-\mu(\lambda)k_\psi z), \quad (3.6)$$

where  $I(z)$  denotes the observed intensity pertaining to (the slice at) depth  $z$  below the surface and  $I_s$  represents the intensity at the state of reference (slice at the surface of the specimen).  $\mu(\lambda)$  is the (effective) linear absorption coefficient of the traversed material pertaining to the applied wavelength  $\lambda$  and  $k_\psi$  is a diffraction-geometry dependent factor, which reads for the applied diffraction geometry  $k_\psi = 2/(\sin \theta \cos \psi)$ . The value of  $\mu(\lambda)$  can be calculated as a composition-weighted sum of the linear absorption coefficients of Fe and N for  $\text{Fe}_3\text{N}$  at  $\lambda = 0.80017 \text{ \AA}$ ; i.e.  $\mu_{\text{Fe}_3\text{N}}(0.8 \text{ \AA}) = 0.035 \text{ \mu m}^{-1}$  [37]. It is assumed that for the modest compositional variations of the  $\varepsilon$  layers  $\mu(\lambda)$  can be taken as constant.

### 3.3.3 Data-evaluation method

The total line profiles  $h$  of the  $\varepsilon$  layers were calculated as the convolution of three different contributions:

$$h = g \otimes f' \otimes f'', \quad (3.7)$$

where  $g$  represents the instrumental broadening contribution, where  $f'$  denotes a physical  $hkl$ -dependent structural broadening contribution typical for even homogeneous  $\varepsilon$ -iron nitrides [38] (see below), and where  $f''$  denotes the intrinsic, structural broadening contribution according to the model for the microstructure described in sections 3.3.1 and 3.3.2.

The contributions  $g$  and  $f'$  for the different measured reflections were described by split pseudo-Voigt ( $spV$ ) functions similar as reported by Liapina *et al.*, 2006 [38], i.e. by

$$g_{hkl}(x), f'_{hkl}(x) = \frac{(1-\eta_{hkl}^{g,f'})}{B_{hkl}^{g,f'}} \sqrt{\frac{\ln 16}{\pi}} \exp\left(-\frac{\ln 16 \times x^2}{(B_{hkl}^{g,f'})^2 (1 \pm As_{hkl}^{g,f'})^2}\right) + \frac{2\eta_{hkl}^{g,f'}}{\pi B_{hkl}^{g,f'} (4x^2 / ((B_{hkl}^{g,f'})^2 (1 \pm As_{hkl}^{g,f'})^2) + 1)}, \quad (3.8)$$

with  $x = 2\theta_{hkl} - 2\theta_{0,hkl}$  ( $2\theta_{0,hkl}$ : fitted peak maximum) and  $B_{hkl}^{g,f'}$  denotes the full width at half maximum (FWHM).  $As_{hkl}^{g,f'}$  and  $\eta_{hkl}^{g,f'}$  are peak shape parameters, where  $\eta_{hkl}^{g,f'}$  is a mixing parameter leading for  $\eta_{hkl}^{g,f'} = 0$  to Gaussian broadening and for  $\eta_{hkl}^{g,f'} = 1$  to Lorentzian broadening, and  $\pm As_{hkl}^{g,f'}$  quantifies the peak asymmetry with ‘-’ for  $x > 0$  and ‘+’ for  $x < 0$ . The instrumental broadening  $g$  was determined from the reflections measured on the LaB<sub>6</sub> standard powder at  $\psi = 0^\circ$  (measurements at  $\psi = 30^\circ$  and  $\psi = 60^\circ$  were also conducted, indicating no significant  $\psi$  dependence of the peak shapes): Diffraction-angle dependent polynomials for  $B^g$ ,  $As^g$  and  $\eta^g$  were determined on the basis of  $B_{hkl}^g$ ,  $As_{hkl}^g$  and  $\eta_{hkl}^g$ , which allows to determine the instrumental broadening at an arbitrary diffraction angle, as required for analysis of the diffraction data from the  $\varepsilon$ -iron-nitride layers.

The contribution  $f'$  was determined from the homogenised  $\varepsilon$  layer. For each recorded reflection  $hkl$  of this layer the instrumental-broadening function  $g$  (pertaining to the corresponding diffraction angle, see above) was convoluted with a split pseudo-Voigt function to describe  $f'_{hkl}$  according to Eq. (3.8). Then by fitting  $g \otimes f'$  to the measured reflection of the homogenised  $\varepsilon$  layer values for  $B_{hkl}^{f'}$ ,  $As_{hkl}^{f'}$  and  $\eta_{hkl}^{f'}$  were obtained. It was found that the  $hkl$  dependence of  $B_{hkl}^{f'}$  and  $As_{hkl}^{f'}$  resembles that of the ‘residual’ diffraction-line broadening observed previously for homogenised  $\varepsilon$ -iron-nitride powders of composition similar to the present homogenised  $\varepsilon$  layer [38].

The  $\varepsilon$  reflections of the homogenised part of specimen  $B$  (data not shown) are much narrower than the  $\varepsilon$  reflections recorded from the layers in the ‘as-nitrided’ state, but are significantly broader than those of the standard LaB<sub>6</sub> at similar  $2\theta$  values. The

broadening of the profile  $f'$  is of microstrain-like character (the line width of a series of higher-order reflections increases with  $\tan\theta_{hkl}$ ), and is strikingly asymmetric and anisotropic: reflections at and close to  $\varphi_{hkl} = 0^\circ$  ( $\varphi_{hkl}$  is the angle of the diffraction vector with the [001] direction of the diffracting crystallites; e.g.  $\varphi_{hkl} = 0^\circ$  for 00 $l$  reflections) show low-angle tails, whereas reflections at and close to  $\varphi_{hkl} = 90^\circ$  (e.g. 110, 300) show high-angle tails. The microstrain in the direction of the diffraction vector has maximum values at  $\varphi_{hkl} = 0^\circ$  and  $\varphi_{hkl} = 90^\circ$ . A minimum of microstrain occurs at  $\varphi_{hkl} \approx 45^\circ$ . The  $hkl$ -dependent, anisotropic and asymmetric line-broadening contribution  $f'$  may be understood to be due to minor compositional variations within the homogenised  $\varepsilon$  layer (unlikely) and/or to be caused by microstresses invoked during cooling by the anisotropy of the thermal shrinkage (likely). The absolute  $B_{hkl}^{f'}$  values are significantly larger in the present case than in the study on homogenised  $\varepsilon$ -iron-nitride powders [38]. This difference may be ascribed to a different microstructure and different thermal treatment leading to anisotropic thermal microstrain different in the annealed, homogenised *layer* as compared to the annealed *powder*. In the same sense it can be understood that the refinements described in the following indicate that the *extent* of  $f'$  in the *not-homogenised*  $\varepsilon$  *layer* is somewhat smaller than in the *homogenised*  $\varepsilon$  *layer*, e.g. due to difference in the annealing temperature of the homogenised  $\varepsilon$  layer and the nitriding temperature of the not-homogenised  $\varepsilon$  layers. It was found that adopting values of  $\frac{2}{3}B_{hkl}^{f'}$ , with  $B_{hkl}^{f'}$  as determined from the homogenised  $\varepsilon$  layer, led to consistent interpretation of all diffraction data recorded from the not-homogenised  $\varepsilon$  layers.

Given the contribution  $g \otimes f'$  for each line profile, the total line profile  $h$  can be calculated applying Eq. (3.7) where  $f''$  is calculated according to the microstructural model described in sections 3.3.1 and 3.3.2. The thus obtained profile  $h$  can be fitted to the measured data by determination of optimal values of the fit parameters incorporated in the microstructural model for  $f''$ . These fit parameters are: the strain-free lattice parameters at the grid points  $j$ ,  $a(j)$  and  $c(j)$ , the stress value at the surface of the specimen,  $\sigma_{//}(j=0)$ , the total change in stress over the whole layer,  $\delta\sigma_{//}^{\text{total}}$ . Such fitting was performed for all recorded reflections and all tilt angles  $\psi$  *simultaneously*.

Refinement of  $a(j)$  and  $c(j)$  without any constraints leads to strong correlations of the lattice parameters of neighbouring grid points and to partially physically unreasonable  $a$  and  $c$  depth profiles. The correlations can be reduced, and physically realistic, ‘smoother’  $a(j)$  and  $c(j)$  depth profiles can be obtained, by application of so-called penalty functions ( $PF$ s). Such  $PF$ s serve as contribution to the overall  $\chi_{pen}^2$  (*penalized least squares*) used in the least-squares refinement process, additional to the usual least-squares  $\chi^2$  determined by the difference between the observed and the calculated profiles [39, 40]:

$$\chi_{pen}^2 = \chi^2 + (K \cdot PF)^2, \quad (3.9)$$

where  $K$  denotes a penalty-weighting factor [41].

The  $PF$  applied in this work is the sum of the squared differences between  $\delta a(j)$  and  $\delta a(j + 1)$  and  $\delta c(j)$  and  $\delta c(j + 1)$  for each value of  $j$ :

$$PF = \sum_{j=1}^{n-1} (\delta a(j) - \delta a(j+1))^2 + \sum_{j=1}^{n-1} (\delta c(j) - \delta c(j+1))^2. \quad (3.10)$$

The  $PF$  is minimal ( $PF = 0$ ) for a linear evolution of  $a(j)$  and  $c(j)$  over the whole layer thickness, i.e.  $\delta a(j)$  and  $\delta c(j)$  are constant for all sublayers  $j$ .

A compromise for the weight  $K$  of the penalty-function contribution to the overall  $\chi^2$  has to be found in order to obtain reasonable results: In the case of a too large weight, physical features in  $a(z)$  and  $c(z)$  may be suppressed (‘oversmoothing’) and in the case of a too small weight,  $a(z)$  and  $c(z)$  can vary too unconstrainedly [42]. Consistent and realistic results were obtained by allowing the penalty function to increase the  $\chi^2$  value by not more than about 20 % with respect to the unconstrained refinement.

The least-squares fitting procedures as described above were executed using the programming language available in the launch mode of the TOPAS software [41]. For determination of the optimal values for the fit parameters pertaining to  $f''$  (see above), so-called ‘Pawley fits’ were performed, i.e. allowing free refinement of the total integrated reflection intensity of each reflection  $hkl$  and at each  $\psi$  separately.-

### 3.4 Results and discussion

#### 3.4.1 Microstructure of the $\epsilon$ layers, as determined by optical microscopy, TEM and EBSD

Optical microscopy (Fig. 3.1) and EBSD (Fig. 3.5) revealed that the  $\epsilon$  layers of both samples consist predominantly of columnar grains, i.e. the  $\epsilon$  grains extend from the surface of the specimen to the  $\epsilon/\gamma'$  interface with grain boundaries mostly parallel to the specimen surface normal. The  $\epsilon/\gamma'$  interface shows only slight roughness. Analysis of the EBSD data indicates that there is no distinct orientation relationship between  $\gamma'$  and  $\epsilon$ ; the  $\epsilon$  grains grow largely randomly oriented on top of  $\gamma'$ . EBSD and also the  $\psi$  dependence of the diffracted intensities of the XRD data (not shown in detail here) indicate that the  $\epsilon$  layers investigated exhibit an only weak 001 fibre texture, which is probably a growth texture, because of the absence (see above) of a distinct orientation relationship between the  $\epsilon$  and the  $\gamma'$  grains (also the  $\gamma'$  layer shows no preferred orientation, cf. Ref. [34]).

High-resolution cross-sectional TEM studies at the location of the  $\epsilon/\gamma'$  interface confirm that no specific orientation relationship, as reported in Refs. [30, 43-47], occurs between  $\epsilon$  and  $\gamma'$ . TEM also showed that neither in the  $\epsilon$  layer (Fig. 3.6) nor in the  $\gamma'$  layer at/near the interface stacking faults are present; stacking faults could lead to special line-shift and line-broadening effects in the powder-diffraction patterns.



**Fig. 3.5:** Cross-sectional EBSD image of the compound layer of specimen *A*, showing a columnar grain structure of the  $\epsilon$  layer with grain boundaries more or less perpendicular to the surface. The different grey shades represent different crystal-grain orientations.



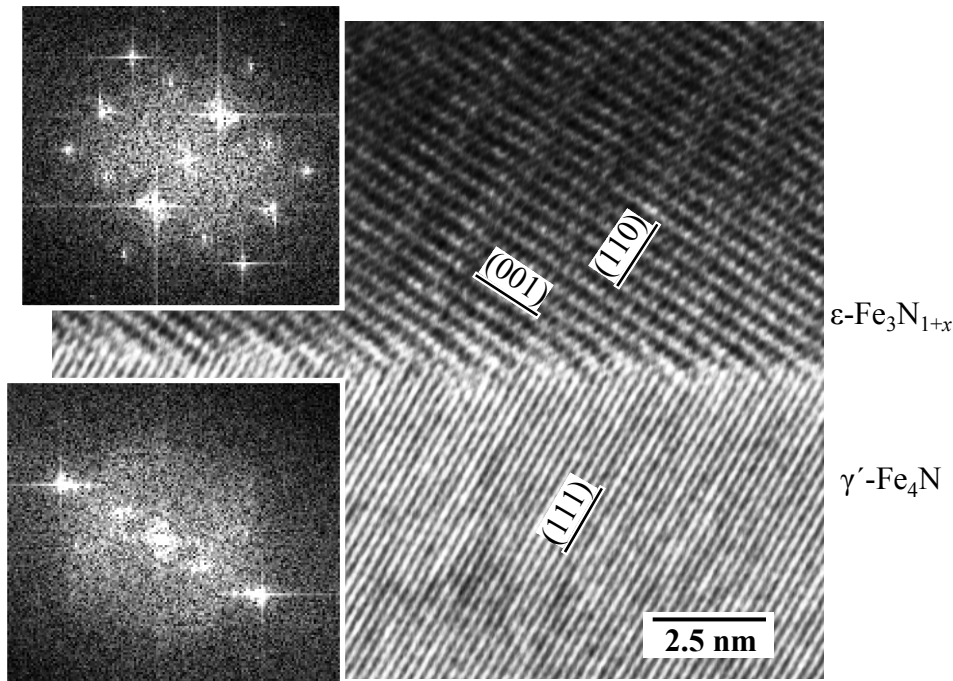


**Fig. 3.6:** Cross-sectional high-resolution TEM image at the  $\epsilon/\gamma'$  interface region of specimen *A*. The insets are Fourier transforms taken from the  $\epsilon$  and  $\gamma'$  parts of the image, corresponding to diffraction patterns, for  $\epsilon$  and  $\gamma'$ . These Fourier transforms indicate a  $[1\bar{1}0]$  zone-axis orientation of the  $\epsilon$  phase. The  $\gamma'$  phase is not oriented along a low-index zone axis (in the image only (111) planes are visible). Evidently, the orientation relationship mentioned in Refs. [30, 43-47] is not observed.

### 3.4.2 Qualitative description of the diffraction-line profile and preliminary analysis

#### (i) Line position and line width

The diffraction patterns recorded for samples *A* and *B* (Fig. 3.7) revealed a characteristic, anisotropic variation of the line positions and line broadening, both as function of the angle of the diffraction vector with the sample normal, corresponding to the tilt angle  $\psi$  (i.e. with respect to the *specimen frame of reference*), as well as function of the angle of the diffraction vector with the  $[001]$  direction of the diffracting crystallites,  $\varphi_{hkl}$  (i.e. with respect to the *crystal frame of reference*; e.g.  $\varphi_{hkl} = 0^\circ$  for  $00l$  reflections and  $\varphi_{hkl} = 90^\circ$  for  $hk0$  reflections).

For both samples, reflections with the diffraction vector direction parallel to the  $[001]$  direction ( $\varphi_{hkl} = 0^\circ$ ), exhibit much smaller line-broadening widths,  $\delta 2\theta_{hkl,\psi}^{\text{total}}$ , than

reflections with the diffraction vector perpendicular to the [001] direction, e.g. 110, 300 ( $\varphi_{hkl} = 90^\circ$ ), which are generally the broadest reflections. In general  $f''$  is much broader than the instrumental broadening  $g$  and the line-broadening contribution  $f'$  originating from a homogenised  $\varepsilon$  layer.

Upon comparing the diffraction patterns of samples  $A$  and  $B$  recorded at a given  $\psi$  and for a given reflection  $hkl$ , the high-angle edge of the reflections, originating from the region at the  $\varepsilon/\gamma'$  interface, appears for both specimens almost at the same  $2\theta$  position, whereas this is not the case for the low-angle edges of the reflections, pertaining to the surface adjacent region: for specimen  $A$  the low-angle side is located at higher  $2\theta$  values than for specimen  $B$ . Furthermore, with increasing  $\psi$  for all  $\varepsilon$  reflections of both specimens the low-angle edge of the reflection shifts towards lower  $2\theta$  values, whereas the shape change at the high-angle edge (see below) does not allow a similar conclusion. The  $\psi$ -dependent shift of in particular the low-angle edge leads to a  $\psi$  dependence of the line broadening: reflections recorded at higher  $\psi$  angles are generally broader than reflections recorded at lower  $\psi$  angles.

The  $\varphi_{hkl}$ -dependent (i.e. with respect to the crystal frame of reference) anisotropic line broadening at a given  $\psi$  can be understood by lattice-parameter variations due to compositional variations [48] associated here with the presence of the nitrogen-concentration gradient within the  $\varepsilon$  layer. Since variation of the nitrogen content leads to larger relative changes of the lattice parameter  $a$  than of the lattice parameter  $c$  [17, 18], reflections with  $\varphi_{hkl}$  close to  $0^\circ$  (see above) should exhibit smaller  $\delta 2\theta_{hkl,\psi}^{\text{total}}$  values than reflections with  $\varphi_{hkl}$  close to  $90^\circ$ , in agreement with the observations described above.

The more pronounced line broadening (valid for all reflections) observed for specimen  $B$ , in comparison with specimen  $A$ , can be explained as follows: Specimen  $B$  was prepared applying a higher nitriding potential than applied for specimen  $A$  (cf. Table 3.1), leading, at the surface of specimen  $B$ , to a higher nitrogen content and consequently to larger lattice spacings at the surface than for specimen  $A$ . At the  $\varepsilon/\gamma'$  interface the nitrogen content and thus the lattice spacings of specimens  $A$  and  $B$  are expected to be similar, supposing local equilibrium of  $\varepsilon$  and  $\gamma'$  at the nitriding temperature. Thus the total change of lattice spacing over the  $\varepsilon$  layer, and thereby the

corresponding total line broadening, is expected to be larger for specimen *B* than for specimen *A*, as observed.

The increase of the line broadening, characterised by the line-width parameter  $\delta 2\theta_{hkl,\psi}^{\text{total}}$ , with increasing  $\psi$  (i.e. with respect to the specimen frame of reference), observed for all reflections of both specimens, can be related to the stress-depth profile within the  $\epsilon$  layers (cf. section 3.4.3.2): With increasing  $\psi$  the low-angle edge of a reflection is shifted to lower  $2\theta$  angles due to tensile stress at the surface, whereas the high-angle edge of the same reflection will remain at the same position  $2\theta$ , if no stress is present in  $\epsilon$  at the  $\epsilon/\gamma'$  interface, or shift to higher angles  $2\theta$ , if compressive stress prevails in  $\epsilon$  at the  $\epsilon/\gamma'$  interface. Then the total width,  $\delta 2\theta_{hkl,\psi}^{\text{total}}$ , increases with increasing  $\psi$ , as observed.

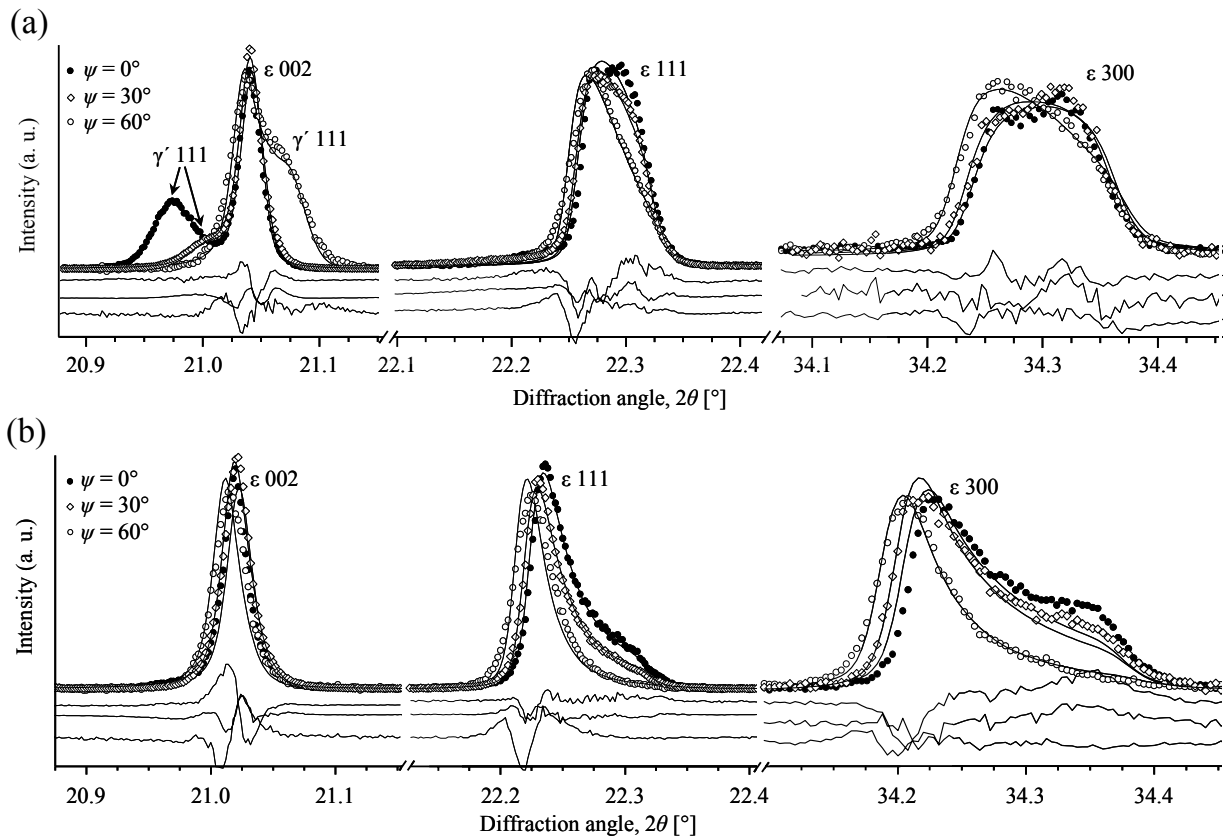


**Fig. 3.7:** Section of the X-ray high-resolution diffraction patterns of (a) specimen *A* and (b) specimen *B* recorded at different tilt angles  $\psi$ . The intensities of the reflections were scaled for better visibility (the original data were considered in the fitting process). The full lines through the measured data points represent the fitted curves obtained on basis of the applied model (the  $\gamma'$ -111 reflection which occurs additionally for specimen *A*, at strongly  $\psi$  dependent  $2\theta$  positions, was fitted separately using a pseudo-Voigt function). The bottom lines represent the difference curves for  $\psi = 0^\circ$  (top),  $\psi = 30^\circ$  (middle) and  $\psi = 60^\circ$  (bottom). The lines were shifted vertically in order to separate them.

## (ii) Line shape

Alongside with the line-width changes due to variations of the diffraction-vector direction with respect to the crystal frame of reference (characterised by the angle  $\varphi_{hkl}$ ) and with respect to the specimen frame of reference (characterised by the angle  $\psi$ ), characteristic changes of the line shape occur. Reflections of specimen *A* with  $\varphi_{hkl}$  close to  $90^\circ$  exhibit a more or less rectangular shape, whereas similar reflections of specimen *B* show characteristic high-angle tails. In general the high-angle part of these reflections, with  $\varphi_{hkl}$  close to  $90^\circ$ , gets attenuated with increasing  $\psi$  with respect to the low-angle part (see Fig. 3.7). Reflections with low  $\varphi_{hkl}$  values are relatively narrow and show no pronounced asymmetry. For some of these reflections (e.g. 002) even slight low-angle tails occur; such tails are also present in the contribution  $f'$  pertaining to homogenised  $\varepsilon$ , emphasising the need of including contribution  $f'$  in the line-broadening analysis (see section 3.3.3). Note that the (apparent) shape of the  $\varepsilon$ -002 reflection of specimen *A* is affected by the 111 reflection of the  $\gamma'$ -Fe<sub>4</sub>N layer underneath this (thin)  $\varepsilon$  layer. The  $\gamma'$ -111 reflection of specimen *A* appears at strongly  $\psi$ -dependent peak positions, due to a relatively large compressive stress within the  $\gamma'$  layer (see Ref. [34]). This 111 reflection of the  $\gamma'$  phase is not visible for specimen *B* because of the larger  $\varepsilon$ -layer thickness of that specimen.

The  $\psi$ -dependent change in peak shape can be ascribed to the absorption of the X-rays. The rectangular shape of almost all reflections of the  $\varepsilon$  layer of specimen *A* (with exception of the narrow reflections with small  $\varphi_{hkl}$  values) measured at  $\psi = 0^\circ$  is due to the low absorption of the X-rays by this relatively thin  $\varepsilon$  layer: a range of more or less equally probable lattice spacings, as pertaining to an almost linear lattice-spacing depth profile, will, in case of negligible absorption of the X-rays, generate such peak shapes. With increasing  $\psi$ , and in particular for the larger  $\varepsilon$ -layer thickness of specimen *B*, the incident and diffracted X-rays in the bottom region of the  $\varepsilon$  layer are significantly absorbed due to, the, for higher  $\psi$  angles and larger  $\varepsilon$ -layer thickness, longer paths the X-rays have to travel through the solid (see also section 3.3.2). Since with increasing distance to the surface the lattice spacings get smaller, the X-ray attenuation affects, in particular, the high-angle sides of the reflections causing the

characteristic high-angle tails, especially pronouncedly visible for specimen *B* (Fig. 3.7b). This effect is less distinctly visible for relatively narrow reflections.

### 3.4.3 Results of the fitting and discussion

By the fitting, simultaneously to all observed diffraction patterns recorded at various values of  $\psi$  using the model and the procedure described in section 3.3, the observed reflection profiles can be reproduced well. Slight discrepancies occur for the peak positions and peak shifts of especially reflections with  $\varphi_{hkl}$  close to  $0^\circ$ , measured at different values of  $\psi$ . This may be an artefact due to the adopted isotropy of the elastic constants. Non-ideal  $\epsilon$ -Fe<sub>3</sub>N<sub>1+x</sub> (deviating from the ideal composition Fe<sub>3</sub>N and/or deviating from the ideally ordered nitrogen distribution) may be more pronouncedly elastically anisotropic than predicted by the applied first-principles calculations for ideal Fe<sub>3</sub>N. Further, for the peak profiles of specimen *B* the high-angle tails of high- $\varphi_{hkl}$  reflections at low  $\psi$  could not be described fully adequately. It can be said that the *simultaneous* fitting procedure applied to all measured reflections for different values of  $\psi$ , using the partitioned lattice-parameter profiles and the linear stress-depth profile as microstructure model, led to a satisfactory description of the measured data. In the following, the obtained results for the fit parameters are presented and discussed.

#### 3.4.3.1 Lattice-parameter-depth profiles

Indeed, as expected for nitrogen diffusion-controlled growth of the  $\epsilon$  layer, the values of the strain-free lattice parameters  $a$  and  $c$  and thus the nitrogen content decrease from the surface to the  $\epsilon/\gamma'$  interface (Fig. 3.8). If the nitrogen concentration depends linearly on depth in the  $\epsilon$  layers during nitriding [12, 49], application of one-to-one relations between composition and the two hexagonal lattice parameters (e.g. [17, 18]) involves that the lattice parameters  $a(z)$  and  $c(z)$  should also vary linearly with depth. Since the expected compositions of the  $\epsilon$  layers at the surface and at the  $\epsilon/\gamma'$  interface can be calculated on the basis of nitrogen-absorption isotherms and (local) equilibrium at the  $\epsilon/\gamma'$  interface [12, 22] (see Table 3.1), a linear lattice-parameter-depth profile can then be predicted. Such a prediction is not supported by the results obtained here (see Fig. 3.8). In particular, the depth-dependent lattice parameters obtained by the model fitting do not depend linearly on depth for both specimen *A* and specimen *B*.

Moreover, both lattice parameters,  $a$  and  $c$ , do not vary in a coupled fashion as it would be expected from the composition dependence of the hexagonal lattice parameters: the relative change of  $a$  ( $\delta a^{\text{total}} / a(j=0)$ ) should be 1.8 times larger than the relative change of  $c$  (cf. data in Ref. [18]), but experimentally this relative change is 3.4 for specimen  $A$  and 2.5 for specimen  $B$ <sup>3.6</sup>.

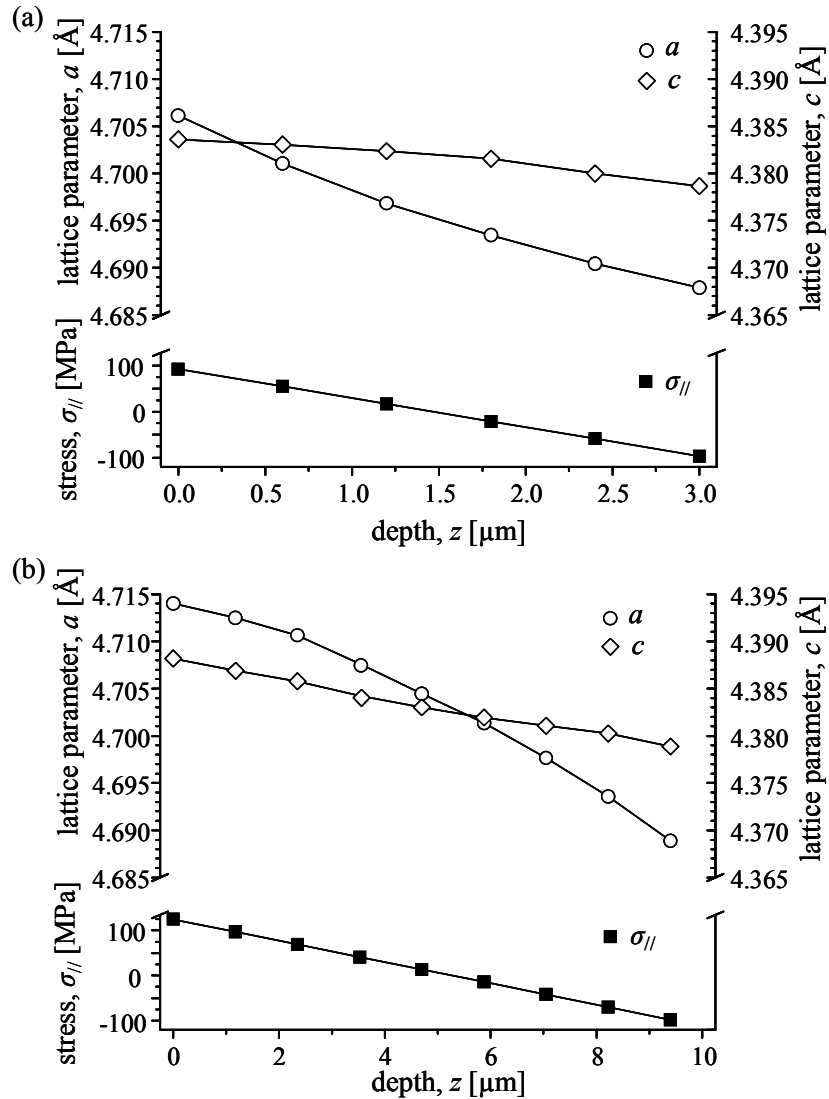


**Fig. 3 8:** Strain-free lattice-parameter and stress-depth profiles of the  $\epsilon$  layer of (a) specimen  $A$  and of (b) specimen  $B$  as determined by fitting on the basis of all recorded diffraction patterns. The values of both lattice parameters,  $a$  and  $c$ , decrease with increasing distance to the surface. The total changes of  $\delta a$  and  $\delta c$  are larger for specimen  $B$  than for specimen  $A$ , which is compatible with the applied nitriding conditions (Table 3.1). The stress is for both specimens of tensile nature at the surface, decreases with increasing depth and becomes of compressive nature near the  $\epsilon/\gamma'$  interface.

<sup>3.6</sup> If one would have imposed in the fitting procedure the one-to-one relations between composition and the lattice parameters from [17, 18], an unacceptable description of the experimental data would occur.

The strain-free lattice-parameter data obtained have also been presented in plots of  $c$  vs.  $a$  (Fig. 3.9). In this type of plot the effect of composition is only indirectly revealed by the decrease of both lattice parameters with decreasing nitrogen content. If  $a$  and  $c$  would only depend on the nitrogen content prevailing at the depth  $z$ , all data points should be located on a curve  $c = f(a)$ . This curve can be calculated by the dependencies of the lattice parameters  $a$  and  $c$  on composition; two examples for (linear)  $c = f(a)$  interdependences valid for quenched  $\varepsilon$  phase have been included in Fig. 3.9 [17, 18]. Evidently, this does not hold fully for the experimental data: *at the surface* of both specimens  $A$  and  $B$  the lattice parameters are compatible with the (for quenched  $\varepsilon$  phase) predicted interdependences  $c = f(a)$  (sample  $A$ :  $a$ ,  $c$  of the first grid point; sample  $B$ :  $a$ ,  $c$  of the first 5 grid points), whereas systematic deviations from that interdependence occur with increasing depth  $z$ : for a given value of  $a$  at a certain depth  $z$  the value of  $c$  at the same depth is larger than predicted by the interdependences  $c = f(a)$ . This anomaly appears to be typical for polycrystalline  $\varepsilon$  layers, since too large  $c/a$  ratios were not only observed in the present work but were also reported by Liapina *et al.* [24], who analysed (homogenised)  $\varepsilon$  layers of various nitrogen contents with conventional XRD measurements using  $\text{CoK}\alpha_1$ , thereby obtaining data pertaining to averages for the whole  $\varepsilon$  layer.

As a possible explanation of the observed deviations from the interdependences  $c = f(a)$  as given by [17, 18], it may be suggested that stress in the  $\varepsilon$  layer (section 3.4.3.2) may influence the state of nitrogen ordering in the  $\varepsilon$  phase (and possibly its magnetism), which can influence the lattice parameters [18]. However, the most likely explanation for the too large  $c/a$  ratio close to the  $\varepsilon/\gamma'$  interface is suggested to be the anisotropy of the linear thermal expansion coefficient of  $\varepsilon$ - $\text{Fe}_3\text{N}_{1+x}$  [9, 50], which is also likely the origin of the line broadening contribution  $f'$  (see section 3.3.3): The linear coefficient of thermal expansion  $\alpha_{\varepsilon,c}$  of the lattice parameter  $c$ , measured for powders, is much larger (up to about three times, depending on the nitrogen content) than that of the lattice parameter  $a$ ,  $\alpha_{\varepsilon,a}$ . Such anisotropy leads to strongly direction dependent dimensional changes upon changing temperature. In massive polycrystalline layers, with intrinsically strong grain interaction, the effective lattice-parameter changes due to thermal shrinkage upon cooling will be less anisotropic than

as expected for free standing grains, or possible in powder specimens. Hence, upon cooling the thermal shrinkage in polycrystalline  $\varepsilon$  layers in  $c$  directions is less pronounced and in  $a$  directions more pronounced than strived for; even a close-to-isotropic shrinkage may occur (see also discussion on the macrostress in section 3.4.3.2). This effect of grain interaction leads to larger values of the lattice parameter  $c$  and to smaller values of the lattice parameter  $a$  measured at room temperature, compared to values expected for unconstrained crystallites. Therefore, a too large  $c/a$  lattice-parameter ratio is observed, especially close to the  $\varepsilon/\gamma'$  interface; at the surface grain interaction is less constrained, and therefore the lattice parameters at the surface can be compatible with the concentration dependencies of the lattice parameters corresponding to  $c = f(a)$ , as observed (see Fig. 3.9). Similar changes of measured lattice parameters due to anisotropic expansion/shrinkage in combination with grain-interaction effects have been observed for thin layers of NiSi [51].

The lattice parameters at the surface and at the  $\varepsilon/\gamma'$  interface as expected from the nitriding conditions (cf. begin of section 3.4.3.1) have been indicated in Fig. 3.9, too. For both specimens the fitted lattice parameters at the surface as well as at the  $\varepsilon/\gamma'$  interface are larger than the expected values. This might hint at nitrogen contents at the surface and at the  $\varepsilon/\gamma'$  interface larger than expected. To appreciate these differences it is recognised that uncertainties exist for the expected nitrogen contents: for example the phase boundary  $\varepsilon/\varepsilon+\gamma'$  (at 823 K) may be located at 24.1 at.% N [12] or at 24.5 at.% N [52], leading to quite large variations in the corresponding lattice parameters.



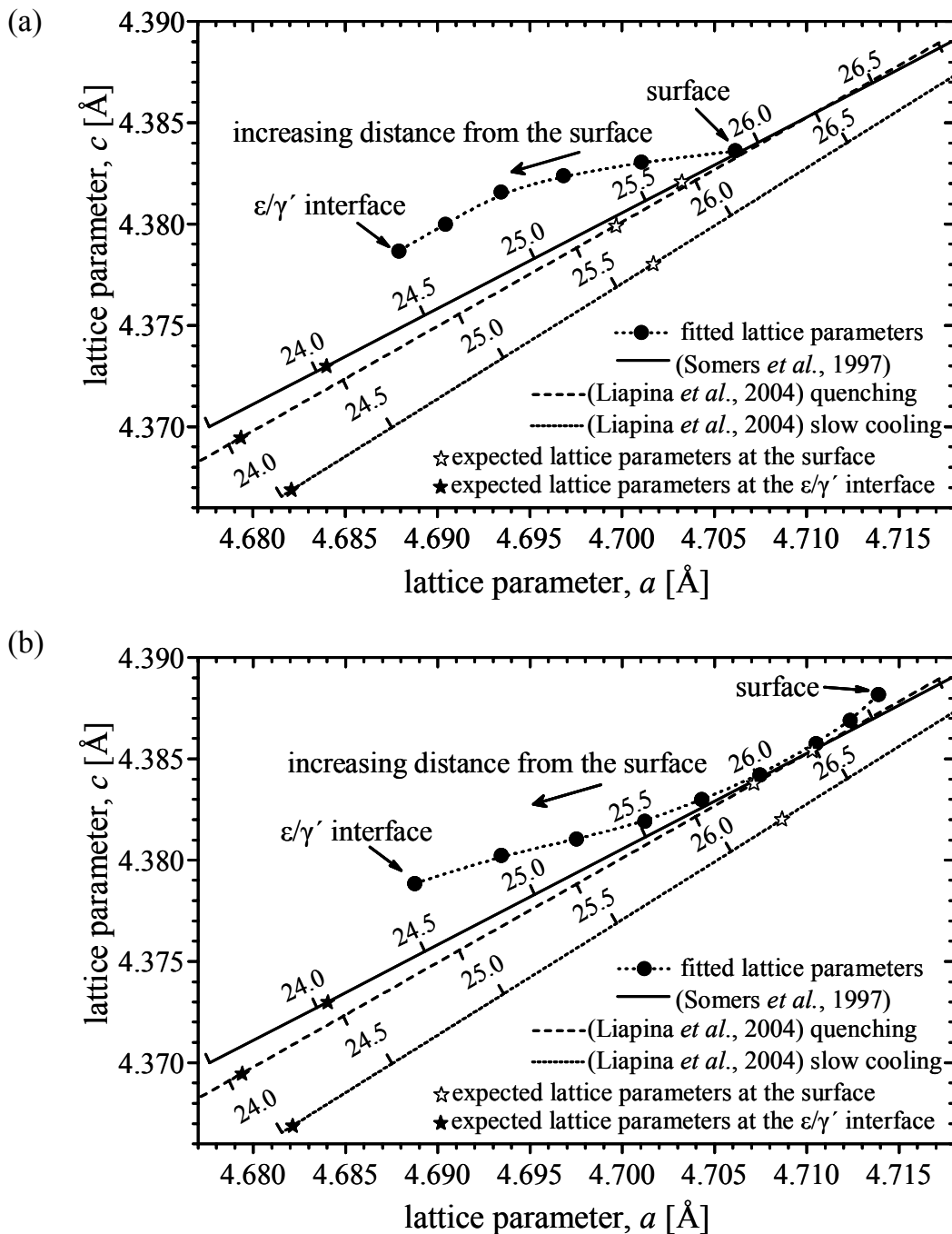


**Fig. 3.9:** Lattice parameter  $c$  vs. lattice parameter  $a$  of (a) specimen A and (b) specimen B. At the surface the lattice parameters are in good agreement with interdependences  $c = f(a)$  proposed by Refs. [17] and [18] for quenched  $\epsilon$  phase. Approaching the  $\epsilon/\gamma'$  interface the  $c/a$  ratio increases with respect to these relations. The open stars indicate the expected lattice parameters at the surface ( $\epsilon$  in equilibrium with the gas phase at 823 K) and the filled stars indicate the expected lattice parameters at the  $\epsilon/\gamma'$  interface ( $\epsilon$  in equilibrium with  $\gamma'$  at 823 K).

### 3.4.3.2 Residual stress-depth profiles

The residual macrostress-depth profiles within the  $\varepsilon$  layers of both specimens, as determined by the fitting according to Eq. (3.2), are similar (Fig. 3.8). The stress at the surface is tensile, decreases with increasing depth, passing through zero near to the middle of the layers, and becomes compressive close to and at the  $\varepsilon/\gamma'$  interface. The obtained stress value at the surface of specimen *A* (about + 90 MPa) is lower than that of specimen *B* (about + 125 MPa); at the  $\varepsilon/\gamma'$  interface the stress amounts for both specimens to about – 95 MPa. Consequently, the total *change* in stress over the whole  $\varepsilon$  layer is  $\delta\sigma_{//}^{\text{total}} = -185$  MPa for specimen *A* and  $\delta\sigma_{//}^{\text{total}} = -220$  MPa for specimen *B*, which corresponds to total *changes* in strain of  $\delta\varepsilon_{//}^{\text{total}} = -5.3 \times 10^{-4}$  for specimen *A* and of  $\delta\varepsilon_{//}^{\text{total}} = -6.4 \times 10^{-4}$  for specimen *B*, according to  $\delta\varepsilon_{//}^{\text{total}} = \frac{\delta\sigma_{//}^{\text{total}}(1-\nu)}{E}$ .

The compound layer is attached by cohesion to the ferritic substrate, the latter being much thicker than the compound layer. Thus, the ferrite substrate will be largely stress/strain free, and the linear misfit between the layer and the substrate is accommodated by a (biaxial) state of macrostrain/macrostress in the compound layer. On this basis different sources for the origin of the residual macrostress in the  $\varepsilon$  layers can be discussed.

#### (i) Thermal misfit

The observed stress in the  $\varepsilon$  layer, and in particular the observed total *change* in stress  $\delta\sigma_{//}^{\text{total}}$ , can be ascribed to thermally induced misfit between the layer and the substrate, as generated by quenching the specimen from the nitriding temperature to ambient temperature (see what follows).

Thermal misfit between the layer and the substrate originates from different coefficients of linear thermal expansion of the  $\varepsilon$  phase (averaged over the crystallographic orientations, viz. isotropy of thermal expansion is assumed here) and of the  $\alpha$ -Fe substrate. Thus, the associated thermal strain in the  $\varepsilon$  layer parallel to the surface,  $\varepsilon_{//}^{\text{th}}$ , can be calculated from

$$\varepsilon_{//}^{\text{th}} = \int_{T_1}^{T_2} (\alpha_{\varepsilon}(z) - \alpha_{\alpha\text{-Fe}}) dT, \quad (3.11)$$

where  $T_1$  and  $T_2$  denote nitriding and ambient temperature, respectively. The average coefficient of linear thermal expansion  $\alpha_\varepsilon$  of  $\varepsilon$ -Fe<sub>3</sub>N<sub>1+x</sub> was found to increase with increasing nitrogen content [50, 53] (The increase of (average)  $\alpha_\varepsilon$  with the nitrogen content (see Fig. 3.10) appears to be an acceptable trend as it is also exhibited by  $\varepsilon$ -phase analogous manganese nitrides [53]). Hence, the presence of a stress gradient in the  $\varepsilon$  layer can be understood, with the stress becoming (more) compressive for increasing depth below the surface.

A quantitative calculation of the *change* of the thermal misfit strain over the  $\varepsilon$  layer,  $\delta\varepsilon_{//}^{\text{th, total}}$ , is possible using

$$\delta\varepsilon_{//}^{\text{th, total}} = \varepsilon_{//}^{\text{th}}(z=0) - \varepsilon_{//}^{\text{th}}(z=Z) = [\alpha_\varepsilon(z=0) - \alpha_\varepsilon(z=Z)][T_2 - T_1] \quad (3.12)$$

yielding<sup>3.7</sup>  $\delta\varepsilon_{//}^{\text{th, total}} = -1.3 \times 10^{-3}$  for specimen *A* and  $\delta\varepsilon_{//}^{\text{th, total}} = -1.7 \times 10^{-3}$  for specimen *B*,

corresponding to total *changes* in stress over the  $\varepsilon$  layer, given by  $\delta\sigma_{//}^{\text{th, total}} = \frac{\delta\varepsilon_{//}^{\text{th, total}} \times E}{(1-\nu)}$ ,

of  $\delta\sigma_{//}^{\text{th, total}} = -460$  MPa for specimen *A* and of  $\delta\sigma_{//}^{\text{th, total}} = -580$  MPa for specimen *B*.

The larger value of  $\delta\varepsilon_{//}^{\text{th, total}} / \delta\sigma_{//}^{\text{th, total}}$  for specimen *B*, as compared to specimen *A*, is consistent with the larger compositional variation present in specimen *B* corresponding with a larger change in  $\alpha_\varepsilon$ . However, the calculated stress changes are about 2.5 times larger than the measured stress changes. Moreover, the prediction on the basis of the data for the linear thermal expansion coefficient in Fig. 3.10 involves that at the surface still a compressive stress should prevail. This can be discussed as follows.

---

<sup>3.7</sup> The isotropic coefficient of thermal expansion  $\alpha_\varepsilon$  was assumed to vary linearly with concentration and the values used for  $\alpha_\varepsilon$  at the surface and at the  $\varepsilon/\gamma'$ -interface were obtained by inter- and extrapolation, respectively, at nitrogen content values pertaining to the surface and the  $\varepsilon/\gamma'$  interface (see Table 3.1).

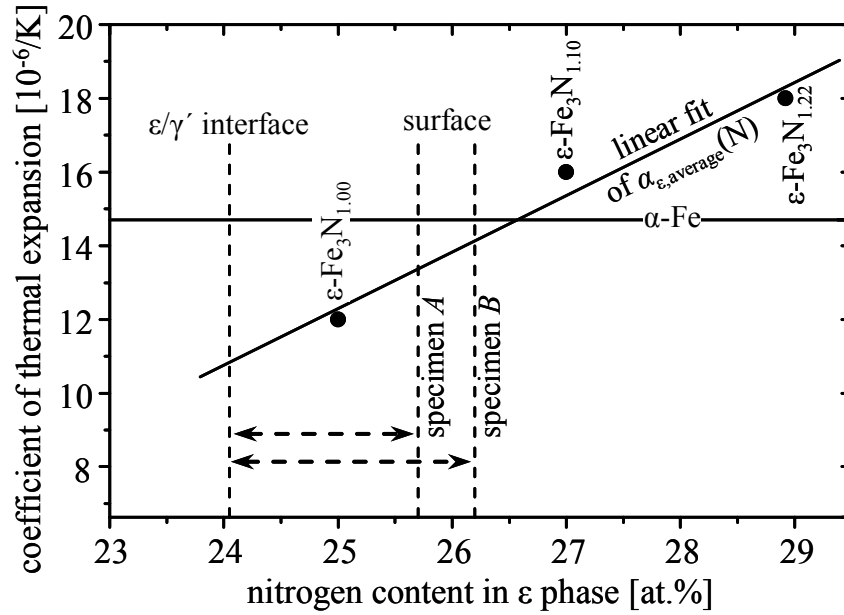


**Fig. 3.10:** The concentration dependence of the coefficient of thermal expansion of the  $\epsilon$  phase (isotropic average),  $\alpha_\epsilon$  [53], including a fitted straight line. With increasing nitrogen content  $\alpha_\epsilon$  increases: at low nitrogen contents  $\alpha_\epsilon$  is smaller than  $\alpha_{\alpha\text{-Fe}}$ , whereas at higher nitrogen contents  $\alpha_\epsilon$  is larger than  $\alpha_{\alpha\text{-Fe}}$ . The value for  $\alpha_{\alpha\text{-Fe}} = 1.47 \times 10^{-6} \text{ K}^{-1}$  was obtained by integration over the temperature interval from 293 K to 823 K [54] and holds only for pure iron.

Already small inaccuracies of the adopted values for the thermal expansion coefficients can explain the discrepancy: For example, see the various values for  $\alpha_{\alpha\text{-Fe}}$  compiled in literature [19, 21, 54] vary, and, in particular, the values of  $\alpha_\epsilon$  are likely of limited accuracy, because these values were determined from temperature-dependent lattice-parameter data ranging from ambient temperature to at maximum 713 K, whereas the nitriding temperature in this work was 823 K. The use of an isotropic average of the (intrinsically anisotropic; see section 3.4.3.1) coefficient of linear thermal expansion of the  $\epsilon$  phase may also induce errors. Since the macrostrain/macrostress present in the  $\epsilon$  phase at a certain depth is determined by the *difference* of the thermal expansion coefficients of the  $\epsilon$  layer and the  $\alpha\text{-Fe}$  substrate (see Eq. (3.11)), small inaccuracies of both adopted expansion coefficients will already significantly affect the calculated depth-dependent values of the strain/stress. Further, differences between the observed and calculated strain values may also be due to macrostrain relaxation within the first 50 K to 100 K during cooling [1].

The difference between the observed stress/strain and the predicted thermally induced stress/strain discussed above may be (partially) due to the presence of additional contributions discussed under points (ii)-(iv).

### (ii) Compositionally induced strain

It can be assumed that the specific volume (i.e. volume per Fe atom) increase upon transformation of  $\gamma'$  into  $\varepsilon$  at the  $\varepsilon/\gamma'$  is accommodated plastically (see (iii) below). Then, during compound-layer growth elastic accommodation of the specific volume increase within the  $\varepsilon$  layer due to the increase of the nitrogen content from the  $\varepsilon/\gamma'$  interface to the surface will lead to a (with respect to the thermal stress) additional depth-dependent stress contribution. This contribution counteracts the thermally induced stress-depth profile, as can be understood as follows: At the  $\varepsilon/\gamma'$  interface the volume of the unstrained  $\varepsilon$  unit cell is smaller than at the surface. Hence, for the same amount of iron atoms per unit area parallel to the surface, a compressive stress parallel to the surface develops that becomes larger with decreasing distance to the surface. The largest value of compositionally induced strain,  $\varepsilon_{//}^c$ , occurs at the surface and equals

$$\varepsilon_{//}^c = (V_{\varepsilon/\gamma'\text{-interface}} - V_{\text{surface}}) / V_{\text{surface}} \times 1/3, \quad (3.13)$$

where  $V_{\varepsilon/\gamma'\text{-interface}}$  and  $V_{\text{surface}}$  are the volumes of the  $\varepsilon$  unit cell at the  $\varepsilon/\gamma'$  interface and at the surface, respectively. Using values for the lattice parameters at the surface and at the  $\varepsilon/\gamma'$  interface as obtained by the fitting procedure, the compositionally induced strain at the surface amounts for specimen *A* to  $\varepsilon_{//}^c = -3.0 \times 10^{-3}$  and for specimen *B* to  $\varepsilon_{//}^c = -4.3 \times 10^{-3}$ . These strain values are relatively large and it may be expected that the compositional misfit within the  $\varepsilon$  layer is accommodated to a significant extent plastically (cf. [1, 21]). In any case this possible source of residual stress cannot explain the occurrence of tensile stress at the surface.

### (iii) Volume misfit

During growth of the compound layer volume misfits due to the different specific volumes per solvent (= iron) atom of  $\alpha$ -Fe,  $\gamma'$ -Fe<sub>4</sub>N<sub>1-y</sub> and  $\varepsilon$ -Fe<sub>3</sub>N<sub>1+x</sub> occur at the  $\gamma'/\alpha$

and  $\varepsilon/\gamma'$  interfaces: The specific volume of  $\gamma'$  at the  $\gamma'/\alpha$  interface is about 15.0 % larger than that of  $\alpha$ -Fe and the specific volume of  $\varepsilon$  at the  $\varepsilon/\gamma'$  interface is about 16.7 % larger than that of  $\alpha$ -Fe (i.e. 1.4 % larger than the specific volume of  $\gamma'$  at the  $\varepsilon/\gamma'$  interface). Taking the very thick, with respect to the compound layer,  $\alpha$ -Fe substrate as completely rigid, and if these misfits would be accommodated fully elastically, compressive stresses in both sublayers,  $\gamma'$  and  $\varepsilon$ , would be induced during growth of these phases. However, the results by Somers and Mittemeijer, 1990 [1] indicate that for  $\gamma'$  this volume misfit is accommodated fully plastically and this misfit does not contribute to the residual stress as observed after nitriding at ambient temperature. Recognising fully plastic accommodation of the volume misfit at the  $\gamma'/\alpha$  interface, a possible elastic accommodation of the  $\varepsilon/\gamma'$  interfacial volume misfit would lead to a strain of  $\varepsilon_{||}^{\text{vol}} = -4.7 \times 10^{-3}$  in the  $\varepsilon$  layer. This value is much larger than the value found at the  $\varepsilon/\gamma'$  interface. Therefore it may be assumed that the volume misfit strain occurring upon the  $\gamma'$  to  $\varepsilon$  transformation is also accommodated plastically and thus does not contribute to the observed stress at the  $\varepsilon/\gamma'$  interface.

#### (iv) Strain relaxation due to pore formation

Porosity in the surface-adjacent region of the  $\varepsilon$  layer can lead to the reduction of stress as compared to a massive layer. The formation of porosity in iron nitrides is very common [55, 56] and can be attributed to the metastable nature of the iron nitrides with respect to the decomposition into iron and molecular nitrogen gas at normal pressure [12, 47, 56]. Pores form mainly upon longer treatment times and for higher nitrogen contents. Thus it can be understood that pore formation had occurred only very *slightly* in the near-surface region of specimen *B* and not for specimen *A* (cf. Fig. 3.1). Hence, the effect of strain relaxation due to porosity can be neglected for the presently studied specimens.

Somers and Mittemeijer, 1992 [21] discussed, mainly theoretically, stress-depth profiles within  $\varepsilon$ -Fe<sub>3</sub>N<sub>1-x</sub> layers on the basis of several different contributions. In that work also a stress gradient was found experimentally (by XRD measurements) by successive sublayer removals, which is generally in agreement with the present study:

the stress was found to be zero at the surface and becoming compressive with increasing distance to the surface. The presence of the stress gradient was explained, contrary to the present interpretation, to be caused by (in that case distinct) porosity at the surface (stress relaxation) and due to elastic accommodation of the volume misfit between  $\epsilon$  and  $\gamma'$  during growth. The effect of the thermal misfit could not be estimated since no precise data for thermal expansion of  $\epsilon$  were known (it was assumed  $\alpha_{\gamma'} < \alpha_{\epsilon} < \alpha_{\alpha\text{-Fe}}$ ). In other works [19, 20] tensile stresses were found in the near-surface region of  $\epsilon$ -Fe<sub>3</sub>(N,C)<sub>1+x</sub> layers, which is compatible with the present results. However, the analysed compound layers were grown on steel substrates and partially also generated by nitrocarburising processes and then consequently carbon was taken up in the compound layers, further complicating the problem and therefore no straightforward interpretation was possible.

### 3.5 Conclusions

A consistent interpretation of both the diffraction-line shift and the anisotropic diffraction-line broadening, with respect to both the crystal frame of reference and the specimen frame of reference, is possible for hexagonal  $\epsilon$ -Fe<sub>3</sub>N<sub>1+x</sub> layers using a model for the microstructure comprising the simultaneous presence of composition- and stress-depth profiles. Depth-dependent strain-free lattice parameters and stress values can be determined by fitting of the model to the full profiles of several reflections  $hkl$  recorded at different specimen-tilt angles.

Application of this model to high-resolution X-ray powder diffraction patterns recorded at various specimen-tilt angles, using synchrotron radiation, from two different polycrystalline  $\epsilon$ -Fe<sub>3</sub>N<sub>1+x</sub> layers grown on  $\alpha$ -Fe by gas nitriding at 823 K revealed that:

(i) The macrostrain-free lattice-parameter-depth profiles in the  $\epsilon$  layers are caused by the depth dependence of the nitrogen contents within the layers with high nitrogen contents at the surface and low nitrogen contents at the  $\epsilon/\gamma'$  interface. The observed line broadening is mainly due to this compositional variation, which corresponds to the different nitriding conditions of the two analysed specimens. The values of the strain-

free lattice parameters  $a$  and  $c$  decrease from the surface to the  $\varepsilon/\gamma'$  interface. Away from the surface of the  $\varepsilon$  layer, grain interaction counteracting the crystallographically anisotropic thermal shrinkage of the  $\varepsilon$  phase leads to too large  $c/a$  lattice-parameter ratios as observed at room temperature.

(ii) The macrostress-depth profiles in the  $\varepsilon$  layers are induced by cooling the  $\varepsilon$  layer after nitriding to room temperature. The concentration dependence of the average coefficient of thermal expansion of  $\varepsilon\text{-Fe}_3\text{N}_{1+x}$  leads to tensile stress at the surface and to compressive stress at the  $\varepsilon/\gamma'$  interface, since the coefficient of thermal expansion of  $\varepsilon\text{-Fe}_3\text{N}_{1+x}$  is larger than that of  $\alpha\text{-Fe}$  for high nitrogen content and smaller than that of  $\alpha\text{-Fe}$  for low nitrogen content.



## Appendix

### First-principles calculations of the elastic constants of $\epsilon$ -Fe<sub>3</sub>N

First-principles calculations of the five independent elastic constants (at 0 K) for hexagonal  $\epsilon$ -Fe<sub>3</sub>N were performed employing the *Vienna ab initio simulation package* VASP [57, 58] in a similar fashion as described for  $\gamma'$ -Fe<sub>4</sub>N [34]. The obtained elastic stiffness constants  $C_{ij}$  of  $\epsilon$ -Fe<sub>3</sub>N are  $C_{11} = 313.72$  GPa,  $C_{12} = 141.82$  GPa,  $C_{13} = 131.50$  GPa,  $C_{33} = 329.17$  GPa and  $C_{44} = 105.65$  GPa. The small differences between  $C_{11}$  and  $C_{33}$ ,  $C_{12}$  and  $C_{13}$  as well as of  $(C_{11} - C_{12})/2$  and  $C_{44}$  indicate a relatively small elastic anisotropy. Therefore, isotropically averaged elastic constants were calculated out of the anisotropic constants, leading to:  $C_{11} = C_{33} = 321.46$  GPa,  $C_{12} = C_{13} = 133.65$  GPa,  $C_{44} = (C_{11} - C_{12})/2 = 93.90$  GPa. Thus it can be calculated (cf. [36]): Young's modulus  $E = 243$  GPa and Poisson's ratio  $\nu = 0.29$ . These last, isotropic values were used in this work.

### Acknowledgement

The authors are grateful to Mr. Jürgen Köhler for his help with the nitriding experiments and to Dr. Ewald Bischoff for performing the EBSD measurements. We also wish to thank Mr. Peter Kobold and Dr. Peter van Aken for TEM analysis. Special thanks go to Dr. Shunli Shang (Pennsylvania State University, Pennsylvania, USA) for calculating the elastic constants of  $\epsilon$ -Fe<sub>3</sub>N and to Dr. Michael Knapp (CELLS, Barcelona, Spain), who assisted during the measurements at the beamline B2, DESY, Hasylab (Hamburg, Germany).

## References

- [1] Somers MAJ, Mittemeijer EJ. *Metall Trans A* 1990;21A:189.
- [2] Liedtke D, Baudis U, Boßlet J, Huchel U, Klümper-Westkamp H, Lerche W, Spies H-J. *Wärmebehandlung von Eisenwerkstoffen*. Renningen: Expert Verlag, 2006.
- [3] Knerr CH, Rose TC, Filkowski JH. In: *ASM Handbook Heat Treating Vol 4*, Eds.: Davis, JR, Davidson, GM, Lampman, SR, Zorc, TB, Daquila, JL, Ronke, AW, Henniger, KL, Uhl, RC, ASM International, 1991, p. 387.
- [4] Bell T. *Heat Treat Met* 1975;2:39.
- [5] Dawes C, Tranter DF. *Heat Treat Met* 1985;3:70.
- [6] Jack KH. *Proc R Soc London, A* 1948;195:34.
- [7] Jack KH. *Acta Crystallogr* 1952;5:404.
- [8] Leineweber A, Jacobs H, Hüning F, Lueken H, Schilder H, Kockelmann W. *J Alloys Compd* 1999;288:79.
- [9] Leineweber A, Jacobs H, Hüning F, Lueken H, Kockelmann W. *J Alloys Compd* 2001;316:21.
- [10] Kooi BJ, Somers MAJ, Mittemeijer EJ. *Metall Mater Trans A* 1996;27A:1055.
- [11] Wriedt HA, Gokcen NA, Nafziger RH. *Bull Alloy Phase Diagr* 1987;8:355.
- [12] Mittemeijer EJ, Somers MAJ. *Surf Eng* 1997;13:483.
- [13] Burdese A. *Metall Ital* 1957;49:195.
- [14] Bouchard RJ, Frederick CG, Johnson V. *J Appl Phys* 1974;45:4067.
- [15] Firrao D, De Benedetti B, Rosso M. *Metall Ital* 1979;9:373.
- [16] Jentsch W-D, Böhmer S. *Krist Tech* 1977;12:1275.
- [17] Somers MAJ, Kooi BJ, Maldzinski L, Mittemeijer EJ, van der Horst AA, van der Kraan AM, van der Pers NM. *Acta Mater* 1997;45:2013.
- [18] Liapina T, Leineweber A, Mittemeijer EJ, Kockelmann W. *Acta Mater* 2004;52:173.
- [19] Oettel H, Ehrentraut B. *Härterei-Tech Mitt* 1985;40:183.
- [20] Rozendaal HCF, Colijn PF, Mittemeijer EJ. *Surf Eng* 1985;1:30.
- [21] Somers MAJ, Mittemeijer EJ. *Härterei-Tech Mitt* 1992;47:175.

- [22] Maldzinski L, Przylecki Z, Kunze J. *Steel Res* 1986;57:645.
- [23] Mittemeijer EJ, Slycke JT. *Surf Eng* 1996;12:152.
- [24] Liapina T, Leineweber A, Mittemeijer EJ. *Metall Mater Trans A* 2006;37A:319.
- [25] Liapina T, Leineweber A, Mittemeijer EJ. *Scripta Mater* 2003;48:1643.
- [26] Chatterjee-Fischer R, Bodenhausen R, Eysell F-W, Hoffmann R, Liedke D, Mallener H, Rembges W, Schreiner A, Welker G. *Wärmebehandlung von Eisen und Stahl - Nitrieren und Nitrocarburieren*. Renningen-Malmsheim: Expert Verlag, 1995.
- [27] Colijn PF, Mittemeijer EJ, Rozendaal HCF. *Z Metallkde* 1983;74:620.
- [28] Wells A. *J Mater Sci* 1985;20:2439.
- [29] Strecker A, Salzberger U, Mayer J. *Prakt Metallogr* 1993;30:482.
- [30] Middendorf C, Mader W. *Z Anorg Allg Chem* 2001;627:398.
- [31] Knapp M, Baetz C, Ehrenberg H, Fuess H. *J Synchr Rad* 2004;11:328.
- [32] Welzel U, Ligot J, Lamparter P, Vermeulen AC, Mittemeijer EJ. *J Appl Crystallogr* 2005;38:1.
- [33] Delhez R, de Keijser TH, Mittemeijer EJ. *Surf Eng* 1987;3:331.
- [34] Gressmann T, Wohlschlägel M, Shang S, Welzel U, Leineweber A, Mittemeijer EJ, Liu Z-K. *Acta Mater* 2007;55:5833.
- [35] Evenschor PD, Fröhlich W, Hauk V. *Z Metallkde* 1971;62:38.
- [36] Howard CJ, Kisi EH. *J Appl Crystallogr* 1999;32:624.
- [37] NIST. X-ray attenuation tables:  
<http://physics.nist.gov/PhysRefData/FFast/html/form.html>. 2006.
- [38] Liapina T, Leineweber A, Mittemeijer EJ, Knapp M, Baetz C, Liu ZQ, Mitsuishi K, Furuya K. *Z Kristallogr Suppl* 2006;23:449.
- [39] Coelho AA. *J Appl Crystallogr* 2000;33:899.
- [40] Berger TG, Leineweber A, Mittemeijer EJ, Knapp M. *Z Kristallogr Suppl* 2006;23:443.
- [41] Coelho AA. *TOPAS: General Profile and Structure Analysis Software for Powder Diffraction Data*. Karlsruhe, Germany: Bruker AXS GmbH, 2003.
- [42] Louboutin R, Louër D. *Acta Cryst A* 1969;25:335.
- [43] Gerardin D, Morniroli JP, Michel H, Gantois M. *J Mater Sci* 1981;16:159.

- [44] Schubert T, Oettel H, Bergner D. Härtereit-Tech Mitt 1986;41:370.
- [45] Xu X, Wang L, Yu Z, Hei Z. Metall Mater Trans A 1996;27A:1347.
- [46] Liu ZQ, Hei ZK, Li DX. J Mater Res 2002;17:2621.
- [47] Middendorf C, Mader W. Z Metallkde 2003;94:333.
- [48] Leineweber A, Mittemeijer EJ. J Appl Crystallogr 2004;37:123.
- [49] Somers MAJ, Mittemeijer EJ. Metall Mater Trans A 1995;26A:57.
- [50] Leineweber A. Ordnungsverhalten von Stickstoff sowie Magnetismus in binären Nitriden einiger 3d-Metalle: Mn/N, Fe/N und Ni/N. Göttingen: Cuvillier Verlag, 1999.
- [51] Detavernier C, Lavoie C, d'Heurle FM. J Appl Phys 2003;93:2510.
- [52] Kooi BJ, Somers MAJ, Mittemeijer EJ. Metall Mater Trans A 1996;27A:1063.
- [53] Leineweber A, Jacobs H, Kockelmann W, Hull S, Hinz-Hübner D. J Alloys Compd 2004;384:1.
- [54] Touloukian YS, Kirby RK, Taylor RE, Desai PD. Thermal Expansion: Metallic Elements and Alloys. New York: IFI/Plenum, 1977.
- [55] Somers MAJ, Mittemeijer EJ. Surf Eng 1987;3:123.
- [56] Prenosil B. Härtereit-Tech Mitt 1973;28:157.
- [57] Kresse G, Furthmüller J. Comp Mat Sci 1996;6:15.
- [58] Kresse G, Furthmüller J. Phys Rev B 1996;54:11169.

***Elastic anisotropy of  $\gamma'$ -Fe<sub>4</sub>N and elastic grain interactions in  $\gamma'$ -Fe<sub>4</sub>N<sub>1-y</sub> layers on  $\alpha$ -Fe: first-principles calculations and diffraction stress measurements***

*T. Greßmann, M. Wohlschlägel, S. Shang, U. Welzel, A. Leineweber,  
E.J. Mittemeijer, Z.-K. Liu*

**Abstract**

The three independent single-crystal elastic-stiffness constants  $C_{ij}$  of cubic  $\gamma'$ -Fe<sub>4</sub>N (*fcc*-type iron substructure) have been calculated by first-principles methods using the density functional theory:  $C_{11} = 307.2$  GPa,  $C_{12} = 134.1$  GPa, and  $C_{44} = 46.0$  GPa. The Zener elastic-anisotropy ratio  $A = 2C_{44}/(C_{11}-C_{12}) = 0.53$  is strikingly  $< 1$ , implying  $\langle 100 \rangle$  as stiffest directions, whereas all *fcc* metals show  $A > 1$ . This elastic anisotropy is ascribed to the ordered distribution of nitrogen on the octahedral interstitial sites. X-ray diffraction lattice-strain measurements for a set of different *hkl* reflections recorded from  $\gamma'$ -Fe<sub>4</sub>N<sub>1-y</sub> layers on top of  $\alpha$ -Fe confirmed the ‘abnormal’ elastic anisotropy of  $\gamma'$ -Fe<sub>4</sub>N<sub>1-y</sub>. Stress evaluation, yielding a compressive stress of about  $-670$  MPa parallel to the surface, was performed using on the basis of *effective* X-ray elastic constants determined from the calculated single-crystal elastic constants  $C_{ij}$  and allowing a grain interaction intermediate between the Reuss and the Voigt model.

## 4.1 Introduction

Iron nitrides play an important role in materials science because their generation by nitriding procedures can improve the surface properties of iron-based alloys and steels [1-3]. Iron-nitride layers grown on the surface of iron and steel have been shown to enhance the resistance to wear and to corrosion [4, 5]. These compound layers usually consist of  $\epsilon$ -Fe<sub>3</sub>N<sub>1+x</sub>, in which the iron atoms are arranged hexagonally close packed, and of  $\gamma'$ -Fe<sub>4</sub>N<sub>1-y</sub> with a close packed cubic arrangement of the iron atoms (see also comments on the crystal structure below). The nitrogen atoms occupy in both nitrides octahedral interstitial sites of the iron substructure in a long-range ordered fashion [6-10]. The homogeneity range of the  $\epsilon$  phase is quite large, e.g. at 823 K from about 24 at.% N up to about 33 at.% N, whereas the homogeneity range of  $\gamma'$  is small, e.g. at 823 K from 19.58 at.% N to 19.94 at.% N [11, 12].

Due to their technological importance a number of studies have been performed on the formation of iron nitrides as surface compound layers. These surface layers are typically produced in the temperature range of about 773 K up to 863 K on top of ferritic iron or steel substrates by gaseous nitriding processes. The growth kinetics of the compound layers (single  $\gamma'$  as well as  $\epsilon/\gamma'$  compound layers) as well as phase transformations occurring in the compound layers were investigated [11, 13-18].

A particular property of iron-nitride compound layers are their residual macrostresses [19-22]. Such residual macrostresses arise due to the cohesion of the misfitting compound layer to the ferritic substrate and due to cohesion within the compound layer [19]. The macrostress-generating misfits can have various origins. They may, for example, arise because the transformation of the substrate phase into the compound layer phase is associated with a change of specific volume, and/or they are induced by temperature changes because substrate and compound layer have different coefficients of thermal expansion. A concentration gradient and associated strain-free lattice-spacing gradients within the layer can lead to depth-dependent macrostresses [19].

The analysis of stresses in surface layers by, usually, lattice-strain measurements using X-ray diffraction [23] requires knowledge of the elastic constants of the stressed, elastically anisotropic material. The single-crystal elastic constants are the basis for calculation of the so-called X-ray elastic constants, XECs, which are used for the evaluation of X-ray stress measurements [23]. For many technologically relevant materials the single-crystal elastic constants are not known. This is, in particular, the case for such substances which cannot be prepared as single crystals sufficiently large for measurement of the elastic constants. In many cases even the averaged isotropic elastic constants as determined for massive polycrystalline material, presumably texture-less, are not available.

Until now, no investigation on the determination of the single-crystal elastic constants  $C_{ij}$  of  $\gamma'$ -Fe<sub>4</sub>N has been performed. Some publications dealing with the analysis of residual stresses in  $\gamma'$  layers utilised the single-crystal elastic constants of austenitic steel for  $\gamma'$ -Fe<sub>4</sub>N<sub>1-y</sub>, since the same close-packed *fcc*-type arrangement of the iron atoms occurs in both materials (thereby neglecting the influence of alloying elements in the austenite, such as Ni and Cr [19]). In other works [21, 24-26] the single-crystal elastic constants of ferrite ( $\alpha$ -Fe) were used, which has a *bcc*-type arrangement of the iron atoms and it is rather unlikely that on that basis reliable estimates for the elastic constants of  $\gamma'$  can be obtained. Further, in the previous works only one single reflection of  $\gamma'$  was analysed in the X-ray stress measurements [19, 20, 24-26] and therefore possible effects of elastically anisotropic behaviour could not be revealed experimentally.

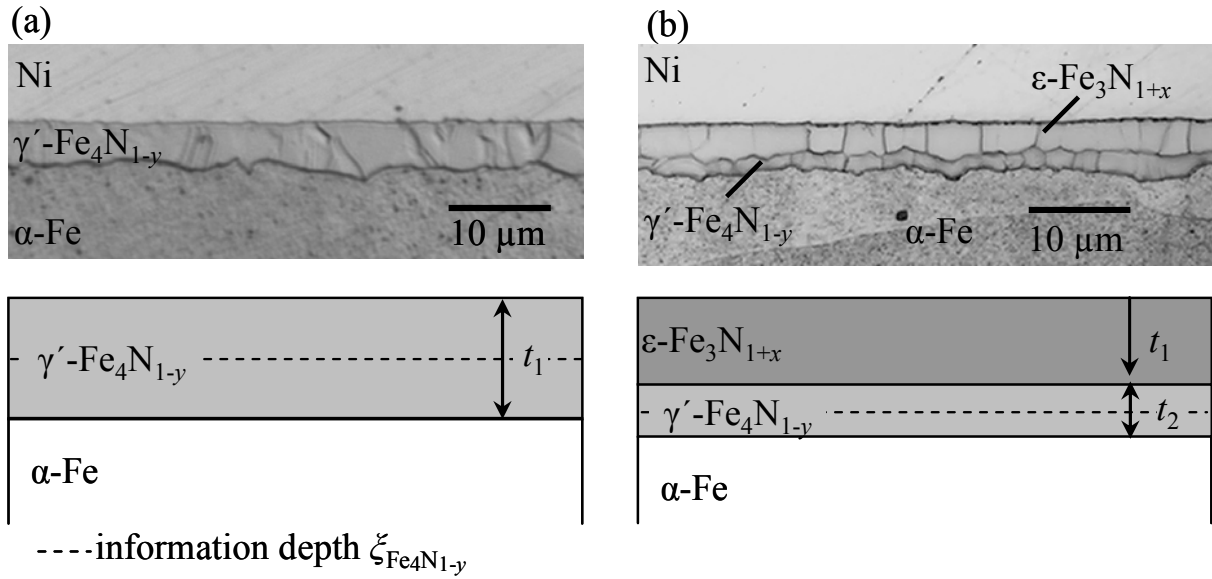


**Fig. 4.1:** Optical micrographs (bright field) of compound-layer cross sections of gas-nitrided  $\alpha$ -Fe sheets after Nital etching. The corresponding sketches given underneath illustrate the constitution of the layers: (a) specimen A with a single  $\gamma'$ - $\text{Fe}_4\text{N}_{1-y}$  layer and (b) specimen B with a double-layer consisting of  $\epsilon$ - $\text{Fe}_3\text{N}_{1+x}$  and  $\gamma'$ - $\text{Fe}_4\text{N}_{1-y}$ . The dashed lines in the sketches indicate the information depth of the X-rays originating from the  $\gamma'$ -(sub)layer for  $\text{CoK}\alpha$  radiation.

The present paper deals with determination of the single-crystal elastic constants  $C_{ij}$  of  $\gamma'$ - $\text{Fe}_4\text{N}$  on the basis of first-principles total-energy calculations. These constants were subsequently used in the course of the X-ray-diffraction analysis of residual stresses in and the anisotropic elastic behaviour of  $\gamma'$ - $\text{Fe}_4\text{N}_{1-y}$  layers (the notation ' $\text{Fe}_4\text{N}$ ' is used in this work for ideal  $\gamma'$  containing 20 at.% N as considered in the first-principles calculations, whereas for the experimentally produced  $\gamma'$  layers the notation  $\text{Fe}_4\text{N}_{1-y}$  is used in order to indicate the presence of the small homogeneity range, where always  $y > 0$  holds). The layers investigated were either a single  $\gamma'$ - $\text{Fe}_4\text{N}_{1-y}$  layer on top of  $\alpha$ -Fe or a  $\gamma'$ - $\text{Fe}_4\text{N}_{1-y}$  sublayer on top of  $\alpha$ -Fe underneath a surface-adjacent  $\epsilon$ - $\text{Fe}_3\text{N}_{1+x}$  sublayer (Fig. 4.1). On this basis the evaluation of the state of stress was performed using measurements of a set of different  $hkl$ -reflections of  $\gamma'$ - $\text{Fe}_4\text{N}_{1-y}$  simultaneously in the so-called  $f(\psi)$ -method [23, 27, 28]. The observed and, from the first-principles calculations, predicted elastic anisotropy, which was found to be abnormal for  $fcc$ -type metals, can be understood on the basis of the particular crystal structure of  $\gamma'$ - $\text{Fe}_4\text{N}$ .



## 4.2 First-principles calculations of elastic constants

### 4.2.1 Theoretical background and method of calculation used

Nowadays, it is possible to calculate with first-principles total-energy methods reliable values of the energies of arbitrary atomic configurations at 0 K, in particular for an ideal crystal, of which the atomic configuration (crystal structure) is given by the lattice vectors and the fractional coordinates of the atoms in the unit cell [29]. By systematic variation of these parameters describing the crystal structure, the minimum energy of the crystal can be found by determining the precise configuration of lowest energy. If this state of minimum energy is known, it is possible to explore the 'energy landscape' around this minimum, i.e. examining the dependence of the crystal's energy on deviations of structural parameters from their values pertaining to the minimum-energy (equilibrium) structure.

For an analysis of the elastic properties of the crystal one has to investigate the energy changes associated with distortions of the lattice vectors, with at the same time allowing relaxations of the fractional coordinates of the atoms in the unit cell. Such distortions can be conceived as the outcome of a strain imposed on the crystal as described by the strain tensor characterised by the six components  $\varepsilon_i$  according to the Voigtian matrix formulation of Hooke's law [30, 31]:

$$\boldsymbol{\varepsilon} = \begin{pmatrix} \varepsilon_1 & \varepsilon_6/2 & \varepsilon_5/2 \\ \varepsilon_6/2 & \varepsilon_2 & \varepsilon_4/2 \\ \varepsilon_5/2 & \varepsilon_4/2 & \varepsilon_3 \end{pmatrix}, \quad (4.1)$$

which modifies the lattice vectors  $\mathbf{a}$ ,  $\mathbf{b}$  and  $\mathbf{c}$  pertaining to the equilibrium state leading to the modified lattice vectors  $\mathbf{a}'$ ,  $\mathbf{b}'$  and  $\mathbf{c}'$ . If, with respect to a Cartesian coordinate system, the lattice vectors  $\mathbf{a}$ ,  $\mathbf{b}$  and  $\mathbf{c}$ , form the three columns of the matrix  $\mathbf{R}$ , e.g. for a primitive cubic lattice,

$$\mathbf{R} = \begin{pmatrix} a & 0 & 0 \\ 0 & a & 0 \\ 0 & 0 & a \end{pmatrix}, \quad (4.2)$$

then the matrix  $\mathbf{R}'$  contains the lattice vectors  $\mathbf{a}'$ ,  $\mathbf{b}'$  and  $\mathbf{c}'$  as its three columns

$$\mathbf{R}' = \mathbf{R}(\mathbf{1} + \boldsymbol{\varepsilon}) \quad (4.3)$$

where  $\mathbf{1}$  is the  $3 \times 3$  unit matrix with 1 as its three diagonal elements and 0 as its six off-diagonal elements.

According to basic elastic theory the change of the energy per unit cell, relative to the energy  $U_0$  of the equilibrium state,  $U - U_0$  (i.e. the elastic energy), depends, in the vicinity of  $U_0$ , on the components of the strain tensor (Eq. (4.1)) and the elastic stiffness tensor as follows [30, 31]:

$$U - U_0 = \frac{1}{2} V_0 C_{ij} \varepsilon_i \varepsilon_j, \quad (4.4)$$

where the Einstein notation used implies summation over  $i, j \in \{1..6\}$  and  $V_0$  represents the unit-cell volume of the equilibrium state. Eq. (4.4) implies that, by systematically imposing (in the calculation) different strains on the crystal and determining the corresponding energy changes, the elastic constants  $C_{ij}$  can be evaluated straightforwardly.

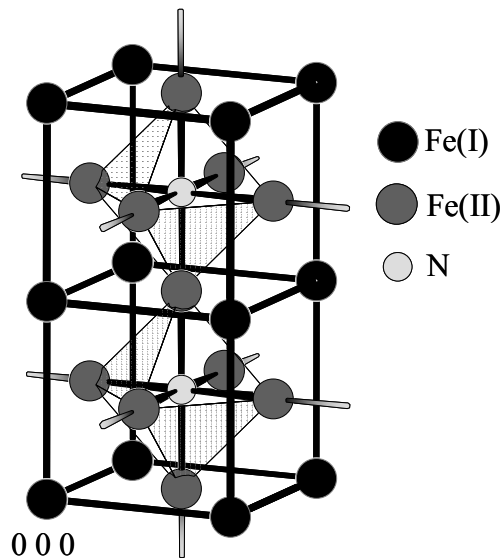


**Fig. 4.2:** Crystal structure of  $\gamma'$ -Fe<sub>4</sub>N (two unit cells). The different, with respect to the state of chemical bonding, iron atoms, Fe(I) and Fe(II), have been represented as spheres of the same size in black and dark grey. Nitrogen atoms occupying  $\frac{1}{4}$  of the octahedral sites (surrounded by shadowed octahedra) have been indicated with a smaller size and in light grey, and are connected in the  $\langle 100 \rangle$  directions by thick bars with neighbouring Fe(II) atoms.

Primitive cubic  $\gamma'$ -Fe<sub>4</sub>N has the space-group symmetry  $Pm\bar{3}m$ . Three inequivalent atomic sites Fe(I), Fe(II) and N with the following fractional coordinates occur: Fe(I): 0 0 0; Fe(II):  $\frac{1}{2}$   $\frac{1}{2}$  0,  $\frac{1}{2}$  0  $\frac{1}{2}$  and 0  $\frac{1}{2}$   $\frac{1}{2}$ ; N:  $\frac{1}{2}$   $\frac{1}{2}$   $\frac{1}{2}$  [6, 7] (see Fig. 4.2). The lattice parameter  $a_{\gamma'}$  has at room temperature a value of 3.7988 Å at the ideal Fe<sub>4</sub>N composition [32]. Note that, although the Fe(I) and Fe(II) together exhibit a *fcc*-type close-packed cubic arrangement, the ordered distribution of nitrogen on one fourth of the octahedral sites leads to a *primitive* cubic Bravais (i.e. translation) lattice. Because of the cubic symmetry of  $\gamma'$ -Fe<sub>4</sub>N only three independent elastic constants  $C_{11}$ ,  $C_{12}$  and  $C_{44}$  occur [30, 31]. These have been determined in this work by calculating the strain-energy changes associated with three different distortion types:

(i) Imposing an isotropic state of strain with  $\varepsilon_1 = \varepsilon_2 = \varepsilon_3 = \varepsilon$  and all other strains  $\varepsilon_i = 0$ , considering that the volume change with respect to  $V_0$  is related with  $\varepsilon$  by  $\varepsilon = \frac{1}{3}(V - V_0)/V_0$ . Eq. (4.4) then becomes

$$U - U_0 = \frac{3}{2}V_0(C_{11} + 2C_{12})\varepsilon^2 = \frac{9}{2}V_0B\varepsilon^2 = \frac{1}{2}B(V - V_0)^2 / V_0, \quad (4.5)$$

which allows to determine the sum of the elastic constants  $C_{11} + 2C_{12}$  and thus the bulk modulus  $B = \frac{1}{3}(C_{11} + 2C_{12})$ , by simultaneous fitting of  $V_0$  and  $U_0$  to the total energy data calculated for different  $V$  (or  $\varepsilon$ ).

Determination of  $B$  has not been performed directly employing Eq. (4.5). Instead, the parameters of a so-called *equation of state* (EOS) in a version suggested by Refs. [33, 34]<sup>4.1</sup>:

$$U(V) = a + bV^{-1/3} + cV^{-2/3} + dV^{-1}, \quad (4.6)$$

have been determined by fitting to the values of the total energy determined for different values of the unit-cell volume  $V$  (resulting from the specific isotropic distortion considered here). Then, the bulk modulus follows from the curvature at the minimum of  $U(V)$  that occurs at a unit-cell volume  $V_0$  [31]:

---

<sup>4.1</sup> In order to allow for consideration of non-parabolic behaviour of  $U$  for larger volume changes  $V-V_0$ . Eq. (4.5) holds only for small changes in volume  $V-V_0$ .

$$B = -V \left( \frac{\partial^2 U}{\partial V^2} \right)_{V=V_0}. \quad (4.7)$$

$B$  can now be directly calculated from the fit parameters  $a$ ,  $b$ ,  $c$  and  $d$  (Eq. (4.6)), as described in detail in Ref. [34]:

$$B = \frac{1}{3}(C_{11} + 2C_{12}) = \frac{2}{9}V_0^{-2} (9d + 5cV_0^{1/3} + 2bV_0^{2/3}). \quad (4.8)$$

(ii) Imposing an uniaxial state of strain:  $\varepsilon_1 = \varepsilon$  and all other strains  $\varepsilon_i = 0$ . Eq. (4.4) then becomes

$$U - U_0 = \frac{1}{2}V_0 C_{11} \varepsilon^2, \quad (4.9)$$

which leads to determination of the elastic constant  $C_{11}$ .

(iii) Imposing a shear strain:  $\varepsilon_4 = \varepsilon$  and all other  $\varepsilon_i = 0$ . Eq. (4.4) then becomes

$$U - U_0 = \frac{1}{2}V_0 C_{44} \varepsilon^2, \quad (4.10)$$

which leads to determination of the elastic constant  $C_{44}$ .

The first-principles total-energy calculations performed in this work for determination of the elastic constants utilised the density functional theory as applied in the *Vienna ab initio simulation package* (VASP, version 4.6) [35, 36]. The projector-augmented wave (PAW) [37] method was adopted to describe the electron-ion interaction, because of its efficient implementation of force, while combining the accuracy of all-electron methods with the efficiency of pseudopotentials. The generalized gradient approximation (GGA) [38] was used for the exchange-correlation potential. The wave functions were sampled on a  $20 \times 20 \times 20$   $k$ -point mesh constructed by the Monkhorst–Pack method [39]. The integration of the band-structure energy over the Brillouin zone was performed by the tetrahedron method incorporating the Blöchl corrections [40]. The energy cutoff on the wave function was taken as 520 eV and the convergence criterion for electronic self-consistency was  $10^{-7}$  eV per unit cell. The projected wave functions were evaluated in reciprocal space in order to get exact total energies. Recognising the ferromagnetic nature of  $\gamma'$ -Fe<sub>4</sub>N [41], the first-

principles calculations were performed adopting the spin-polarized approximation for considering the magnetic interactions.

### 4.2.2 Results

The energies calculated for crystals strained to different extents according to the distortion types (i)-(iii) (see section 4.2.1.) could be well described by Eq. (4.6), Eq. (4.9) and Eq. (4.10); see Figs. 4.3a-c. The thus obtained values by fitting for  $B = \frac{1}{3}(C_{11} + 2C_{12})$ ,  $C_{11}$  and  $C_{44}$  have been gathered in Table 4.1 together with the value for  $C_{12}$  calculated from the values of  $C_{11}$  and  $B$ . As equilibrium volume  $V_0 = 54.6385 \text{ \AA}^3$  per unit cell, corresponding to  $a_{\gamma'} = 3.7946 \text{ \AA}$ , was obtained from the fitted parameters of Eq. (4.6). The elastic-compliance constants,  $S_{ij}$ , calculated from  $C_{ij}$  have also been given in Table 4.1. Further, Table 4.1 lists the values for the Zener anisotropy ratio

$$A = \frac{2C_{44}}{C_{11} - C_{12}} = \frac{2(S_{11} - S_{12})}{S_{44}} \quad (4.11)$$

and 'aggregate, mechanical elastic properties' (pertaining to a texture-less polycrystalline specimen) as the averaged Young's modulus  $E$  and the averaged shear modulus  $G$ , adopting Voigt and Reuss types of grain interaction. Note that the values for the elastic constants of  $\gamma'$ -Fe<sub>4</sub>N presented in Table 4.1 hold for 0 K (see above).

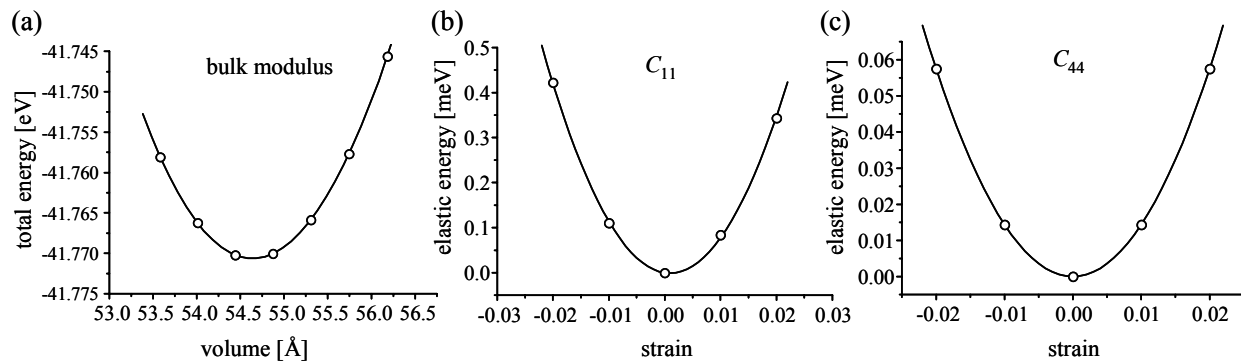


**Fig. 4.3:** Calculated (symbols) and fitted (lines) total energy of  $\gamma'$ -Fe<sub>4</sub>N as function of unit-cell volume to obtain (a) the bulk modulus  $B$ , and the elastic energy of  $\gamma'$ -Fe<sub>4</sub>N as function of the strain to obtain the elastic constants (b)  $C_{11}$  and (c)  $C_{44}$  (corresponding to the distortion modes (i)-(iii), section 4.2.1). Error bars are of the size of the symbols and are therefore omitted.

**Table 4.1:** Single-crystal elastic constants of  $\gamma'$ -Fe<sub>4</sub>N (calculated for 0 K; present work), austenitic steel and  $\alpha$ -Fe (experimental results taken from literature for ambient temperature): elastic stiffnesses  $C_{ij}$  and compliances  $S_{ij}$ , and the corresponding bulk modulus  $B = \frac{1}{3}(C_{11} + 2C_{12})$  (for comparison with literature data as given) and elastic anisotropy  $A = 2C_{44}/(C_{11}-C_{12})$ . For texture-less, polycrystalline specimens the average Young's modulus'  $E_{\text{Voigt}} = 9BG_{\text{Voigt}}/(G_{\text{Voigt}}+3B)$ ,  $E_{\text{Reuss}} = ((3S_{11}+2S_{12}+S_{44})/5)^{-1}$  [44, 72] and the average shear modulus  $G_{\text{Voigt}} = (C_{11}-C_{12}+3C_{44})/5$ ,  $G_{\text{Reuss}} = ((4S_{11}-4S_{12}+3S_{44})/5)^{-1}$  [44, 72] have been given as well.

	$C_{11}$	$C_{12}$	$C_{44}$	$S_{11}$	$S_{12}$	$S_{44}$	$B$	$A$	$E_{\text{Voigt}}$	$G_{\text{Voigt}}$	$E_{\text{Reuss}}$	$G_{\text{Reuss}}$
	[GPa]			$[10^{-3} \text{ GPa}^{-1}]$			[GPa]		[GPa]			
$\gamma'$ -Fe <sub>4</sub> N	307.2	134.1	46.0	4.43	-1.35	21.7	191.8 <sup>a</sup> 191.1 [34] <sup>a</sup> 196 [60] <sup>b</sup> 155 [61] <sup>b</sup>	0.53	168.4	62.2	154.6	56.6
$\gamma$ (Fe-Cr-Ni alloy) [62]	232.5	161.6	123.5	10	-4.1	8.1	185.2	3.48	228.5	88.3	167.2	62.0
$\alpha$ -Fe [73]	251.0	157.0	112.0	7.68	-2.96	8.93	188.3	2.38	223.9	86	191.8	72.1

<sup>a</sup> calculated for 0 K

<sup>b</sup> experimentally determined at room temperature

### 4.3 Macrostrains and macrostresses in $\gamma'$ -Fe<sub>4</sub>N<sub>1-y</sub> layers

#### 4.3.1 Determination of residual macrostresses by diffraction methods

The analysis of mechanical, macroscopical stresses in polycrystalline surface layers by X-ray diffraction methods has been reviewed in references [23, 42]. In the absence of crystallographic texture and of direction-dependent (anisotropic) elastic grain interaction, polycrystalline surface layers are macroscopically elastically isotropic (neglecting effects at the edges of the specimen). The absence of crystallographic texture for the specimens investigated has been verified experimentally employing X-ray diffraction (cf. section 4.3.3.2). For a discussion of the grain interaction in the specimen, cf. section 4.4.2.

Considering that the  $\gamma'$ -Fe<sub>4</sub>N<sub>1-y</sub> layers investigated have been produced by gaseous nitriding of polycrystalline  $\alpha$ -Fe substrates (see section 4.3.2.1.), the layers

exhibit a rotationally symmetric biaxial state of stress (verified experimentally; see section 4.3.2.2.) parallel to the specimen surface, i.e.  $\sigma_{//} \equiv \sigma_{11} = \sigma_{22}$ . Then the stress is connected to the strain by [23]:

$$\varepsilon_{\psi}^{hkl} = (d_{\psi}^{hkl} - d_0^{hkl}) / d_0^{hkl} = (2S_1^{hkl} + \frac{1}{2}S_2^{hkl} \sin^2 \psi) \cdot \sigma_{//}, \quad (4.12)$$

where  $\varepsilon_{\psi}^{hkl}$  is the strain in the direction of the diffraction vector, i.e. for a tilt angle,  $\psi$ , with respect to the specimen surface normal,  $d_{\psi}^{hkl}$  denotes the strained lattice spacing,  $d_0^{hkl}$  represents the strain-free, reference lattice spacing and  $S_1^{hkl}$  and  $\frac{1}{2}S_2^{hkl}$  are the X-ray elastic constants (XECs). The XECs depend on the single-crystal elastic constants  $C_{ij}$ <sup>4.2</sup> and on the (type of) elastic grain interaction occurring in the specimen [43].

For a cubic material, using a series of different lattice spacings  $d_{\psi}^{hkl}$  for various  $hkl$  measured at different tilt angles  $\psi$  the stress  $\sigma_{//}$  can be determined from a plot of  $d_{\psi}^{hkl} (h^2 + k^2 + l^2)^{1/2}$  versus

$$f(\psi) = a_{\text{ref}} (2S_1^{hkl} + \frac{1}{2}S_2^{hkl} \cdot \sin^2 \psi), \quad (4.13)$$

where  $a_{\text{ref}}$  denotes the reference lattice parameter. The slope of the straight line in the plot equals the macroscopic stress [23, 28]. This so-called ' $f(\psi)$  method' is a generalization of the conventional  $\sin^2\psi$  method (where in the latter the strain  $\varepsilon_{\psi}^{hkl}$ , recorded from a single  $hkl$  reflection, is plotted versus  $\sin^2\psi$ ; cf. Eq. (4.12)). Note that the  $f(\psi)$  method is based on the same assumptions stated above for the traditional  $\sin^2\psi$  method and the two approaches are equivalent (for a discussion of advantages of the approach based on the use of Eq. (4.13), cf. [23]). In order to find a reliable value of the stress  $\sigma_{//}$ ,  $a_{\text{ref}}$  needs not to be known precisely, since it is of minor importance for the outcome of the stress evaluation [28]. Application of the  $f(\psi)$  method in principle allows, simultaneously with the determination of  $\sigma_{//}$ , determination of the *effective* X-ray elastic constants for each  $hkl$  according to

---

<sup>4.2</sup> Note that  $\sigma_{11}$  and  $\sigma_{22}$  refer to the specimen frame of reference (for which the  $z$ -axis is oriented perpendicularly to the specimen surface and the  $x$  and  $y$  axes lie in the surface plane), whereas the elastic constants  $C_{ij}$  refer to the crystallographic frame of reference.

$$S_{1,2}^{hkl} = wS_{1,2}^V + (1-w)S_{1,2}^{R,hkl} \quad (4.14)$$

via determination of a weighting factor,  $w$ , which weights between the extreme values for the diffraction elastic constants (XECs) as given by the Voigt type of grain interaction, which, for cubic materials, yields [23, 44, 45]

$$S_1^V = -(C_{11} - 2C_{44} + 4C_{12}) / [2(C_{11} + 3C_{44} - C_{12})(C_{11} + 2C_{12})], \quad (4.15)$$

$$\frac{1}{2}S_2^V = 15 / (2C_{11} + 6C_{44} - 2C_{12}) \quad (4.16)$$

and by the Reuss type of grain interaction [23, 45], which, for cubic materials and using Eq. (4.11), yields

$$S_1^{R,hkl} = 2S_{12} + \frac{1}{2}S_{44}(A-1)\Gamma_{hkl}, \quad (4.17)$$

$$\frac{1}{2}S_2^{R,hkl} = AS_{44} - \frac{3}{2}S_{44}(A-1)\Gamma_{hkl}, \quad (4.18)$$

where  $\Gamma_{hkl} = (h^2k^2 + h^2l^2 + k^2l^2) / (h^2 + k^2 + l^2)^2$  is the orientation factor for cubic materials.

Note that  $S_{1,2}^V$  does not depend on  $hkl$ ; see also Fig. 4.4b and its discussion in section 4.4.1. Often the Neerfeld-Hill approach has been applied for calculation of  $S_{1,2}^{hkl}$ , which implies a value for  $w$  equal to  $\frac{1}{2}$ . It follows that, for some value of  $w$ , a plot of  $\frac{1}{2}S_2^{hkl}\sigma_{//}$  (cf. Eq. (4.12)) vs.  $\Gamma_{hkl}$  yields a straight line (this result is used in section 4.3.3; see Fig. 4.4). Both  $\sigma_{//}$  and  $w$  can be obtained by least-squares fitting of a straight line to the experimental data in the  $f(\psi)$  plot [46].

In the course of X-ray diffraction analysis of stress in surface layers the probed volume varies with  $\psi$  due to the  $\psi$ -dependent absorption of X-rays in solids. This X-ray attenuation has in particular to be considered if stress and/or concentration gradients occur within the probed volume. Concentration gradients for instance lead usually to lattice-spacing gradients, since different compositions of the same phase commonly result in different lattice spacings [32]. Such changes in the lattice spacing with depth may also lead to peak shifts with changing  $\psi$ , as macrostresses do.



Therefore,  $\psi$ -dependent line shifts due to concentration gradients may be misinterpreted in terms of the presence of stresses, leading to so-called ghost-stresses [19, 47].

The  $\psi$ - and  $\theta$ -dependent sampled volume of a sublayer  $i$  that ranges from depth  $t_{i-1}$  to  $t_{i-1}+t_i$  (see Fig. 4.1) can be quantified by the information depth  $\xi_i$ . The information depth is the averaged depth obtained upon weighting each depth  $z$  with the X-ray attenuation due to absorption of the signal originating from depth  $z$  [42]:

$$\xi_i = \langle z \rangle = \frac{\int_{t_{i-1}}^{t_{i-1}+t_i} z \exp(-\mu kz) dz}{\int_{t_{i-1}}^{t_{i-1}+t_i} \exp(-\mu kz) dz}. \quad (4.19)$$

The brackets ' $\langle \rangle$ ' indicate averaging,  $t_i$  denotes the thickness of the layer  $i$ ,  $t_{i-1}$  is the depth beneath the surface where layer  $i$  begins,  $\mu$  is the linear absorption coefficient and  $k$  represents a diffraction-geometry dependent factor<sup>4.3</sup>. For a single layer  $i$  of thickness  $t_i$  the information depth can then be calculated according to:

$$\xi_i = \langle z \rangle = \frac{1}{\mu k} - \frac{t_i \exp(-\mu k t_i)}{1 - \exp(-\mu k t_i)} \quad (4.20)$$

and for layer  $i$  underneath a layer  $i-1$  (of thickness  $t_{i-1}$ ) via:

$$\xi_i = \langle z \rangle = \frac{t_{i-1} \mu k \exp(t_i \mu k) - t_{i-1} \mu k - t_i \mu k - 1}{k \mu (\exp(t_i \mu k) - 1)}. \quad (4.21)$$

In the extreme case, if the absorption coefficient  $\mu$  is zero, the average information depth  $\xi_i$  equals  $t_{i-1} + \frac{1}{2} t_i$ .

In the present study the wavelength and the maximum tilt angle were chosen such (see section 4.3.2.2) that the X-ray attenuation is sufficiently small with respect to the layer thickness, so that  $\xi_i = t_{i-1} + \frac{1}{2} t_i$  holds and therefore the information depth is

---

<sup>4.3</sup> For a powder diffractometer allowing  $\omega$  tilt ( $\omega$  axis coincides with  $\theta$  axis;  $\omega$  takes the role of  $\psi$ ),  $k$  is given by  $k = (2 \sin\theta \cos\omega) / (\sin^2\theta - \sin^2\omega)$ , whereas for a powder diffractometer allowing only  $\chi$  tilt ( $\chi$  is the angle of rotation of the sample around the axis defined by the intersection of the diffraction plane and the sample surface, i.e. perpendicular to the  $\theta/2\theta$  plane;  $\chi$  coincides in the  $\chi$ -mode with the angle  $\psi$ ), the relation is  $k = 2 / (\sin\theta \cos\psi)$  [48].

virtually independent of  $\psi$ . Thereby, the possible effect of stress gradients and composition gradients within the  $\gamma'$  layer, as e.g. dealt with in Ref. [19], is averaged out in the present work.

## 4.3.2 Experimental

### 4.3.2.1 Specimen preparation and metallography

Specimens in the form of rectangular discs (18 mm  $\times$  25 mm  $\times$  1 mm) were prepared from a cold-rolled  $\alpha$ -Fe (Alpha Aesar 99.98 wt.%) cast rod. Prior to nitriding the specimens were recrystallised for 2 hours at 973 K in hydrogen, mechanically polished up to 1  $\mu$ m diamond paste and finally ultrasonically cleaned in ethanol.

The nitriding treatments were performed at 823 K in a vertical quartz-tube furnace in  $\text{NH}_3$  (99.999 vol.%) /  $\text{H}_2$  (99.999 vol.%) gas mixtures. Compositions of the nitriding gas atmospheres and the nitriding times were chosen that two different nitride layers were obtained on top of the ferrite substrate: (a) a single  $\gamma'$ - $\text{Fe}_4\text{N}_{1-y}$  surface layer of about 6  $\mu$ m thickness (43 vol.%  $\text{NH}_3$  / 57 vol.%  $\text{H}_2$ ; nitriding time of 5 h; further denoted as specimen A) and (b) an  $\epsilon/\gamma'$  double layer, with a 3.0  $\mu$ m thick  $\epsilon$ - $\text{Fe}_3\text{N}_{1+x}$  sublayer adjacent to the surface and a  $\gamma'$ - $\text{Fe}_4\text{N}_{1-y}$  sublayer underneath of 1.8  $\mu$ m thickness (56 vol.%  $\text{NH}_3$  / 44 vol.%  $\text{H}_2$ ; nitriding time of 1.5 h; further denoted as specimen B). According to the preparation conditions and the thermodynamic data of the Fe-N system [11, 13],  $y$  ranges from 0.021 ( $\gamma'$  in equilibrium with  $\alpha$ -Fe) to 0.003 for specimen A ( $\gamma'$  in equilibrium with  $\epsilon$ - $\text{Fe}_3\text{N}_{1+x}$ ) and from 0.021 to 0.005 for specimen B ( $\gamma'$  in equilibrium with the gas atmosphere). After nitriding the specimens were quenched by dropping them into cold water flushed with  $\text{N}_2$ .

Optical microscopy of the nitrided specimens was performed applying a Leica DM RM microscope. Embedded cross-sections (covered with a protective nickel layer [49, 50]) were ground, polished and etched in 1 vol.% Nital containing 0.1 vol.% HCl [51, 52]. For each specimen several cross-sectional micrographs were taken close to both faces of the specimen and the surface-layer thicknesses were determined from these micrographs: the measured area of the layer was divided by the measured lateral length of the layer, yielding the layer thickness. The values of several micrographs were arithmetically averaged [16].

#### 4.3.2.2 X-ray diffractometry

X-ray diffraction analysis for specimens A and B was performed employing a Philips (now PANalytical) MR diffractometer equipped with a Eulerian cradle and using CoK $\alpha$  radiation ( $\lambda_{\alpha 1} = 1.78897 \text{ \AA}$ ,  $\lambda_{\alpha 2} = 1.79285 \text{ \AA}$ ;  $\mu_{\text{Fe}_4\text{N,CoK}\alpha} = 0.039 \text{ \mu m}^{-1}$ ) emerging from the point focus of a sealed tube and converted into a quasi-parallel beam by an X-ray lens. The size of the incident beam was set to 4 mm  $\times$  4 mm by crossed slits. The divergence of the incident beam coming out of the X-ray lens was approximately 0.3°. The diffracted beam passed a parallel-plate collimator (0.18° acceptance angle) and a flat graphite monochromator before being detected by a gas proportional counter.

High-resolution X-ray diffraction measurements were additionally carried out for specimen B using synchrotron radiation (B2 station equipped with a Eulerian cradle, HASYLAB, Hamburg); the corresponding, very small instrumental broadening reduced the occurrence of overlap of some  $\varepsilon$  reflections close to  $\gamma'$  reflections (the  $\varepsilon$  reflections are analysed in a forthcoming work [53]), in contrast with the in-house diffractometer. The beamline was used in the direct, unmirrored beam configuration [54], the wavelength was adjusted to  $\lambda = 0.80017 \text{ \AA}$  ( $\mu_{\text{Fe}_4\text{N,0.8\AA}} = 0.0346 \text{ \mu m}^{-1}$ ) and the beam size to 5 mm  $\times$  1 mm. The diffracted beam passed a Ge (111) analyzer crystal before being detected by a NaI scintillation counter.

During all measurements the samples were rotated around the surface normal in order to achieve better crystallite statistics; the rotational symmetry of the state of stress,  $\sigma_{//} \equiv \sigma_{11} = \sigma_{22}$ , was confirmed by additional stress measurements at different rotation angles,  $\varphi$ , around the surface normal. For stress measurements both diffractometers were used in  $\chi$ -mode [23, 42] in symmetrical diffraction geometry. Several  $\gamma'$ -Fe<sub>4</sub>N<sub>1-y</sub> fundamental reflections were recorded in the tilt-angle range of  $\psi = 0^\circ$  to  $60^\circ$ . The step-size in  $2\theta$  varied between  $0.002^\circ$  and  $0.04^\circ$  depending on the applied instrument and on the  $hkl$ -reflection.  $\psi$ -dependent analysis of the reflection intensities (not shown) revealed the absence of crystallographic texture. The very weak superstructure reflections due to nitrogen ordering were not considered in the measurements.

The positions of the  $\gamma'$ -Fe<sub>4</sub>N<sub>1-y</sub> reflections (for both above described measurement conditions) were obtained by profile fitting using pseudo-Voigt functions [55].

### 4.3.3 Results of X-ray stress analysis

Evaluation of conventional strain  $\varepsilon_{\psi}^{hkl}$  versus  $\sin^2\psi$  plots (cf. Eq. (4.12); plots not shown), each plot for a different  $hkl$ , revealed that the slopes  $\frac{1}{2}S_2^{hkl} \cdot \sigma_{//}$  of the straight lines vary systematically with  $hkl$ . The slopes,  $\frac{1}{2}S_2^{hkl} \cdot \sigma_{//}$ , for the various  $hkl$  have been plotted in Fig. 4.4a as function of the orientation factor,  $\Gamma_{hkl}$ , for specimen A as well as for specimen B (including both the in-house CoK $\alpha$  and the synchrotron measurements). The range of  $3\Gamma_{hkl}$  varies between 0 ( $h00$  planes) and 1 ( $hhh$  planes). Evidently, the  $h00$  reflections show smaller absolute slopes  $\frac{1}{2}S_2^{hkl} \cdot \sigma_{//}$  (i.e. less negative) than the  $hhh$  reflections, thereby indicating the occurrence of a distinct elastic anisotropy of  $\gamma'$ . For intrinsically elastically isotropic materials and for intrinsically elastically anisotropic polycrystalline materials in the case of Voigt grain interaction  $\frac{1}{2}S_2^{hkl}$  should not depend on  $hkl$ , i.e. on  $\Gamma_{hkl}$ , as indicated by the dotted line in Fig. 4.4b for a constant stress  $\sigma_{//}$ , whereas, according to the Reuss grain interaction, elastically anisotropic *cubic* materials exhibit linear dependencies of  $\frac{1}{2}S_2^{hkl}$  on  $\Gamma_{hkl}$  (cf. Eq. (4.18) and its discussion; see also Fig. 4.4b, solid line (Reuss model:  $w = 0$ ) and dashed line (Neerfeld-Hill approach:  $w = \frac{1}{2}$ )).

The straight lines in Fig. 4.4a represent linear least-squares fits of  $\frac{1}{2}S_2^{hkl} \cdot \sigma_{//}$  vs.  $3\Gamma_{hkl}$  for the two specimens. It should be mentioned here that the  $\frac{1}{2}S_2^{hkl} \cdot \sigma_{//}$  value obtained from the weak 400 reflection of sample A has not been considered in the linear fit, since it deviates apparently from the corresponding result obtained from the strong 200 reflection (for specimen B the 400 reflection could not even be measured, due to its very low intensity). As both the 200 reflection and the 400 reflection originate from the same set of lattice planes, the corresponding slopes in the  $\sin^2\psi$  plots should be equal. The difference between the slopes for the 200 and the 400 reflections then may, for example, be caused by an orientation dependence (with respect to the specimen frame of reference) of the stacking fault probability [56].

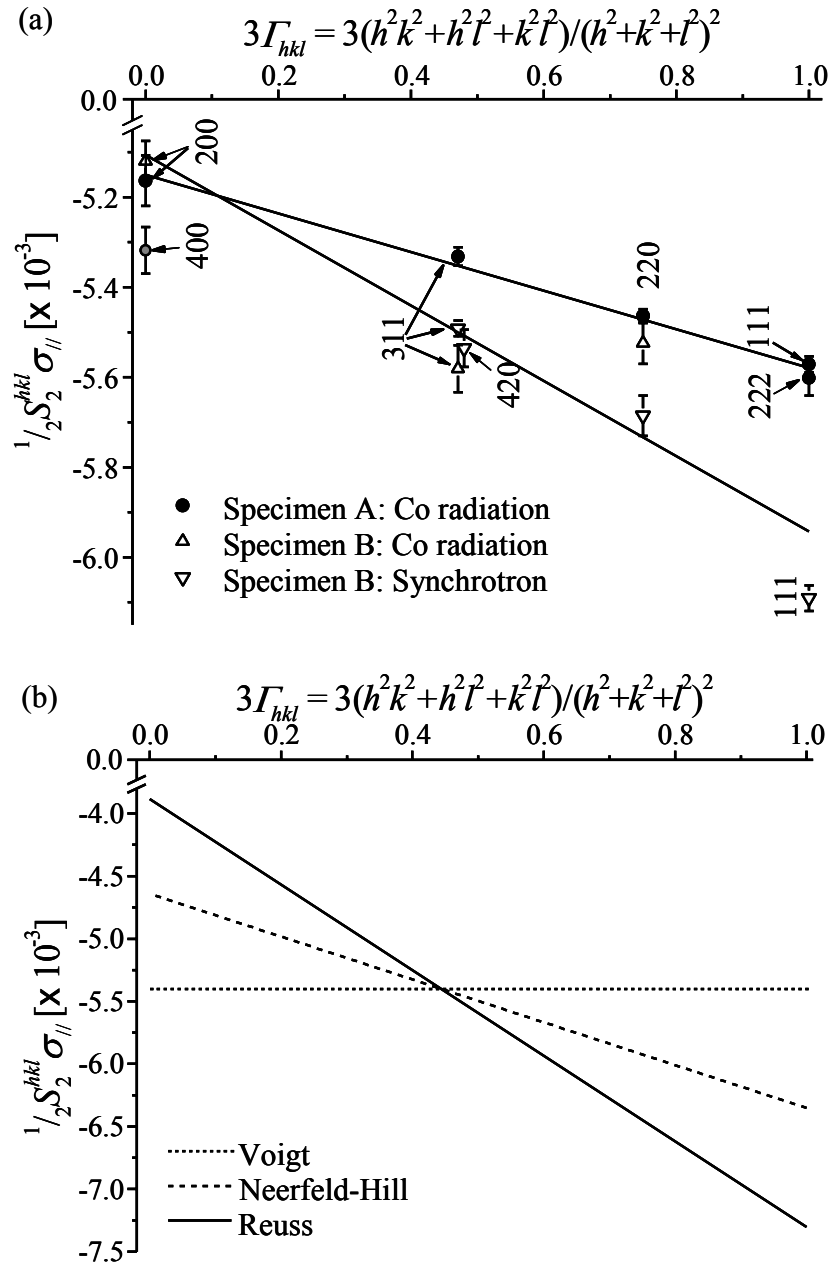


**Fig. 4.4:** (a) Experimentally determined variation of the slope  $\frac{1}{2} S_2^{hkl} \cdot \sigma_{||}$  with  $\Gamma_{hkl}$ . The values of  $\frac{1}{2} S_2^{hkl} \cdot \sigma_{||}$  have been obtained from the straight lines of  $\varepsilon_{\psi}^{hkl}$  vs.  $\sin^2\psi$  plots of the  $\gamma'$ -Fe<sub>4</sub>N<sub>1-y</sub> layers of specimens A and B. The solid lines represent linear fits to the data pertaining to specimens A (circles) and B (triangles). The grey circle represents the  $\gamma'$ -Fe<sub>4</sub>N<sub>1-y</sub> 400 reflection recorded from specimen A, which was not used for fitting of the straight line (see text). (b) Calculated evolution of the orientation dependence of  $\frac{1}{2} S_2^{hkl} \cdot \sigma_{||}$  vs.  $3\Gamma_{hkl}$  for the Voigt (dotted line), Reuss (solid line) and the averaged Neerfeld-Hill (dashed line) types of grain interaction in a texture-less polycrystal calculated for  $\sigma_{||} = -670$  MPa using the single-crystal elastic constants of  $\gamma'$ -Fe<sub>4</sub>N as obtained by first-principles calculations. Note that figure (b) has an ordinate scale different from figure (a).

The single-crystal elastic constants of  $\gamma'$ -Fe<sub>4</sub>N as obtained by first-principles calculations (presented in section 4.4.2) were used to calculate the diffraction elastic constants according to the Voigt and Reuss models for grain interaction (Eqs. (4.15 – 4.18)). Then, the  $f(\psi)$  method was applied as described in section 4.3.1. The  $f(\psi)$  plot as obtained for specimen A, where the data obtained from the 111, 200, 220, 311 and 222 reflections were used simultaneously, is shown in Fig. 4.5a. The  $f(\psi)$  plot of specimen B is presented for both the in-house measurements (200, 220 and 311 reflections) and the synchrotron measurements (111, 220, 311 and 420 reflections) in Fig. 4.5b. In both cases the dependence of  $d_{\psi}^{hkl} \cdot (h^2 + k^2 + l^2)^{1/2}$  on  $f(\psi)$  can very well be described by a straight line. The straight-line fit to these data provides values for the stress  $\sigma_{//}$  and the weighting parameter  $w$  (cf. Eq. (4.14)). As a result of the fitting of straight lines (cf. section 4.3.1) it was obtained for the weighting parameter:  $w = 0.85$  for specimen A and  $w = 0.80$  for specimen B (in the fitting an instrumental offset in  $2\theta$  was used as additional fit parameter [46]). These results indicate near-Voigt type grain interaction in the investigated layers. Further, the fitting yielded values for the stresses in both specimens for the  $\gamma'$ -layers:  $\sigma_{//} = -(665 \pm 2)$  MPa for specimen A and  $\sigma_{//} = -(681 \pm 5)$  MPa for specimen B. The mechanical strain parallel to the surface  $\varepsilon_{//}^{\text{mech}}$  can now be obtained according to Eq. (4.12) from  $\sigma_{//}$  (here the average of the above measured stress values has been taken) and the effective X-ray elastic constants at  $\Gamma = \frac{1}{5}$ , because for cubic materials it holds that  $S_{1,2}^{\text{mech}} = S_{1,2}^{hkl} (\Gamma = \frac{1}{5})$  [28, 45, 57]. It is obtained:  $\varepsilon_{//}^{\text{mech}} = 2.6 \cdot 10^{-3}$ .

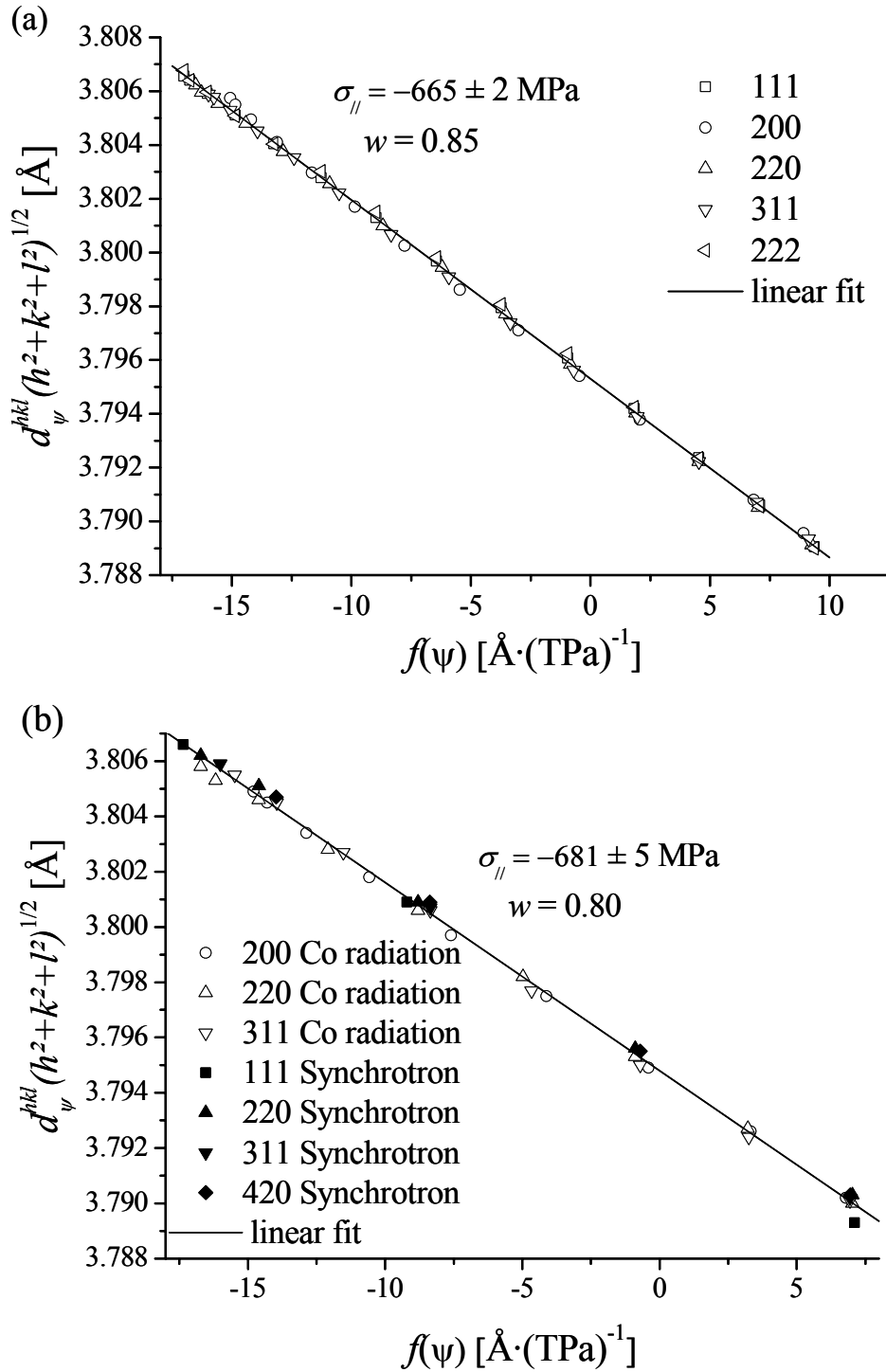


**Fig. 4.5:** Stress analysis employing the  $f(\psi, hkl) = a_{ref} (2S_1^{hkl} + \frac{1}{2}S_2^{hkl} \cdot \sin^2 \psi)$  method for (a) specimen A (using only Co radiation) and (b) specimen B (using both Co radiation – open data points – and synchrotron data – solid data points). The slopes of the straight lines correspond to the stresses present in the  $\gamma'$ -Fe<sub>4</sub>N<sub>1-y</sub> layers. The weighting parameter  $w$  represents the weighting between the Voigt ( $w = 1$ ) and Reuss ( $w = 0$ ) types of grain interaction. Error bars are of the size of the symbols and are therefore omitted.

The strain in the  $\gamma'$ -layer is mainly due to the thermal misfit between the  $\gamma'$ -layer and the  $\alpha$ -Fe substrate induced upon cooling as a consequence of the difference between the coefficients of thermal expansion of layer and substrate, as can be shown as follows. The thermal strain in  $\gamma'$  parallel to the surface,  $\varepsilon_{//}^{th}$ , induced upon quenching from the nitriding temperature,  $T_1$  (at which the layer can be assumed to be largely macrostress free), down to ambient temperature,  $T_2$ , can be calculated from (taking the substrate, thick as compared to the layer, as rigid):

$$\varepsilon_{//}^{th} = \int_{T_1}^{T_2} (\alpha_{\gamma'-Fe_4N} - \alpha_{\alpha-Fe}) \cdot dT. \quad (4.22)$$

The coefficients of thermal expansion for the layer and the substrate were taken from literature ( $\alpha_{\gamma'} = (7.6 \pm 0.8) \cdot 10^{-6} \text{ K}^{-1}$  [32] and  $\alpha_{\alpha-Fe} = 14.7 \cdot 10^{-6} \text{ K}^{-1}$ , with  $\alpha_{\alpha-Fe}$  as an average obtained via integration over the temperature interval from 293 K to 823 K [58]). From these data a strain of  $\varepsilon_{//}^{th} = (3.8 \pm 0.5) \cdot 10^{-3}$  was calculated, which indeed is of the same order of magnitude as the mechanical strain value derived above.

The difference between the experimentally measured value of mechanical strain and the predicted value according to Eq. (4.22) can be understood if the thermal strain is built up during cooling from temperatures below 690 K. This implies that during the first 130 K of cooling (823 K to 690 K) strain relaxation appears to occur, which agrees with observations made earlier for  $\gamma'$ -Fe<sub>4</sub>N<sub>1-y</sub> layers [19, 59].

## 4.4 Discussion

### 4.4.1 Interpretation of the calculated single-crystal elastic constants

Until now only a few data on only the bulk modulus of  $\gamma'$ -Fe<sub>4</sub>N have been presented earlier in the literature. The equilibrium lattice parameter and bulk modulus estimated from the present first-principles calculations agree well with the value of the bulk modulus obtained from a previous FP-LAPW (= Full Potential Linear Augmented Plane Wave) calculation [34] (cf. Table 4.1). Further, the calculated value for the bulk modulus is very close to a value determined previously from diamond-anvil-cell high-



pressure X-ray diffraction experiments [60]. As compared to this agreement, it appears that the result from a similar high-pressure X-ray diffraction experiment [61] deviates.

It may be proposed that the calculated elastic properties of  $\gamma'$ -Fe<sub>4</sub>N can be compared with corresponding experimental values for austenitic steel [62], which have been suggested as an approximation to the elastic constants of  $\gamma'$ -Fe<sub>4</sub>N [19, 20] since austenitic steel has the same *fcc*-type arrangement of the matrix (mostly iron) atoms.

Almost every cubic material exhibits an orientation dependence of the elastic properties. This anisotropy can be quantified e.g. by the Zener anisotropy ratio  $A = 2C_{44}/(C_{11}-C_{12}) = 2(S_{11}-S_{12})/S_{44}$  (Eq. 4.11), being 1 for elastically isotropic material. This elastic anisotropy can be visualised by the orientation dependence of e.g. the single-crystal's Young's modulus  $E_{hkl}$ . The orientation dependence of the Young's modulus (i.e. the Young's modulus in the direction perpendicular to the lattice planes  $hkl$ ) reads for cubic material [30, 31]:

$$1/E_{hkl} = S_{11} - S_{44}(A-1)\Gamma_{hkl}. \quad (4.23)$$

The thus calculated variation of  $E_{hkl}$  in the  $(1\bar{1}0)$  and  $(010)$  planes is shown in polar diagrams for  $\gamma'$ -Fe<sub>4</sub>N and austenitic steel (Fe-Cr-Ni alloy [62]) in Figs. 4.6a and 4.6b. Austenitic steel exhibits a maximum of  $E_{hkl}$  in the  $\langle 111 \rangle$  directions ( $E_{\gamma,\max} = 303$  GPa) and a minimum in the  $\langle 100 \rangle$  directions ( $E_{\gamma,\min} = 100$  GPa). This contrasts with  $\gamma'$ -Fe<sub>4</sub>N that shows a completely reverse anisotropy of the elastic behaviour: The maximum of  $E_{hkl}$  occurs in the  $\langle 100 \rangle$  directions ( $E_{\gamma',\max} = 226$  GPa), and the minimum of  $E_{hkl}$  occurs in the  $\langle 111 \rangle$  directions ( $E_{\gamma',\min} = 128$  GPa). The Zener anisotropy ratio for austenitic steel is  $A = 3.48$ , whereas for  $\gamma'$ -Fe<sub>4</sub>N it is  $A = 0.53$ . Hence, the elastic constants of austenite (or austenitic steel) do not constitute reliable estimates for the elastic constants of  $\gamma'$ -Fe<sub>4</sub>N, as exhibited in particular by the nature of the anisotropy.

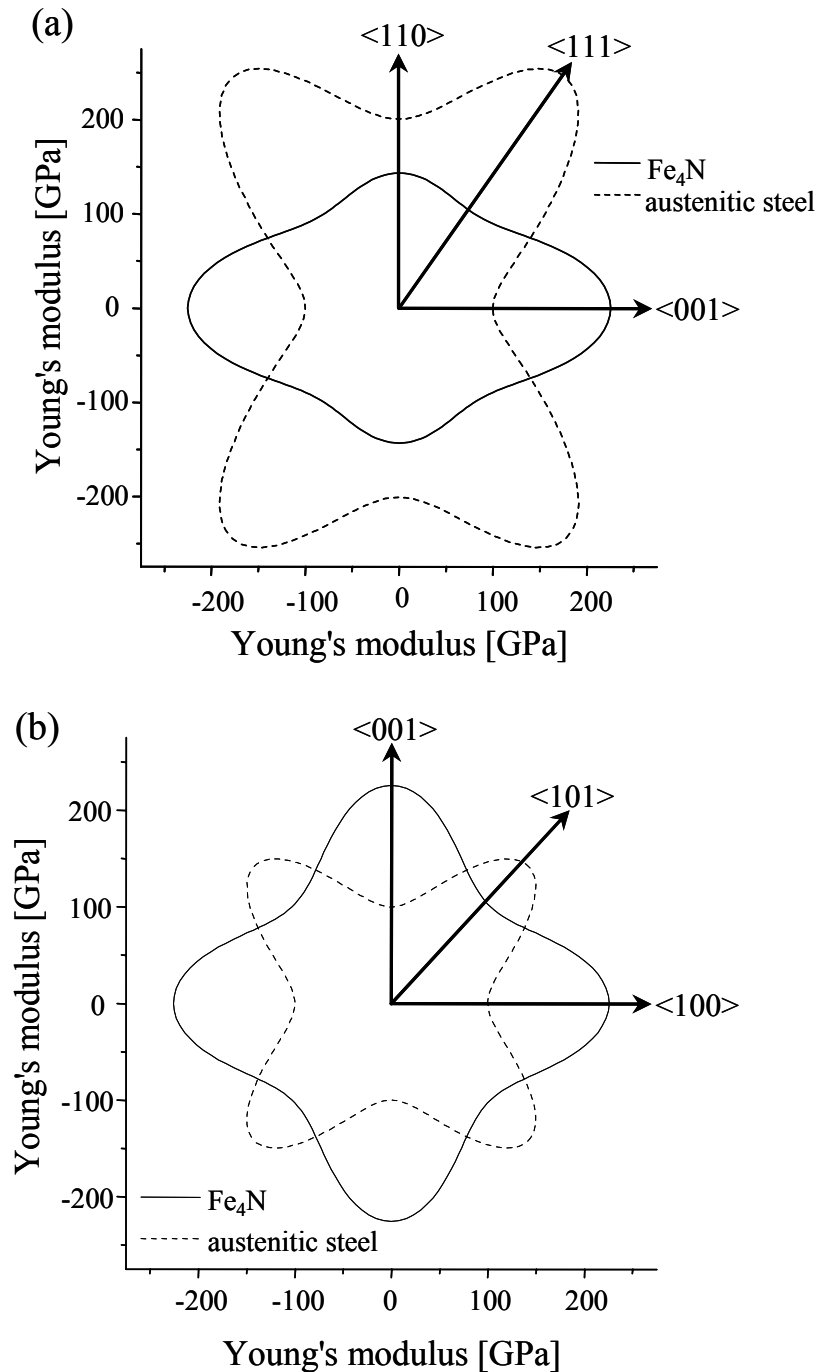


**Fig. 4.6:** Orientation dependence of the Young's modulus of  $\gamma'$ -Fe<sub>4</sub>N (solid line) and  $\gamma$ -Fe (dashed line) in polar coordinates as visualization of the single-crystal elastic anisotropy: cut (a) through the  $(1\bar{1}0)$  plane and (b) through the  $(010)$  plane.

The elastic anisotropy can often be related to the anisotropy of the chemical bonding in the crystal [63]. Then, one may try to understand the difference in the elastic properties of  $\gamma'$ -Fe<sub>4</sub>N and austenite on that basis. Recognizing that austenite shows the typical elastic anisotropy of *fcc*-type metals with  $A > 1$ , which can be

ascribed qualitatively as a direct consequence of the first nearest-neighbour interaction in  $\langle 110 \rangle$  directions<sup>4.4</sup>, the reverse elastic anisotropy of  $\gamma'$ -Fe<sub>4</sub>N ( $A < 1$ ) may then be considered as a consequence of the insertion of nitrogen atoms into the octahedral sites with fractional coordinates  $\frac{1}{2} \frac{1}{2} \frac{1}{2}$ , upon the (hypothetical) formation of  $\gamma'$  from  $\gamma$  (Fig. 4.2): the nitrogen atoms experience a relatively strong interaction with the Fe(II) atoms due to the short separation distance of  $a_\gamma/2$  in the  $\langle 100 \rangle$  directions<sup>4.5</sup>. Therefore, the occurrence of Fe(II)-N atomic chains in  $\langle 100 \rangle$  directions in  $\gamma'$ -Fe<sub>4</sub>N is responsible for a relatively high value of  $E_{hkl}$  in the  $\langle 100 \rangle$  directions. Indeed, B1 (NaCl) transition-metal ( $M$ ) carbides and nitrides in which all octahedral sites are occupied, and which consequently contain  $M$ -C/N chains, similar to the Fe(II)-N chains in  $\gamma'$ , also show very low Zener anisotropy ratios ( $A < 1$ ) [68]. Note that in  $\gamma'$ -Fe<sub>4</sub>N the low Zener anisotropy ratio is already achieved by occupancy of one fourth of the octahedral sites.

It must be remarked that for the calculation of the single-crystal elastic constants of  $\gamma'$ -Fe<sub>4</sub>N some approximations were used, which could lead to differences compared to real  $\gamma'$ -Fe<sub>4</sub>N<sub>1-y</sub>:

- (i) the approximate description of the exchange-correlation functional,
- (ii) ignorance of thermal (or entropy) effects (the calculations were performed for 0 K),
- (iii) the assumption that all octahedral sites  $\frac{1}{2} \frac{1}{2} \frac{1}{2}$  are occupied by nitrogen, whereas real  $\gamma'$ -Fe<sub>4</sub>N<sub>1-y</sub> in equilibrium with  $\alpha$ -Fe (at 823 K) contains only 19.58 at.% N, leading to 2.1 % unoccupied interstitial octahedral sites (in contact with  $\epsilon$ -Fe<sub>3</sub>N<sub>1+x</sub>: 19.94 at.% N in  $\gamma'$ ; 0.3 % unoccupied interstitial octahedral sites). Therefore, the Fe(II)-N chains are interrupted, which reduces the stiffness in  $\langle 100 \rangle$  directions.

---

<sup>4.4</sup> It was demonstrated for monoatomic *fcc* crystals (like  $\gamma$ -Fe), using a very simplified two-body central-force interatomic potential model considering only first nearest-neighbour interaction (along  $a/2\langle 110 \rangle$ ), that a Zener elastic anisotropy ratio of  $A = 2$  would be expected [64]. For austenitic steel this anisotropy ratio is reasonably well achieved ( $A_\gamma = 3.48$ ), and is also typical for other *fcc*-type metals, e.g.  $A_{Cu} = 3.20$ ,  $A_{Ni} = 2.57$  [65]. The deviation from  $A = 2$  is due to ignorance of second- and higher order neighbour interactions and due to interatomic interactions which cannot be described by simple pair wise central interatomic forces, which e.g. leads to breakdown of the Cauchy relationship for elastic constants, i.e. here  $C_{12} \neq C_{44}$ .

<sup>4.5</sup> Indeed, analysis of the present electronic structure calculations and those in [66, 67] indicated strong Fe(II)-N bonding.

#### 4.4.2 The effective, experimentally determined type of grain interaction

The results of the X-ray diffraction stress measurements on the  $\gamma'$ -Fe<sub>4</sub>N<sub>1-y</sub> layers (see section 4.3.3) confirm the type of intrinsic elastic anisotropy of  $\gamma'$ -Fe<sub>4</sub>N as predicted by the first-principles calculations:  $\varepsilon_{\psi}^{hkl}$  vs.  $\sin^2\psi$  plots show slopes pronouncedly less negative for the {200} reflections than for the {hhh} reflections (Fig. 4.4a). Indeed, according to Eqs. (4.14, 4.16, 4.18) for compressive stress ( $\sigma_{//} < 0$ ) the slope in  $\frac{1}{2}S_2^{hkl} \cdot \sigma_{//}$  vs.  $3\Gamma_{hkl}$  plots,  $\frac{d\frac{1}{2}S_2^{hkl}\sigma_{//}}{d3\Gamma_{hkl}}$ , should be negative for  $A < 1$  ( $A - 1 < 0$ ), irrespective of the type of grain interaction as given by the value of  $w$  (except for  $w = 1$ , i.e. Voigt-like grain interaction), whereas for  $A > 1$  the slope is always positive.

The values obtained for the weighting parameter  $w$  for the *effective* X-ray elastic constants, determined on the basis of the calculated single-crystal elastic constants using the  $f(\psi)$  method, indicate a distinct Voigt-like character of grain interaction for both samples ( $w = 0.85$  for sample A, Fig. 4.5a;  $w = 0.80$  for sample B, Fig. 4.5b, cf. Eq. (4.14)). These results for the type of grain interaction can be understood as follows: Both  $\gamma'$ -layers consist of laterally large  $\gamma'$  grains (grain size of the order of several micrometers; grain-size effects on the elastic properties can thus be neglected) on top of the  $\alpha$ -Fe substrate and are separated by grain boundaries oriented more or less perpendicularly to the specimen surface (confirmed in this work by additional electron back-scattering diffraction experiments (EBSD); not shown)<sup>4,6</sup>. In this case the thermal misfit arising from cooling from the nitriding temperature to ambient temperature (cf. section 4.3.3) is imposed at the base of the grains, i.e., the imposed misfit strain parallel to the interface is likely to be about the same for all grains (both the  $\gamma'$  layer and the  $\alpha$ -Fe substrate are cubic and hence exhibit isotropic thermal expansion). Opposite to what may be expected for thin films produced by physical vapour deposition (see, for example [69]), the grain boundaries oriented more or less perpendicularly to the specimen surface are not expected to be voided for the

<sup>4,6</sup> During nitriding N diffuses from the surface into the bulk and thus transforms  $\alpha$ -Fe to  $\gamma'$ -Fe<sub>4</sub>N<sub>1-y</sub> leading to a columnar grain structure. This grain morphology does not necessarily lead to a crystallographic texture, also because no strong epitaxy of  $\gamma'$ -Fe<sub>4</sub>N<sub>1-y</sub> on  $\alpha$ -Fe occurs. See also comment in section 4.3.2.2 about the absence of crystallographic texture.

$\gamma'$ -layer. Hence, a Reuss-like grain interaction is less likely and as a consequence the grain interaction becomes more Voigt-like (cf. discussion in [70, 71]).

Yet, it is worth noting that the values of the elastic constants, adopted for calculation of the XECs according to Eqs. (4.15-4.18) and as used in Eq. (4.14), strongly influence the value of  $w$  evaluated on the basis of the experimental data. If the calculated single-crystal elastic constants had led to another value of  $A$ , the fitted weighting parameter  $w$  would have been different: for example, if the true value of  $A$  of  $\gamma'$ -Fe<sub>4</sub>N<sub>1-y</sub> had been closer to 1, then the term  $(A-1)$  in Eqs. (4.17, 4.18) would have been less negative and a smaller weighting parameter  $w$  would have been obtained by fitting a straight line to the experimental data, implying a more Neerfeld-Hill-like, rather than a Voigt-like, type of grain interaction.

## 4.5 Conclusions

The single-crystal elastic constants  $C_{ij}$  of  $\gamma'$ -Fe<sub>4</sub>N (*fcc*-type iron substructure) at  $T = 0$  K calculated by first-principles methods are  $C_{11} = 307.2$  GPa,  $C_{12} = 134.1$  GPa, and  $C_{44} = 46.0$  GPa.  $\gamma'$ -Fe<sub>4</sub>N has a strikingly small Zener elastic anisotropy ratio of  $A = 0.53$  (i.e.  $A < 1$ ), involving  $\langle 111 \rangle$  as most compliant directions and  $\langle 100 \rangle$  as stiffest directions, whereas typical *fcc* metals such as austenite usually have an anisotropy ratio  $A > 1$ . This striking difference of  $\gamma'$ -Fe<sub>4</sub>N and austenite can be ascribed to the ordered presence of N atoms at  $\frac{1}{2} \frac{1}{2} \frac{1}{2}$  octahedral sites in  $\gamma'$ -Fe<sub>4</sub>N, leading to a strong interaction along the Fe(II)-N chains in  $\langle 100 \rangle$  directions.

The ‘abnormal’ elastic anisotropy of  $\gamma'$ -Fe<sub>4</sub>N was confirmed by X-ray diffraction stress analysis of  $\gamma'$ -Fe<sub>4</sub>N<sub>1-y</sub> layers grown on  $\alpha$ -Fe. The residual stresses in the  $\gamma'$ -layer are mainly thermally induced due to different coefficients of thermal expansion of  $\gamma'$ -Fe<sub>4</sub>N<sub>1-y</sub> and of  $\alpha$ -Fe. The elastic grain interaction in the  $\gamma'$ -layer was found to be close to Voigt-like.

## Acknowledgement

We are grateful to Dr. M. Knapp (Darmstadt University of Technology; present address: CELLS, Spain) for assistance with the synchrotron measurements performed at DESY Hasylab Beamline B2.

## References

- [1] Source book on nitriding: ASM, Metals Park, OH, 1977.
- [2] Knerr CH, Rose TC, Filkowski JH. In: ASM Handbook Heat Treating Vol 4, Eds.: Davis, JR, Davidson, GM, Lampman, SR, Zorc, TB, Daquila, JL, Ronke, AW, Henniger, KL, Uhl, RC, ASM International, 1991, p. 387.
- [3] Liedtke D, Baudis U, Boßlet J, Huchel U, Klümper-Westkamp H, Lerche W, Spies H-J. Wärmebehandlung von Eisenwerkstoffen. Renningen: Expert Verlag, 2006.
- [4] Bell T. Heat Treat Met 1975;2:39.
- [5] Dawes C, Tranter DF. Heat Treat Met 1985;3:70.
- [6] Jack KH. Proc R Soc London, A 1948;195:34.
- [7] Jacobs H, Rechenbach D, Zachwieja U. J Alloys Compd 1995;227:10.
- [8] Jack KH. Acta Crystallogr 1952;5:404.
- [9] Leineweber A, Jacobs H, Hüning F, Lueken H, Schilder H, Kockelmann W. J Alloys Compd 1999;288:79.
- [10] Leineweber A, Jacobs H, Hüning F, Lueken H, Kockelmann W. J Alloys Compd 2001;316:21.
- [11] Mittemeijer EJ, Somers MAJ. Surf Eng 1997;13:483.
- [12] Wriedt HA, Gokcen NA, Nafziger RH. Bull Alloy Phase Diagr 1987;8:355.
- [13] Somers MAJ, Mittemeijer EJ. Metall Mater Trans A 1995;26A:57.
- [14] Somers MAJ, Mittemeijer EJ. Härterei-Tech Mitt 1992;47:5.
- [15] Schwerdtfeger K, Grieveson, P., Turkdogan, E. T Metall Soc AIME 1969;245:2461.
- [16] Liapina T, Leineweber A, Mittemeijer EJ. Metall Mater Trans A 2006;37A:319.

- [17] Du H, Ågren J. *Z Metallkd* 1995;86:522.
- [18] Rozendaal HCF, Mittemeijer EJ, Colijn PF, van der Schaaf PJ. *Metall Mater Trans A* 1983;14A:395.
- [19] Somers MAJ, Mittemeijer EJ. *Metall Trans A* 1990;21A:189.
- [20] Rozendaal HCF, Colijn PF, Mittemeijer EJ. *Surf Eng* 1985;1:30.
- [21] Oettel H, Ehrentraut B. *Härterei-Tech Mitt* 1985;40:183.
- [22] Somers MAJ, Mittemeijer EJ. *J Mater Eng* 1990;12:111.
- [23] Welzel U, Ligot J, Lamparter P, Vermeulen AC, Mittemeijer EJ. *J Appl Crystallogr* 2005;38:1.
- [24] Hoffmann FT, Kreft U, Hirsch T, Mayr P. *Heat Treat Met* 1996;3:57.
- [25] Kreft U, Hoffmann F, Hirsch T, Mayr P. *Härterei-Tech Mitt* 1995;50:169.
- [26] Günther D, Hoffmann F, Hirsch T. *Härterei-Tech Mitt* 2004;59:18.
- [27] Quaeysaegens C, Knuyt G, Stals LM. *Vac Sci Technol A* 1996;14:2462.
- [28] Kamminga J-D, de Keijser TH, Mittemeijer EJ, Delhez R. *J Appl Crystallogr* 2000;33:1059.
- [29] Martin RM. *Electronic Structure: Basic Theory and Practical Methods*. Cambridge: Cambridge University Press, 2004.
- [30] Paufler P. *Physikalische Kristallographie*. Weinheim, Germany: VCH Verlagsgesellschaft, 1986.
- [31] Nye JF. *Physical properties of crystals*. New York: Oxford University Press, 2004.
- [32] Somers MAJ, van der Pers NM, Schalkoord D, Mittemeijer EJ. *Metall Trans A* 1989;20A:1533.
- [33] Teter DM, Gibbs GV, Boisen MB, Allan DC, Teter MP. *Phys Rev B* 1995;52:8064.
- [34] Shang S, Böttger A. *Acta Mater* 2005;53:255.
- [35] Kresse G, Furthmüller J. *Comp Mat Sci* 1996;6:15.
- [36] Kresse G, Furthmüller J. *Phys Rev B* 1996;54:11169.
- [37] Kresse G, Joubert D. *Phys Rev B* 1999;59:1758.
- [38] Perdew JP, Burke K, Ernzerhofer M. *Phys Rev Lett* 1996;77:3865.
- [39] Monkhorst HJ, Pack JD. *Phys Rev B* 1976;13:5188.

- [40] Blöchl PE, Jepsen O, Andersen OK. Phys Rev B 1994;49:16223.
- [41] Frazer BC. Phys Rev 1958;112:751.
- [42] Delhez R, de Keijser TH, Mittemeijer EJ. Surf Eng 1987;3:331.
- [43] Welzel U, Mittemeijer EJ. J Appl Phys 2003;93:9001.
- [44] Voigt W. Lehrbuch der Kristallphysik. Stuttgart: Teubner, 1966.
- [45] Bollenrath F, Hauk V, Müller EH. Z Metallkd 1967;58:76.
- [46] Wohlschlägel M, Baumann W, Welzel U, Mittemeijer EJ. Mater Sci Forum 2006;524-525:19.
- [47] Somers MAJ, Mittemeijer EJ. Härtereit-Tech Mitt 1992;47:175.
- [48] Kumar A, Welzel U, Mittemeijer EJ. J Appl Crystallogr 2006;39:633.
- [49] Chatterjee-Fischer R, Bodenhausen R, Eysell F-W, Hoffmann R, Liedke D, Mallener H, Rembges W, Schreiner A, Welker G. Wärmebehandlung von Eisen und Stahl - Nitrieren und Nitrocarburieren. Renningen-Malmsheim: Expert Verlag, 1995.
- [50] Colijn PF, Mittemeijer EJ, Rozendaal HCF. Z Metallkd 1983;74:620.
- [51] Wells A. J Mater Sci 1985;20:2439.
- [52] Somers MAJ, Mittemeijer EJ. Surf Eng 1987;3:123.
- [53] Gressmann T, Leineweber A, Mittemeijer EJ. in preparation.
- [54] Knapp M, Baetz C, Ehrenberg H, Fuess H. J Synchr Rad 2004;11:328.
- [55] TOPAS. General Profile and Structure Analysis Software for Powder Diffraction Data. Karlsruhe, Germany: Bruker AXS GmbH.
- [56] Warren BE. X-ray diffraction. New York: Dover Publications, 1990.
- [57] Stickforth J. Techn Mitt Krupp Forsch-Ber 1966;24:89.
- [58] Touloukian YS, Kirby RK, Taylor RE, Desai PD. Thermal Expansion: Metallic Elements and Alloys. New York: IFI/Plenum, 1977.
- [59] Somers MAJ, Mittemeijer EJ. Metall Trans A 1990;21A:901.
- [60] Yang CL, Abdelmeguid MM, Micklitz H, Michels G, Otto JW, Kong Y, Xue DS, Li FS. J Magn Magn Mater 1995;151:L19.
- [61] Adler JF, Williams Q. J Geophys Res 2005;110:Art. No. B01203.
- [62] Salmutter K, Stangler F. Z Metallkd 1960;51:544.



- [63] Schreuer J, Hausühl S. In: EMU Notes in Mineralogy, Vol 7, Ed.: Mitelich, R, 2005, p. 173.
- [64] Ledbetter HM, Moment RL. Acta Metall 1976;24:891.
- [65] Authier A. International Tables for Crystallography D: Physical Properties of Crystals. Dordrecht/Boston/London: Kluwer Academic Publishers, 2003.
- [66] Zhou W, Qu LJ, Zhang QM, Wang DS. Phys Rev B 1989;40:6393.
- [67] Sifkovits M, Smolinski H, Hellwig S, Weber W. J Magn Magn Mater 1999;204:191.
- [68] Chen X-J, Struzhkin VV, Z. W, Somayazulu M, Qian J, Kung S, Christensen AN, Zhao Y, Cohen RE, Mao H-K, Hemley RJ. Proc Natl Acad Sci USA 2005;102:3198.
- [69] Welzel U, Leoni M, Mittemeijer EJ. Philos Mag 2003;83:603.
- [70] Welzel U, Freour S, Mittemeijer EJ. Philos Mag 2005;85:2391.
- [71] Welzel U, Mittemeijer EJ. Z Kristallogr 2007;222:160.
- [72] Reuss A. Z. Angew Math Mech 1929;9:49.
- [73] Johnson RA. Phys Rev 1966;145:423.



## Zusammenfassung

### 5.1 Einleitung

Nitrieren und Nitrocarburieren sind wichtige oberflächenspezifische Wärmebehandlungsverfahren für Werkstücke aus Eisen, Eisenbasislegierungen oder Stahl. Bei diesen thermochemischen Verfahren bildet sich an der Oberfläche eine Eisen-(carbo-)nitridverbindungsschicht (Abb. 5.1), welche die Verschleißfestigkeit als wichtige tribologische Eigenschaft, sowie die Korrosionsbeständigkeit der Werkstücke erhöht. Die unter der Verbindungsschicht liegende Diffusionszone, in welcher der ferritische Grundwerkstoff mit eindiffundiertem Stickstoff angereichert ist, verbessert überdies die Ermüdungsfestigkeit [1, 2]

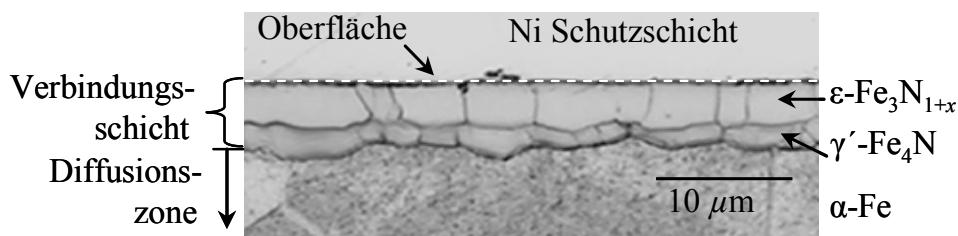


**Abb. 5.1:** Typische Mikrostruktur einer gasnitrierten Eisenprobe, mit einer Verbindungsschicht aus  $\epsilon$ - und  $\gamma'$ -Eisennitrid an der Oberfläche und einer darunterliegenden Diffusionszone.

Beim Gasnitrieren, einem der wichtigsten technischen Nitrierverfahren, ist es möglich, über die Zusammensetzung der aus  $\text{NH}_3$  und  $\text{H}_2$  bestehenden Gasatmosphäre, das chemische Potential von Stickstoff an der Werkstückoberfläche zu regeln. Hierbei wird Gleichgewicht zwischen dem chemischen Potential von Stickstoff in der Gasatmosphäre und an der Werkstückoberfläche angenommen. Typische Behandlungstemperaturen liegen zwischen  $450\text{ }^\circ\text{C}$  und  $590\text{ }^\circ\text{C}$ . Während des

Nitrierens wird zuerst Stickstoff im  $\alpha$ -Eisen gelöst. Anschließend bildet sich eine Verbindungsschicht an der Oberfläche aus, die, abhängig vom chemischen Potential von Stickstoff in der Gasphase und der Behandlungstemperatur, aus verschiedenen Eisennitridphasen besteht.

Wegen der Eindiffusion von Stickstoff in das Werkstück kann nur an der Oberfläche Gleichgewicht mit der Gasphase hergestellt werden. Mit zunehmendem Abstand von der Oberfläche nimmt das chemische Potential von Stickstoff ab [3]. Dies geht mit einer Abnahme des Stickstoffgehalts sowohl in den Eisennitriden der Verbindungsschicht als auch im  $\alpha$ -Eisen einher, d. h. ein eindiffusionskontrolliertes Stickstoffkonzentrationstiefenprofil bildet sich aus (Abb. 5.2a). Durch Abschrecken kann der Eindiffusionsprozess gestoppt werden und das Stickstoffkonzentrationstiefenprofil kann bei Raumtemperatur erhalten bleiben.

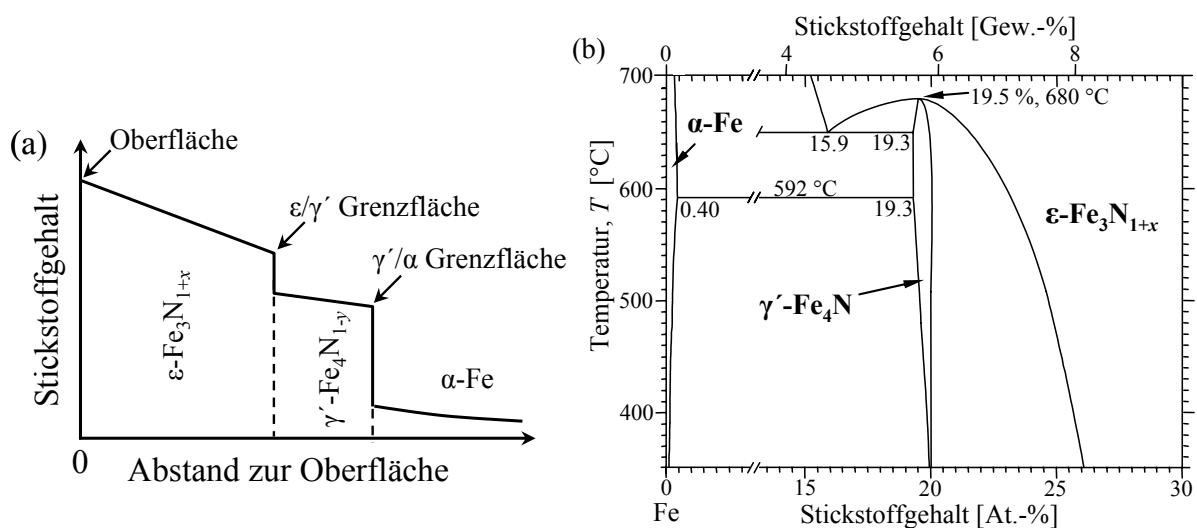


**Abb. 5.2:** (a) Typisches Stickstofftiefenprofil einer durch Nitrieren hergestellten Verbindungsschicht. Lokales Gleichgewicht gemäß dem Fe-N Phasendiagramm ((b), [4]) wird hierbei an den Phasengrenzen (durch Pfeile in (a) gekennzeichnet) angenommen.

Beim Gasnitrocarburieren wird zusätzlich Kohlenstoff über die Gasphase bereitgestellt. Üblicherweise erfolgt der Kohlenstoffübertrag von der Gasphase in das Werkstück über die heterogene Dissoziation von CO.

Die wichtigsten Phasen in Verbindungsschichten sind  $\gamma'$ -Fe<sub>4</sub>N<sub>1-y</sub>,  $\epsilon$ -Fe<sub>3</sub>N<sub>1+x</sub> (siehe Abb. 5.2b) und Zementit, Fe<sub>3</sub>C. Die ersten beiden Phasen,  $\gamma'$  und  $\epsilon$ , sind typische interstitielle Verbindungen, in denen die Eisenatome kubisch dichtest ( $\gamma'$ ) bzw. hexagonal dichtest ( $\epsilon$ ) gepackt sind und Stickstoffatome partiell, unter

Ausbildung einer Fernordnung, Oktaederlücken besetzen [5-11]. Zementit ist orthorhombisch mit zwölf Eisenatomen und vier Kohlenstoffatomen pro Elementarzelle, wobei jedes Kohlenstoffatom in relativ unregelmäßiger Art von acht Eisenatomen umgeben ist [12]. Während sowohl  $\gamma'$  als auch Zementit einen sehr schmalen Homogenitätsbereich aufweisen, ist der Homogenitätsbereich der  $\epsilon$ -Phase groß und stark temperaturabhängig (Abb. 5.2b) [4], was zu erheblichen Änderungen der Gitterparameter über den Zusammensetzungsbereich führt [13, 14]. Überdies kann in der  $\epsilon$ -Phase Kohlenstoff teilweise Stickstoff substituieren [15]. Während des Verbindungsschichtwachstums und beim anschließenden Abschrecken auf Raumtemperatur kommt es in den Verbindungsschichten zum Aufbau von Makrospannungen, die zu signifikanten Gitterdehnungen führen [16-18].

In dieser Arbeit wird zum einen (i) die Bildung von massiven Zementitschichten und die damit verbundene Wachstumskinetik untersucht und zum anderen (ii) werden die Mikrostrukturen von Eisennitridverbindungsschichten mit Hilfe von Röntgenbeugungsmessungen und mittels Berechnungen nach der *First-Principles* Methode analysiert. Abschnitt (ii) ist in die Analyse von  $\epsilon$ -Fe<sub>3</sub>N<sub>1+x</sub>-Schichten und in die Untersuchung der elastischen Eigenschaften von  $\gamma'$ -Schichten unterteilt.

## 5.2 Experimentelles

Rechteckige Eisenplättchen (ca. 1 mm dick) wurden durch Kaltwalzen von gegossenen Reineisenstäben hergestellt und anschließend für 2 Stunden bei 700 °C unter Wasserstoffatmosphäre rekristallisiert. Die thermochemischen Wärmebehandlungen der Eisenplättchen wurden in einem vertikal angeordneten Mehrzonenofen bei 550 °C durchgeführt. Zum Nitrieren wurden NH<sub>3</sub>/H<sub>2</sub>- und zum Nitrocarburieren wurden NH<sub>3</sub>/H<sub>2</sub>/CO/N<sub>2</sub>-Gasgemische verwendet. Die Gasströme der einzelnen Gase wurden separat über Massedurchflussregler gesteuert. Beendet wurden die Wärmebehandlungen durch Abschrecken der Proben in mit Stickstoff gespültem Wasser.

Die Charakterisierung der behandelten Proben erfolgte mittels Lichtmikroskopie an polierten und geätzten Querschliffen, sowie mittels Röntgenpulverdiffraktometrie. Letztere wurde zur Phasenanalyse mittels  $\text{CoK}\alpha$ -Strahlung in Bragg-Brentano-Geometrie eingesetzt. Zur röntgenographischen Spannungsmessung wurde sowohl  $\text{CoK}\alpha$ -Strahlung als auch Synchrotronstrahlung ( $\lambda = 0.8 \text{ \AA}$ ) verwendet. Die entsprechenden Diffraktometer waren mit einer Eulerwiege ausgestattet und arbeiteten in Parallelstrahlgeometrie.

## 5.3 Ergebnisse und Diskussion

### 5.3.1 Bildung und Wachstumskinetik von massiven Zementitschichten

Die Behandlung von Eisen in stark aufkohlenden Gasatmosphären bei Temperaturen von unter  $600 \text{ }^\circ\text{C}$  führt üblicherweise zur Abscheidung von Graphit auf der Probenoberfläche. Zusätzlich kann sich in Probe an der Oberfläche Zementit bilden. Dieser ist jedoch im Vergleich zu Graphit thermodynamisch metastabil und zersetzt sich daher in Graphit und Eisenstaub. Dieser Prozess, der die Probe zerstört, wird als „Metal Dusting“ bezeichnet [19].

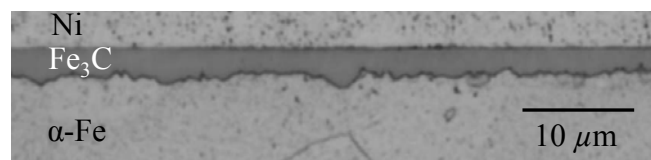


**Abb. 5.3:** Lichtmikroskopische Aufnahme eines Querschliffes einer auf  $\alpha$ -Fe durch Nitrocarburieren bei  $550^\circ\text{C}$  hergestellten Zementitschicht. Die verwendete Gasatmosphäre bestand aus 20.0 Vol.-%  $\text{CO}$ , 58.0 Vol.-%  $\text{H}_2$ , 13.2 Vol.-%  $\text{NH}_3$  und 8.8 Vol.-%  $\text{N}_2$ .

In dieser Arbeit konnte erstmalig gezeigt werden, dass die gezielte Zugabe von  $\text{NH}_3$  zu stark aufkohlenden  $\text{CO}/\text{H}_2/\text{N}_2$ -Gasmischen „Metal Dusting“ verhindern kann und somit massive Zementitschichten auf  $\alpha$ -Fe gebildet werden können (Abb. 5.3). Der Prozessparameterraum, in dem dies gelingt, ist jedoch relativ schmal (Abb. 5.3a): ein zu hoher  $\text{NH}_3$ -Gehalt führt durch die zusätzliche Bildung von Eisen(carbo)nitriden in der Verbindungsschicht zu komplexen Mikrostrukturen, während ein zu geringer  $\text{NH}_3$ -Gehalt in der Gasmischung die Graphitabscheidung und

das „Metal Dusting“ nicht vollständig unterdrücken kann. Tendenziell wurde festgestellt, dass eine Erhöhung des  $\text{NH}_3$ -Gehaltes – in oben genannten Grenzen – zu einer schnelleren Wachstumsgeschwindigkeit der Zementitschichten führt.

Bei konstanten Prozessparametern (13.2 %  $\text{NH}_3$ , 58 %  $\text{H}_2$ , 20 %  $\text{CO}$ , 8.8 %  $\text{N}_2$ ,  $T = 550^\circ\text{C}$ ) wurde die Zeitabhängigkeit des Wachstums von Zementitschichten untersucht (Abb. 5.4b). Die Zementitschichtdicke  $S$  kann als Funktion der Behandlungszeit mit einem modifizierten parabolischen Wachstumsgesetz beschrieben werden:

$$S^2 = kt + S_0^2, \quad (5.1)$$

wobei  $k$  die parabolische Wachstumskonstante und  $S_0$  eine hypothetische anfängliche Schichtdicke sind.

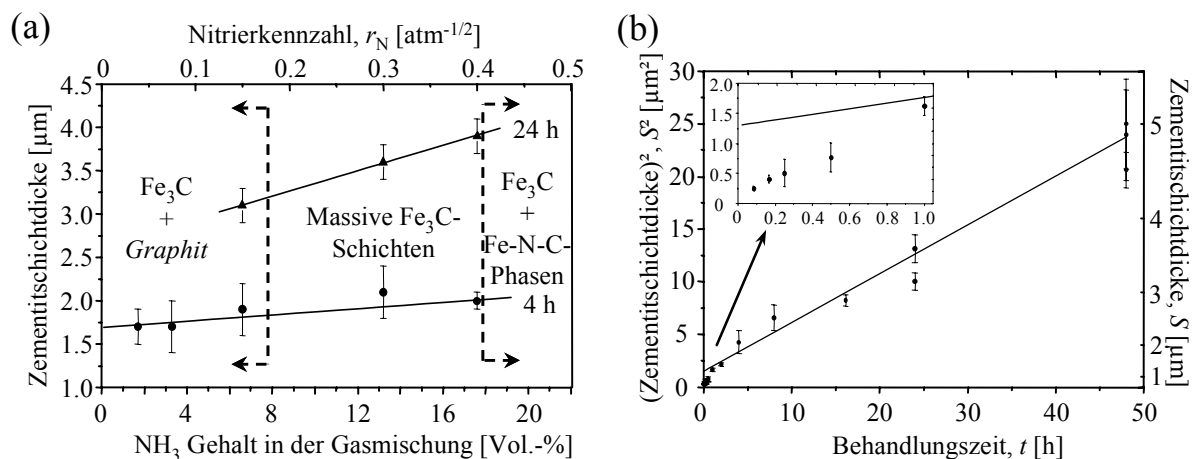


**Abb. 5.4:** (a) Entwicklung der Zementitschichtdicke bei  $550^\circ\text{C}$  nach einer Behandlungsdauer von 4 h und 24 h in Abhängigkeit des  $\text{NH}_3$  Gehalts in einer Atmosphäre der Zusammensetzung 20.0 Vol.-%  $\text{CO}$ , 58.0 Vol.-%  $\text{H}_2$ , 22.0 –  $n$  Vol.-%  $\text{NH}_3$  und  $n$  Vol.-%  $\text{N}_2$ . (b) Zeitliche Entwicklung der quadratischen Zementitschichtdicke bei konstanten Nitrocarburierbedingungen:  $550^\circ\text{C}$ , 20.0 Vol.-%  $\text{CO}$ , 58.0 Vol.-%  $\text{H}_2$ , 13.2 Vol.-%  $\text{NH}_3$ , 8.8 Vol.-%  $\text{N}_2$ . Die durchgezogene Linie stellt eine angepasste Gerade (für  $t > 1$  h) nach einem modifizierten parabolischen Wachstumsgesetz (Gleichung 5.1) dar.

$S_0$  beschreibt einen Versatz in den Schichtdickendaten, der durch Abweichungen von einem rein parabolischen Wachstumsgesetz,  $S^2 = kt$ , aufgrund eines anfänglich schnelleren Schichtwachstums ( $S^2 = 0$  bei  $t < 0$ ) verursacht ist. Begründet werden kann dies durch einen zweistufigen Wachstumsmechanismus: im Anfangsstadium ist die Zementitschicht noch nicht geschlossen und Kohlenstoff kann

hauptsächlich durch Ferrit diffundieren. Zusätzlich ist der Zementit anfänglich defektreich (z. B. enthält viele Korngrenzen), was zu einem erhöhten Diffusionskoeffizienten von Kohlenstoff im Zementit führt. Nach Ausbildung einer geschlossenen Zementitschicht und Ausheilung von Defekten ist die Diffusion von Kohlenstoff durch die Zementitschicht der geschwindigkeitsbestimmende Schritt und ein parabolisches Wachstum kann zugrunde gelegt werden.

### 5.3.2 Röntgenbeugungsanalyse von $\epsilon$ - $\text{Fe}_3\text{N}_{1+x}$ Schichten: Linienprofilanalyse

Beim Nitrieren bildet sich während der Eindiffusion von Stickstoff innerhalb von  $\epsilon$ -Eisennitridschichten ein Stickstoffkonzentrationstiefenprofil aus (Abb. 5.2a). In der Literatur wird für das Stickstofftiefenprofil häufig ein linearer Verlauf angenommen [3]. Die Zusammensetzungsänderungen innerhalb von  $\epsilon$ -Schichten sollten zu starken Variationen der hexagonalen Gitterparameter führen, wobei angenommen wird, dass ein direkter Zusammenhang zwischen Stickstoffgehalt und der Größe der Gitterparameter besteht [13, 14]<sup>5.1</sup>. Sowohl über das tatsächliche Tiefenprofil der Gitterparameter, als auch über die auftretenden Makrospannungen innerhalb von  $\epsilon$ -Schichten war bisher wenig bekannt.

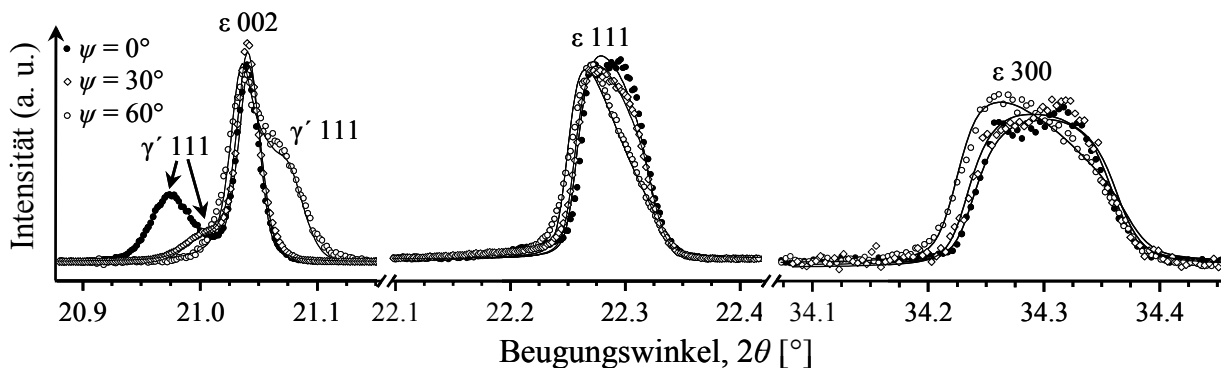


**Abb. 5.5:** Ausschnitt aus den an einer  $\epsilon$ - $\text{Fe}_3\text{N}_{1+x}$  Schicht gemessenen Röntgenbeugungsprofilen. Die gemessenen Daten weisen eine ausgeprägte anisotrope ( $hkl$ -abhängige) Reflexverbreiterung, sowie eine vom Kippwinkel  $\psi$  abhängige Reflexverschiebung auf. Die durchgezogenen Linien durch die Messpunkte wurden durch Fitten mit einem Modell für die Mikrostruktur (zu Details siehe Kapitel 3) erhalten. Der  $\gamma'$ -111 Reflex, der an stark  $\psi$ -abhängigen Positionen auftritt, wurde separat mit pseudo-Voigt-Funktionen angepasst.

<sup>5.1</sup> Die Gitterparameter können für eine gegebene Zusammensetzung jedoch je nach Ordnungsgrad in der Stickstoffüberstruktur beeinflusst sein, z. B. verursacht durch die vorangegangene Abkühlprozedur (langames Abkühlen oder schnelles Abschrecken) nach der Herstellung [14].



Mit unterschiedlichen Nitrierparametern hergestellte  $\varepsilon$ -Schichten wurden mittels hochauflösenden Röntgenbeugungsmessungen (mit Synchrotronstrahlung) unter Variation der Probenverkipfung relativ zum Beugungsvektor untersucht. Die erhaltenen, kompliziert geformten Beugungsprofile (Abb. 5.5; exemplarisch für eine Probe) zeigten zum einen ausgeprägte, anisotrope ( $hkl$ -abhängige) Reflexverbreiterung und zum anderen kippwinkelabhängige ( $\psi$ ) Verschiebung der Bragg-Reflexe. Ein Modell für die Mikrostruktur von  $\varepsilon$ -Schichten zur gleichzeitigen Beschreibung aller aufgenommenen Reflexe wurde entwickelt: sowohl die anisotrope Reflexverbreiterung, als auch die Reflexgestalt und -verschiebung der gemessenen Beugungsprofile können mit dem Modell gut beschrieben werden (Abb. 5.5).

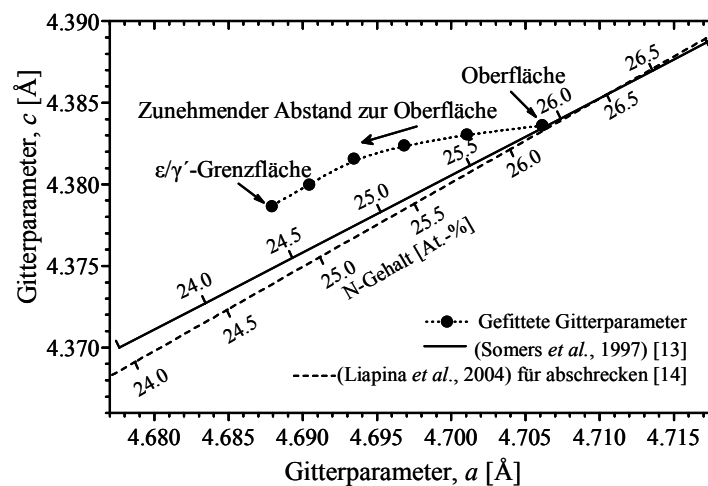


**Abb. 5.6:** Aus dem Fitprozess (für Details siehe Kapitel 3) erhaltene tiefenabhängige Gitterparameter einer  $\varepsilon$ -Verbindungsschicht. Mit zunehmendem Abstand zur Oberfläche verringern sich die Werte der Gitterparameter. Eine deutliche Abweichung von den in der Literatur vorgeschlagenen Stickstoffkonzentrationsabhängigkeiten der Gitterparameter kann in der Tiefe der Schicht beobachtet werden.

Die beobachtete Reflexverbreiterung konnte hauptsächlich auf das Stickstoff-Tiefenprofil in den  $\varepsilon$ -Schichten zurückgeführt werden. Die für verschiedene  $\varepsilon$ -Schichten unterschiedlich ausgeprägte Reflexverbreiterung konnte mit den unterschiedlichen Nitrierbedingungen begründet werden. Die erhaltenen Werte für die spannungsfreien Gitterparameter  $a$  und  $c$  nehmen mit zunehmendem Abstand zur Oberfläche ab, wobei kein linearer Zusammenhang zwischen den Gitterparametern und dem Oberflächenabstand beobachtet wurde. Die Gitterparameter nahe der  $\varepsilon/\gamma'$  Grenzfläche sind durch Kornwechselwirkung beeinflusst, die der anisotropen

thermischen Ausdehnung der  $\varepsilon$ -Phase entgegenwirken. Das führt dazu, dass die bei Raumtemperatur gemessenen  $c/a$ -Verhältnisse (nahe der  $\varepsilon/\gamma'$ -Grenzfläche) von polykristallinen  $\varepsilon$ -Schichten im Vergleich zu homogen, spannungsfreien  $\varepsilon$ -Pulvern zu groß sind (Abb. 5.6).

Die Reflexverschiebungen wurden auf ein Spannungstiefenprofil zurückgeführt, welches sich während des Abschreckens der Proben nach dem Nitrieren ausbildet. Die Stickstoffkonzentrationsabhängigkeit des isotrop-gemittelten Ausdehnungskoeffizienten der  $\varepsilon$ -Phase,  $\alpha_{\varepsilon, \text{isotrop}}$ , führt zu Zugspannungen an der Oberfläche und zu Druckspannungen an der  $\varepsilon/\gamma'$ -Grenzfläche. Für hohe Stickstoffgehalte (z. B. an der Oberfläche) ist  $\alpha_{\varepsilon, \text{isotrop}}$  größer als der Ausdehnungskoeffizient des als starr angenommenen  $\alpha$ -Fe-Substrates,  $\alpha_{\alpha\text{-Fe}}$ , während für niedrige Stickstoffgehalte, z. B. nahe der  $\varepsilon/\gamma'$ -Grenzfläche,  $\alpha_{\varepsilon, \text{isotrop}}$  kleiner als  $\alpha_{\alpha\text{-Fe}}$  ist.

### 5.3.3 Elastische Anisotropie von $\gamma'$ -Eisennitrid

Zur quantitativen Auswertung von röntgenographischen Eigenspannungsmessungen ist das Wissen um die einkristall-elastischen Eigenschaften des untersuchten Materials von elementarer Wichtigkeit [20]. Für viele Materialien sind die einkristall-elastischen Konstanten nicht bekannt und können experimentell nicht bestimmt werden, da z. B. keine ausreichend großen Einkristalle hergestellt werden können.

Im Rahmen dieser Arbeit wurden zum ersten Mal die einkristall-elastischen Konstanten  $C_{ij}$  von kubischem  $\gamma'$ -Fe<sub>4</sub>N mittels *First-Principles* Berechnungen (für 0 K) bestimmt:  $C_{11} = 307.2$  GPa,  $C_{12} = 134.1$  GPa,  $C_{44} = 46.0$  GPa. Die daraus resultierende, für *fcc*-artige Metalle ungewöhnliche elastische Anisotropie  $A = 2C_{44}/(C_{11}-C_{12}) = 0.53$  ist deutlich kleiner als 1. Damit sind die  $\langle 100 \rangle$ -Richtungen die steifsten Richtungen, während üblicherweise bei *fcc* Metallen ( $A > 1$ ) die  $\langle 111 \rangle$ -Richtungen am steifsten sind (Abb. 5.7). Diese außergewöhnliche elastische Anisotropie wurde durch röntgenographische Eigenspannungsmessungen an  $\gamma'$ -Schichten, bei denen jeweils mehrere Reflexe  $hkl$  analysiert wurden, bestätigt (Abb. 5.8). Die mittels der sogenannten  $f(\psi)$ -Methode bestimmten Druckspannungen in den  $\gamma'$ -Schichten von ca. – 670 MPa sind überwiegend thermisch induziert.

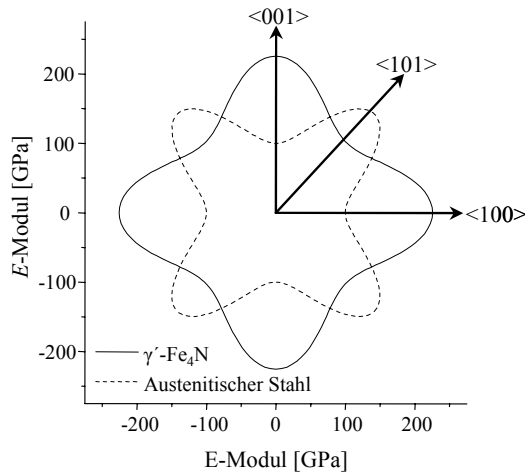


**Abb. 5.7:** Orientierungsabhängigkeit des  $E$ -Moduls (Schnitt durch die (010) Ebene) von  $\gamma'$ -Fe<sub>4</sub>N und von austenitischem Stahl [21] zur Visualisierung der elastischen Anisotropie.

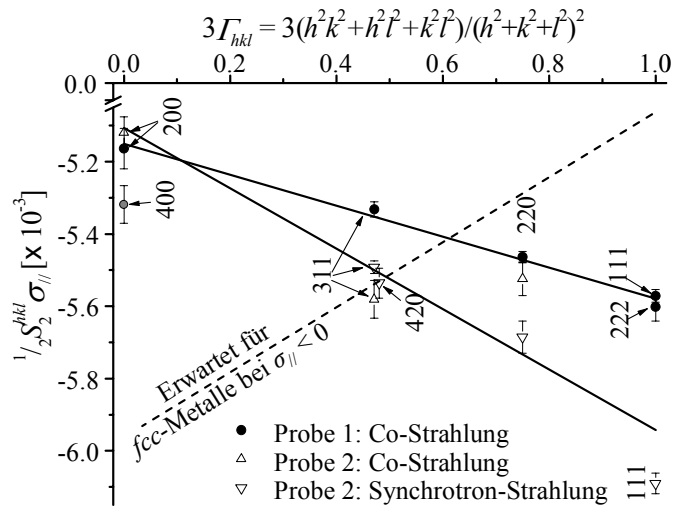


**Abb. 5.8:** Orientierungsabhängigkeit der Steigung  $\frac{1}{2}S_2^{hkl} \cdot \sigma_{||}$ . Die Werte für  $\frac{1}{2}S_2^{hkl} \cdot \sigma_{||}$  wurden aus Auftragungen von  $\epsilon^{hkl}$  gegen  $\sin^2\psi$ , die an zwei verschiedenen  $\gamma'$ -Schichten gemessen wurden, bestimmt. Die Steigung der gefitteten Geraden (durchgezogene Linien) sind negativ (bei  $\sigma_{||} < 0$ ), während für typische  $fcc$ -Metalle eine positive Steigung erwartet wird (gestrichelte Linie).

Begründet werden kann die elastische Anisotropie von  $\gamma'$ -Fe<sub>4</sub>N mit seiner Kristallstruktur. In  $\gamma'$ -Fe<sub>4</sub>N sind die Oktaederlücken (an der Position  $\frac{1}{2} \frac{1}{2} \frac{1}{2}$ ) des  $fcc$ -artigen Eisengitters geordnet mit Stickstoff besetzt (Abb. 5.9). Dies führt zu den kürzesten interatomaren Abständen in  $\gamma'$  zwischen den „flächenzentrierten“ Eisenatomen (an den Positionen  $\frac{1}{2} \frac{1}{2} 0$ ,  $\frac{1}{2} 0 \frac{1}{2}$  und  $0 \frac{1}{2} \frac{1}{2}$ ) und Stickstoff und damit zu starken Wechselwirkungen in  $\langle 100 \rangle$ -Richtung. In reinen  $fcc$ -Metallen sind die kürzesten interatomaren Abstände hingegen in  $\langle 110 \rangle$ -Richtung zu finden, was zu einer elastischen Anisotropie von  $A > 1$  führt.

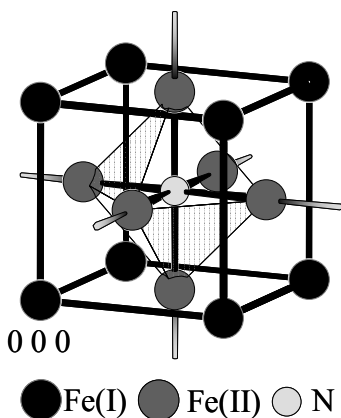


**Abb. 5.9:** Elementarzelle von kubischem  $\gamma'$ -Fe<sub>4</sub>N. Stickstoff besetzt  $\frac{1}{4}$  der Oktaederlücken des  $fcc$ -artigen Eisengitters. Die kürzesten interatomaren Abstände zwischen Fe(II) und N verlaufen in  $\langle 100 \rangle$ -Richtung.

## Literatur

- [1] Knerr CH, Rose TC, Filkowski JH. In: ASM Handbook Heat Treating Vol 4, Eds.: Davis, JR, Davidson, GM, Lampman, SR, Zorc, TB, Daquila, JL, Ronke, AW, Henniger, KL, Uhl, RC, ASM International, 1991, p. 387.
- [2] Liedtke D, Baudis U, Boßlet J, Huchel U, Klümper-Westkamp H, Lerche W, Spies H-J. Wärmebehandlung von Eisenwerkstoffen. Renningen: Expert Verlag, 2006.
- [3] Mittemeijer EJ, Somers MAJ. Surf Eng 1997;13:483.
- [4] Wriedt HA, Gokcen NA, Nafziger RH. Bull Alloy Phase Diagr 1987;8:355.
- [5] Hägg G. Nature 1928;121:826.
- [6] Jack KH. Proc R Soc London, A 1948;195:34.
- [7] Jack KH. Proc R Soc London, A 1948;195:56.
- [8] Jack KH. Acta Crystallogr 1952;5:404.
- [9] Jacobs H, Rechenbach D, Zachwieja U. J Alloys Compd 1995;227:10.
- [10] Leineweber A, Jacobs H. J Alloys Compd 2000;308:178.
- [11] Leineweber A, Jacobs H, Hüning F, Lueken H, Kockelmann W. J Alloys Compd 2001;316:21.
- [12] Wood IG, Vocadlo L, Knight KS, Dobson DP, Marshall WG, Price GD, Brodholt J. J Appl Crystallogr 2004;37:82.
- [13] Somers MAJ, Kooi BJ, Maldzinski L, Mittemeijer EJ, van der Horst AA, van der Kraan AM, van der Pers NM. Acta Mater 1997;45:2013.
- [14] Liapina T, Leineweber A, Mittemeijer EJ, Kockelmann W. Acta Mater 2004;52:173.
- [15] Naumann FK, Langenscheid, G. Arch Eisenhüttenw 1965;36:677.
- [16] Rozendaal HCF, Colijn PF, Mittemeijer EJ. Surf Eng 1985;1:30.
- [17] Oettel H, Ehrentraut B. Härterei-Tech Mitt 1985;40:183.
- [18] Somers MAJ, Mittemeijer EJ. J Mater Eng 1990;12:111.
- [19] Grabke HJ. Mater Corr 2003;54:736.
- [20] Welzel U, Ligot J, Lamparter P, Vermeulen AC, Mittemeijer EJ. J Appl Crystallogr 2005;38:1.
- [21] Salmutter K, Stangler F. Z Metallkd 1960;51:544.

---

## *List of publications*

- T. Gressmann, M. Nikolussi, A. Leineweber, and E.J. Mittemeijer. *Formation of massive cementite layers on iron by ferritic carburising in the additional presence of ammonia*. Scripta Mater, 55 (2006) 723.
- A. Leineweber, T. Liapina, T. Gressmann, M. Nikolussi, and E.J. Mittemeijer. *Phase transformations and interstitial atom diffusion in iron-nitride, iron-carbonitride and iron-carbide layers*. Advances in Science and Technology, 46 (2006) 32.
- T. Gressmann, A. Leineweber, E.J. Mittemeijer, and M. Knapp. *X-ray diffraction analysis of an  $\epsilon/\gamma'$  iron-nitride compound double layer*. Z Kristallogr Suppl (accepted).
- T. Gressmann, M. Wohlschlögel, S. Shang, U. Welzel, A. Leineweber, E. J. Mittemeijer, and Z.-K. Liu. *Elastic anisotropy of  $\gamma'$ -Fe<sub>4</sub>N and elastic grain interaction in  $\gamma'$ -Fe<sub>4</sub>N<sub>1-y</sub> layers on  $\alpha$ -Fe: first-principles calculations and diffraction stress measurements*. Acta Mater 55 (2007) 5833.
- T. Gressmann, A. Leineweber, and E.J. Mittemeijer. *Simultaneous determination of concentration- and stress-depth profiles in hexagonal  $\epsilon$ -iron-nitride compound layers by means of X-ray diffraction line profile analysis*. Submitted to Phil Mag.



## *Danksagung*

Die vorliegende Arbeit wurde am Institut für Metallkunde der Universität Stuttgart und am Max-Planck-Institut für Metallforschung angefertigt. An dieser Stelle möchte ich all denen danken, die zum Gelingen dieser Arbeit beigetragen haben.

An erster Stelle möchte ich mich bei Herrn Prof. Dr. Ir. E.J. Mittemeijer für die Aufnahme in seine Abteilung, die Überlassung des interessanten Themas und somit für das in mich gesetzte Vertrauen besonders bedanken. Seine Betreuung durch die zahlreichen und regelmäßigen wissenschaftlichen Diskussionen hatte großen Einfluss auf die Entstehung der Arbeit, ließen aber dennoch viel Spielraum für die eigenen Entfaltungsmöglichkeiten.

Herrn Prof. Dr. F. Aldinger danke ich für die freundliche Übernahme des Mitberichts, sowie Herrn Prof. Dr. H. Bertagnolli für die Zusage den Prüfungsvorsitz zu übernehmen.

Herrn Dr. A. Leineweber, meinem täglichen Betreuer, danke ich für die stete Diskussionsbereitschaft und seine wertvollen Ratschläge. Zum erfolgreichen Durchführen und Abschließen der Arbeit hat er in großem Maße beigetragen.

Allen Mitarbeitern des Max-Planck-Instituts für Metallforschung, insbesondere den Kollegen der Abteilung Mittemeijer, sei für die gute Zusammenarbeit bei den kleinen und großen Problemen des Forschungsalltages und für die angenehme Arbeitsatmosphäre gedankt. Namentlich möchte ich hier Marc Nikolussi hervorheben, mit dem ich eine intensive Zusammenarbeit hatte, sowie Jürgen Köhler, der für alle technischen Probleme eine Lösung parat hatte.

Ermöglicht wurde diese Arbeit durch die finanzielle Unterstützung der „International Max Planck Research School for Advanced Materials (IMPRS-AM)“.

Für die persönliche Unterstützung danke ich meinen Eltern, meiner Freundin Andrea sowie meinen Freunden und Bekannten, die mir in dieser Zeit viel Verständnis entgegengebracht haben.





## *Curriculum Vitae*

### **Thomas Greßmann**

born on January 10<sup>th</sup> 1979 in Bayreuth (Germany)

#### **School**

1985-1989            Primary school: Grundschule Eckersdorf  
1989-1998            High school: Wirtschaftswissenschaftliches und mathematisch-naturwissenschaftliches Gymnasium Bayreuth

#### **Academic studies**

1998-2003            University of Bayreuth  
                          Faculty of Applied Science  
                          Study of Materials Science  
  
2003                    University of Bayreuth  
                          Diploma thesis at the department of Metals and Alloys:  
                          *Characterisation of Lead-Free Solder Alloys*

#### **Dissertation**

2004-2007            PhD student at the Max Planck Institute for Metals Research,  
                          Institute for Materials Science, University of Stuttgart  
                          Promoter: Prof. Dr. Ir. Eric J. Mittemeijer  
                          Research Theme: *Fe-C and Fe-N compound layers: growth kinetics and microstructure*